Identifying and harnessing mechanisms that are more strongly required for cancer cell division

Kevin Larocque

A

Thesis

in the Department

of

Biology

Presented in Partial Fulfillment of the Requirements

For the Degree of

Doctor of Philosophy in Biology at

Concordia University

Montreal, Quebec, Canada

January 2023

CONCORDIA UNIVERSITY
School of Graduate Studies

This is to certify that the thesis prepared

By: Kevin Larocque

Entitled: Identifying and harnessing mechanisms that are more strongly required

for cancer cell division

and submitted in partial fulfillment of the requirements for the degree of

Doctor Of Philosophy (Biology)

complies with the regulations of the University and meets the accepted standards with respect to originality and quality.

Signed by the final Examining Committee:

_____ Chair
Dr. Peter Darlington

_____ External Examiner
Dr. Gilles Hickson

_____ External to Program
Dr. Rafik Naccache

_____ Examiner
Dr. David Kwan

_____ Examiner
Dr. Malcolm Whiteway

_____ Thesis Supervisor
Dr. Alisa Piekny

Approved by _____
                    Dr. Grant Brown, Graduate Program Director

January 17th, 2023   _____
                                        Dr. Pascale Sicotte, Dean of Faculty

Abstract

Identifying and harnessing mechanisms that are more strongly required for cancer cell division

Kevin Larocque, Ph.D.

Concordia University, 2023

Cancer is the leading cause of death in Canada, and remains difficult to treat since no two cancers are genetically the same. Cancer hallmarks describe the physiological changes that occur to give rise to metastatic cancer, and include uncontrolled cell proliferation and aneuploidy. Many of the current therapies target one or more of these hallmarks, but there is a need to expand the repertoire of available treatments. To do this, it is crucial to identify mechanisms controlling crucial physiological functions that are unique to cancer cells, which could be targeted to block their progression. In my thesis, I reveal that anillin, a cytokinesis protein, is more strongly required in cancer cells with hyperploidy compared to (near) diploid cells. Cytokinesis occurs at the end of mitosis to separate the daughter cells, due to the ingression of a contractile ring. Multiple pathways spatiotemporally control ring position to coordinate it with the segregating chromosomes. We previously discovered a chromatin-sensing pathway where Ran-GTP, which is enriched around chromatin, controls the levels of importins for the cortical recruitment of anillin to control ring position in HeLa cells. We hypothesized that this mechanism depends on ploidy, since HeLa cells are hypotriploid and we saw differences in anillin localization in cells with lower ploidy. In this thesis, I obtained evidence supporting this hypothesis by inducing an increase in ploidy in near diploid HCT116 cells where anillin is not strongly required, and revealing that this causes a change in anillin's localization and its requirement for cytokinesis. I also show how importin-binding is involved for this requirement. These findings reveal that anillin and/or other chromatin sensing pathway components could make ideal targets for novel cancer therapies. In another project, we have been collaborating with Dr. Forgione's lab (Chemistry and Biochemistry) to identify novel compounds with anti-cancer properties. His lab synthesized a family of thienoisoquinoline compounds, and we found several derivatives with high efficacy in cancer cells. We determined the mechanism of action of one of these derivatives, C75, *in vitro* and in cells. I found that C75 binds directly to tubulin and prevents microtubule polymerization *in vitro*. In cells, C75 disrupts

the mitotic spindle, causing cells to arrest in mitosis. I also helped show that it can synergize with other microtubule-targeting drugs, including paclitaxel, which is currently being used to treat cancers. These findings reveal that thieonoisoquinoline compounds could be explored as a potential novel anti-cancer therapy.

<u>Acknowledgements</u>

Dedications

I'd like to dedicate this thesis to my parents, Daniel Larocque and Nathalie Pellerin, who's support was continuous and priceless. Thank you for being the best parents in the world.

I also like to dedicate it to my partner Melissa McAuley. I don't know where I'd be without you.

Publications

Kevin Larocque, Mathieu C. Husser, Su Pin Koh, Natasha Letourneau, Alex Perlman, Noha Skaik & Alisa Piekny. (2022). Anillin's requirement for cytokinesis changes with ploidy. To be Submitted.

Jaunky, D*., **Larocque, K***., Husser, M., Liu, J., Forgoine, P., Piekny, A. (2021). Characterization of a recently synthesized microtubule-targeting compound that disrupts mitotic spindle poles in human cells. *Scientific Reports.* doi.org/10.1038/s41598-021-03076-3. *Equal contribution.

Kashani, S, A., **Larocque, K.,** Piekny, A., Packirisamy, M. (2022). Gold Nano-Bio-Interaction to Modulate Mechanobiological Responses for Cancer Therapy Applications. *ACS Applied Bio Materials*.doi.org/10.1021/acsabm.2c00230

Liu, T, J., Jaunky, B, D., **Larocque, K.,** Chen, F., Sirouspour, M., Mckibbon, K., Taylor, S., Shafeii, A, Campbell, D., Braga, H., Piekny, A., Forgione, P. (2021). Design, structure-activity relationship study and biological evaluation of the thieno[3,2-c]isoquinoline scaffold as a potential anti-cancer agent. *Bioorganic & Medicinal Chemistry Letters*. doi:10.1016/j.bmcl.2021.128327.

Hong, H, S., **Larocque, K**., Jaunky, D., Piekny, A., Oh, K, J. (2018). Dual disassembly and biological evaluation of enzyme/oxidation-responsive polyester-based nanoparticulates for targeted delivery of anticancer therapeutics. *Colloids and Surfaces B.* doi.org/10.1016/j.colsurfb.2018.09.013

Contribution of Authors

Figure 7: Mathieu Husser made the HCT116 and HeLa cell lines where anillin is endogenously tagged with mNeonGreen and made the cartoon in D.

Figure 13: Mathieu Husser designed and cloned the bicistronic vector as well as the cartoon in A.

Table 1 and 2: Jiang Tian Liu synthesized the compounds and Dilan Jaunky performed the IC_{50} experiments.

Figure 16: I previously showed this figure in my MSc thesis (2018).

Figure 19: I previously showed A and D in my MSc thesis (2018). Dilan Jaunky performed the experiments in C, D and contributed to experiments in E.

Figure 20: Mathieu Husser performed the experiments in B and C.

Figure 21: Dilan Jaunky performed the experiments in A. Mathieu performed the experiments in B and C.

Figure 22: Dilan Jaunky performed the experiments.

Figure 23: Dilan Jaunky performed the experiments.

Figure 24: Dilan Jaunky performed the experiments.

Figure 25: I previously showed B and D in my MSc thesis (2018).

Table of Contents

List of Figures

List of Tables

List of Supplemental Figures

Abbreviations

14-3-3	Named for migration pattern on scratch-gel electrophoresis
γ-TuRC	Gamma-tubulin ring complex
a.u.	Arbitrary units
A549	Lung adenocarcinoma human alveolar basal epithelial
ABCB1	ATP binding cassette subfamily b member 1
ACA	Anti-centromere antibody
APC	Anaphase promoting complex
Cdk1	Cyclin-dependent kinase 1
CCS	Cosmic calf serum
CIN	Chromosomal instability index
CLIC4	Chloride intracellular channel 4
CRISPR	Clustered regularly interspaced short palindromic repeats
Cyk4	Cytokinesis defect 4 (also called MgcRacGAP; Rac GTPase activating protein)
DAPI	4′,6-diamidino-2-phenylindole
DMEM	Dulbecco's modified eagle medium
DMSO	Dimethyl sulfoxide
Ect2	Epithelial cell transforming 2
ERM	Ezrin-radixin-moesin
ESCRT	Endosomal sorting complexes required for transport
F-actin	Filamentous actin
FBS	Fetal bovine serum

GAP	GTPase-activating protein
GDP	Guanosine diphosphate
GEF	Guanosine nucleotide exchange factor
GTP	Guanosine triphosphate
HCT116	Human colorectal carcinoma
HeLa	Human cervical cancer from Henrietta Lacks
HFF-1	Human foreskin fibroblast
HRAS	Harvey rat sarcoma virus
HSET/KIFC1	Kinesin family member 1
ICB	Intercellular bridge
ILK	Integrin linked kinase
MAD	Mitotic arrest deficient
MAP	Microtubule associated proteins
MP-GAP	M-phase GTPase-activating protein
MCAK	Mitotic centromere-associated kinesin
MKLP1	Mitotic kinesin-like protein 1
MTA	Microtubule targeting agent
NBS	N-bromo succinimide
NLS	Nuclear localization signal
Plk1	Polo-like kinase 1
PP1	Protein phosphatase 1
PP2A	Protein phosphatase 2A
PRC1	Protein regulator of cytokinesis 1

Ran	Ras-related nuclear protein
RAS	Rat sarcoma virus
RCC1	Regulator of chromosome condensation 1
RhoA	Ras homolog family member A
ROCK	RhoA kinase
S2	Schneider 2 cells
SAC	Spindle assembly checkpoint
SAF	Spindle assembly factor
SAR	Structure activity relationship
sgRNA	Single guide RNA
siRNA	Short interfering ribonucleic acid
TACC3	Transforming acidic coiled-coil protein 3
TCA	Trichloroacetic acid
ch-TOG	Tumor overexpressed gene (also called CKAP5; cytoskeleton-associated protein 5)
TPXL-1	*C. elegans* ortholog of TPX2
TPX2	Targeting Protein for Xenopus kinesin-like protein 2

Chapter 1. Literature review

1.1 Preamble

Cancer is a disease with devastating consequences for our aging population – it has now surpassed heart disease as the leading cause of death of Canadians. All cancers initiate due to uncontrolled cell proliferation, and progressively worsen as they accumulate characteristics that overcome the body's defense systems and enable cancer cells to migrate to multiple locations where they become difficult to treat and have lethal consequences for the patient[1]. While our knowledge of cancer and its complexity have improved over the last few decades, this still has not translated into a significant improvement in how we treat most cancers. This heterogenous disease is never the same in any two patients – so we must treat 'bigger' picture traits. The most successful treatments will either 1) try to re-engage the immune response, 2) trigger the apoptotic machinery, and or 3) target the cell cycle to stop proliferation[2,3]. In none of these cases are the treatments specific – the hope is that cancers are more sensitive to these treatments compared to healthy cells. However, since there are so few targeted chemotherapies that are in use, especially for some types of cancers, there is a need to obtain deeper, more fundamental knowledge of cancers at the cellular and molecular level, and to use this knowledge to develop novel therapies and provide patients with more alternatives. Thus, the overall goal of my thesis was two-fold: to identify mechanisms controlling cytokinesis specifically in cancer cells, and collaborate with medicinal chemists to develop new anti-cancer therapies.

1.2 Sustained proliferation is a cancer hallmark

A cancer cell will accumulate 1000's of mutations over time which favor its propagation and growth. It is estimated that 40% of us will develop cancer in our lifetime and 25% will die from it[4]. It can be difficult to categorize cancers, as their genomic profiles will differ between individuals even for cancers with the same tissue of origin, and the tumours within an individual will be heterogenous both spatially and temporally. Hannahan and Weinberg (2011) defined hallmarks or features that most cancers gain as they progress (Fig. 1)[1,3]. These hallmarks describe the physiological changes that arise in cancers, and involve most of the fundamental processes
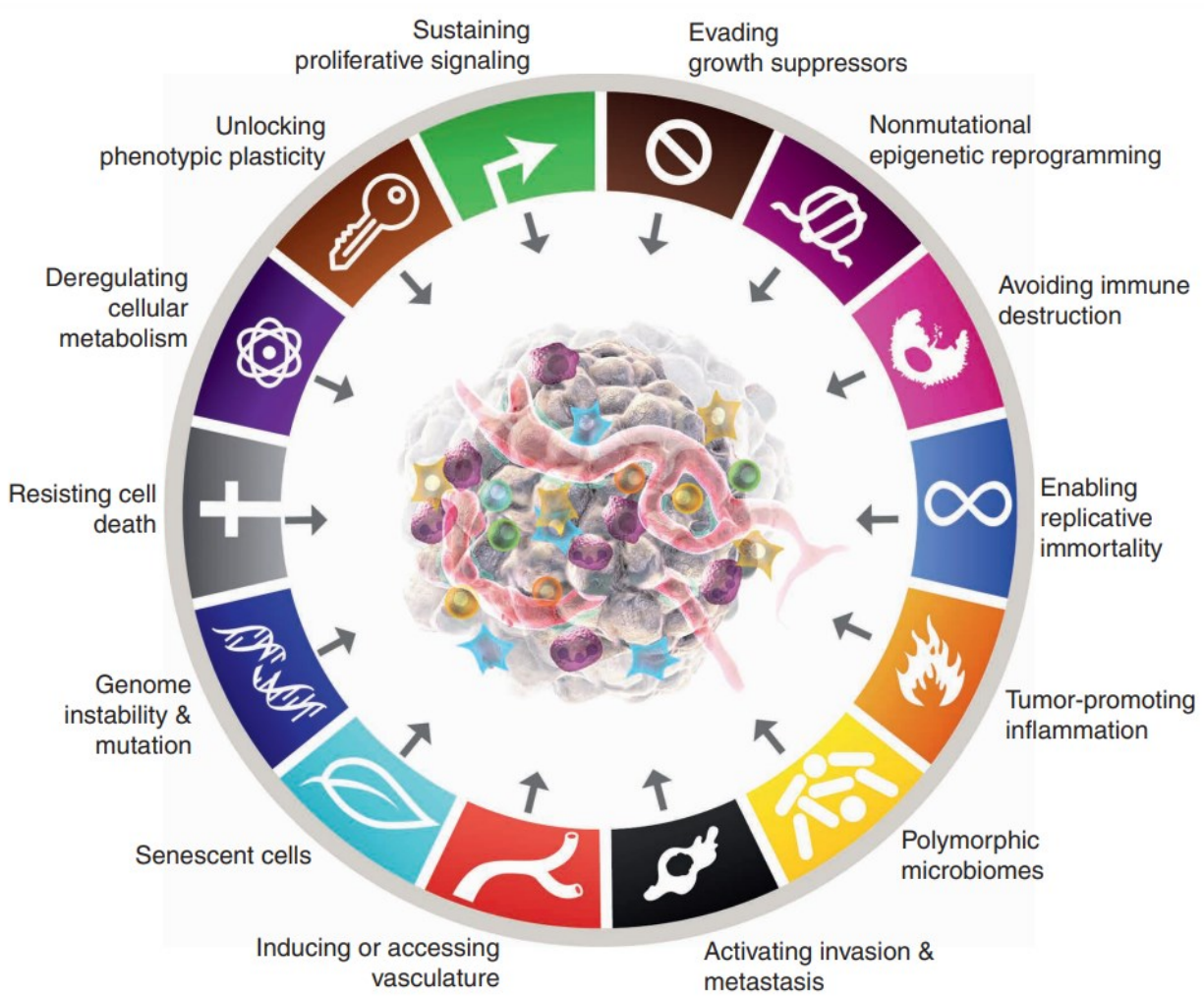
Figure 1: Hallmarks of cancer. A tumour is shown in the middle of the circle containing the 14 most recent characteristics that cancers acquire as they progress. Among these hallmarks, sustained proliferative signaling describes uncontrolled cell cycle entry, while genome instability & mutation describes the accumulation of genetic changes that drive cancer evolution. Figure adapted from Hanahan, (2022)[3].

including sustained proliferation, evasion of apoptosis, evasion of the immune system, changes in cell fate, among others. One of the fundamental hallmarks is sustained proliferation, which occurs when cells no longer respond to cues that typically control cell cycle entry (Fig. 1). Changes include the constitutive expression of growth signals, reduction in inhibitors of cell cycle entry, and the failure to respond to hyperproliferative stress (Fig. 1)[1]. An example of this is the commonly mutated Ras proteins, or its upstream EGF receptor, which typically regulate cell cycle entry by controlling the expression of genes required for cell cycle entry and transcription[5]. In 55% of colorectal cancers, HRAS is constitutively active, causing constitutive cell cycle entry without upstream activation[6]. Another early hallmark is caused by the loss of p53, where cancer cells also lose the ability to undergo apoptosis in response to DNA damage and stress, permitting them to gain genetic and chromosomal instability that can help them evolve more quickly by acquiring additional mutations conferring more hallmarks[7,8]. Interestingly, these same traits also make cancer cells more susceptible to catastrophe[9].

1.3 Mitotic spindle

Mitosis is a crucial step in the somatic cell cycle, with entry and exit being tightly controlled to ensure that daughter cells are formed with the correct genetic (Fig. 2). M phase entry is regulated by an increase in Cdk1 activity. Cdk1 requires binding to Cyclins A and B, and is regulated by multiple phosphorylation events. For example, Cdk1 activity is inhibited via phosphorylation by Wee1 and Myt1 kinase, and the phosphatase Cdc25 removes this inhibitory phosphorylation to release active Cdk1-Cyclin[10]. Cdk1-CyclinA/B has multiple substrates that trigger dramatic changes in cell shape, initiate nuclear envelope breakdown, condense chromatin, and promote centrosome separation and maturation to increase microtubule dynamics for spindle assembly[11]. After chromosomes properly attach to the spindle via their kinetochores, the spindle assembly checkpoint (SAC) is satisfied and triggers mitotic exit[12].

The SAC consists of multiple proteins including Mad1 and Mad2, which are enriched at unattached kinetochores, and prevent mitotic exit until all kinetochores are properly attached and generate tension via pulling forces from each spindle pole on the sister chromatids[12]. Mitotic exit requires the degradation of Cyclin A and Cyclin B to inactivate Cdk1, as well as the degradation of securin to release active separase to cleave cohesins and release sister chromatids[13]. The E3 ligase that is responsible for this degradation is the anaphase promoting complex (APC), which
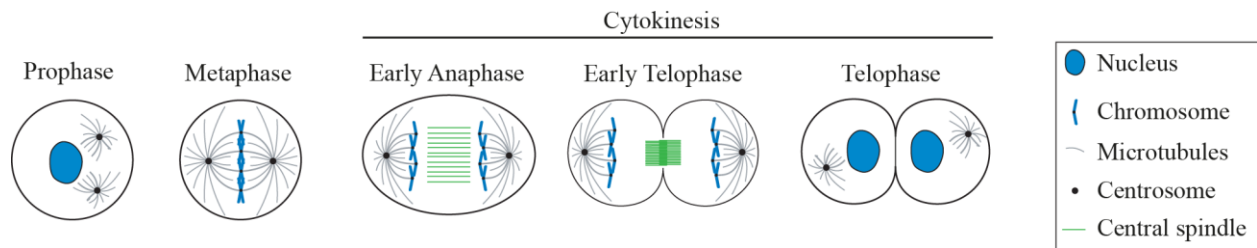
Figure 2: **Eukaryotic cell mitosis.** The cartoon illustrates the different phases of mitosis. The centrosomes separate and nucleate microtubules during prophase. During metaphase, dynamic microtubules assemble into a bipolar spindle that aligns the sister chromatids, which segregate to their respective poles during anaphase. Also during anaphase, the cortex polarizes to form a ring that ingresses in telophase to separate the daughter cells by abscission. The nucleus and chromosomes are shown in blue, microtubules are shown in grey, centrosomes are shown in black, and the central spindle is shown in green.

requires the cofactor Cdc20 for its activity[14]. When Mad1 and Mad2 are still localized to kinetochores, they prevent Cdc20 from binding to the APC[15,16]. When the SAC is satisfied, this triggers APC activation via Cdc20[14,17]. Thus, mitosis is tightly controlled to ensure that sister chromatids are properly aligned and segregated to their respective poles and avoid aneuploidy.

The mitotic spindle is a crucial structure required for proper sister chromatid separation, and its assembly is controlled by hundreds of microtubule-associated proteins (MAPs) and motors[18]. The core spindle structure is formed by microtubules. Microtubules are generally formed by 13 protofilaments of β and α tubulin dimers, which assemble with the β subunit facing the 'plus' end (Fig. 3)[19]. These proteins are GTPases, and when β-tubulin is GTP-bound, this promotes growth, while hydrolysis to the GDP-bound form will promote rapid depolymerization and catastrophe[19–21]. In somatic metazoan cells, microtubules typically grow from the centrosomes, which helps to stabilize the minus ends[18]. At G2/M transition, centrosomes mature through the Aurora A kinase and Plk1-dependent recruitment of the γ-TuRC complex, and separate to opposite poles via the kinesin motor protein Eg5[22–24]. The γ tubulin ring complex (γ-TuRC) is found at the base of centrosomes and nucleates microtubule polymerization [25,26]. Multiple MAPs promote the nucleation, polymerization or depolymerization of microtubules such as TPX2, ch-TOG and mitotic centromere-associated kinesin (MCAK), respectively[18]. Ch-TOG is a microtubule polymerase required for the formation of a bipolar spindle[27]. It has multiple TOG domains capable of binding to tubulin dimers as well as the microtubule lattice[28]. The model is that the outer arms bind to and bring tubulin dimers to the core lattice to facilitate their assembly into a polymer. Through its TOG6 domain, ch-TOG docks to TACC3 at the centrosome where it promotes microtubule assembly based on the local critical concentration of free dimers[24]. Ch-TOG also interacts with another protein called TPX2, which is implicated in microtubule nucleation[18]. This complex localizes to the plus ends of microtubules where they control microtubule assembly at the sites of kinetochore attachments in response to Ran-GTP signaling[29]. Active Ran (Ran-GTP) is generated by RCC1 (Ran GEF), which is tethered to histones, and inactivated by RanGAP in the cytosol[30]. Spindle assembly factors (SAFs) with nuclear localization signals (NLSs – also named because the same system controls nuclear transport) can bind to importins, and Ran-GTP releases importins from these proteins[31,32]. Thus, SAFs, which include TPX2, can be bound to importins and kept inactive at regions of the cytosol away from chromatin, but near chromatin they are released by Ran-GTP where they help to assemble the bipolar spindle[33]. MCAK depolymerizes
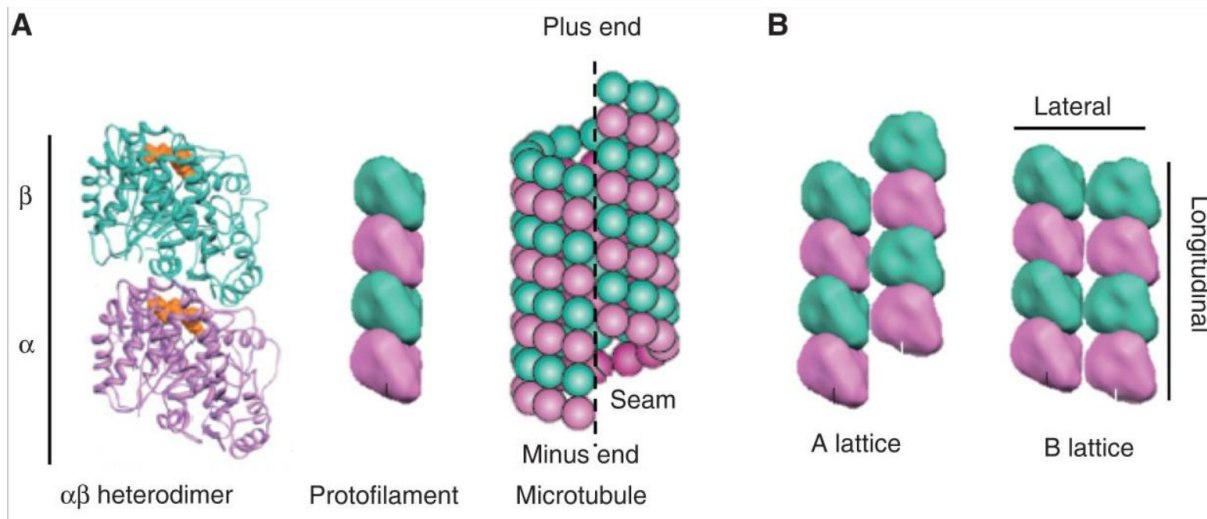
Figure 3: Microtubule structure. A) The structures of α- (purple) and β-tubulin (aqua) as a heterodimer are shown, with the GTP-binding site in yellow. The dimers assemble into a protofilament and microtubule with directionality as shown. B) Microtubules have two types of protofilament alignment referred to as the A and B lattice. The A lattice is found at the seam of the microtubule (left), while the B lattice alignments occur in the main body. The α- and β-tubulin neighbor can change depending on the arrangement. In the A lattice, the α tubulin aligns with β tubulin, and is considered to be a weak point in the microtubule structure. Figured adapted from Goodson and Jonasson, (2018)[19].

microtubules to promote increased dynamics to correct improperly attached kinetochores, and is hypothesized to balance the activity of ch-TOG[34,35]. Depleting ch-TOG causes the formation of multipolar spindles that can be rescued by co-depletion of MCAK, although it is not clear why ch-TOG depletion forms multipolar spindles[35]. This could be because they used HeLa cells, which have fragmented or supernumerary centrosomes that typically cluster to form bipolar spindles, and disrupting microtubules could make these centrosomes prone to de-clustering. The mitotic spindle is an important structure to ensure the proper segregation of sister chromatids, and cells have multiple mechanisms in place that can cause cell cycle arrest if this does not happen properly.

1.4 Targeting the mitotic spindle to treat cancer

Some of the most successful anti-cancer drugs target microtubules and disrupt the spindle[36]. Many of the core microtubule regulators including TPX2 and ch-TOG are highly overexpressed in cancers, causing them to have different microtubule dynamics and these spindles often are prone to having mis-aligned sister chromatids causing mis-segregation and aneuploidy, which helps cancers to progress and evolve[37]. In addition, as mentioned earlier, they often lack the mechanisms to cause cell cycle arrest or apoptosis in response to hyperproliferative stress or improperly attached chromosomes[1]. Therefore, microtubule-targeting drugs are hypothesized to be successful because they decrease microtubule dynamics, making cells prone to mitotic catastrophe.

One of the most common microtubule-targeting drugs that is still in use today is Taxol[TM] (paclitaxel) which prevents microtubule depolymerization[38]. Paclitaxel binds to β tubulin at longitudinal and/or lateral interfaces on the lumen side of the lattice and causes a loss in microtubule dynamics *in vitro*[39,40](Fig. 4). In cells, very little paclitaxel is needed to stabilize polymers, with IC_{50} for toxicity <10 nM in many cancer cells[41]. However, paclitaxel is a highly complex molecule of natural origin, and its solubility is quite poor[42]. In a review by Weaver (2014), she proposed that the intratumoral concentration of paclitaxel was generally too low to cause robust mitotic arrest[38]. This is based on studies showing that there is an increase in multipolar spindles in cells in paclitaxel-treated tissues, suggesting that cells die from mitotic catastrophe[38]. This was further supported by another study showing that mitotic arrest was dispensable to tumor regression, which rather depended on the mis-segregation of chromosomes[43]. While paclitaxel has
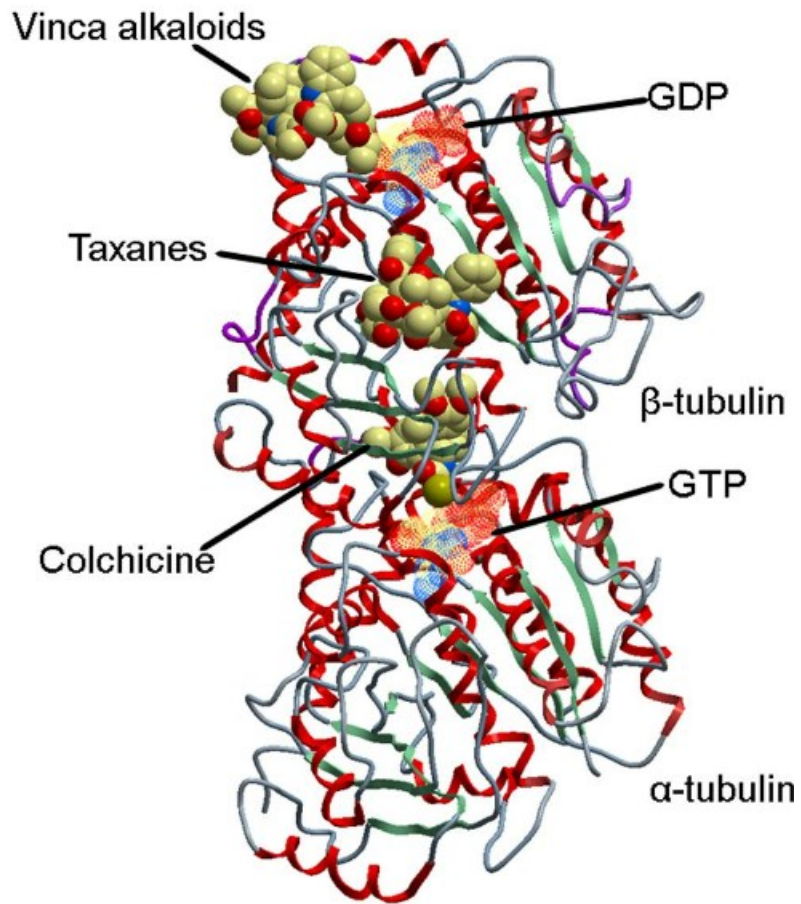
Figure 4: Microtubule targeting drugs. The cartoon shows the structure of the α- and β-tubulin dimer with the binding sites for vinca alkaloids (vinblastine), taxanes (paclitaxel) and colchicine. Figure adapted from Xie and Zhou, (2017)[45].

high efficacy for many different types of cancer cells, it causes severe side-effects and patients often gain resistance leaving them with few other options for treatment[44]. Multiple mechanisms contribute to paclitaxel resistance. It can be removed from cells by ABC transporters, which use ATP to pump out drugs containing recognizable chemical moieties[44,46]. Paclitaxel could also be removed by ABCB1, also called the "hydrophobic vacuum cleaner", which binds to hydrophobic compounds to remove them from cells[46]. Another common strategy is to overexpress the βIII tubulin isoform which increases microtubule dynamics by more than 50% and/or could have lower affinity for paclitaxel[47,48]. Thus, there is a need to increase the repertoire of drugs and develop new therapeutic strategies in therapy. For example, paclitaxel has been improved by coupling it to albumin, or harnessing a lipid-based delivery system to improve retention and reduce the amount of drug needed to achieve high efficacy[49].

Other microtubule-targeting drugs prevent microtubule polymerization and/or promote depolymerization. Many of these drugs are not used to treat cancers because of toxic side-effects. Ones that are currently in use are vinca alkaloids including vincristine and vinblastine[50](Fig. 4). These compounds bind to the interface between tubulin subunits and cause a 'wedge' in the microtubule lattice which destabilizes microtubules to cause catastrophe and inhibits their growth[50–52]. Other drugs, such as colchicine, are not used to treat cancer, but are used to treat inflammation caused by gout, pericardial disease and familial Mediterranean fever among other diseases[53]. This could be because the activation and/or migration of white blood cells are sensitive to microtubule disruption[53]. Colchicine binds irreversibly between α/β tubulin dimers, and is incorporated at the end of the microtubule lattice[53–55](Fig. 4). This addition prevents microtubule growth, and at higher colchicine concentrations causes microtubule depolymerization[54,56,57]. Nocodazole is another compound that disrupts microtubule polymerization, but is not used in the clinic because of serious side-effects[58]. It binds to the same site as colchicine, although could extend more deeply into the β subunit with less affinity for the α subunit[59].

Another characteristic of cancer cells is that they have supernumerary or fragmented centrosomes that cluster to form pseudo bipolar spindles[60]. This clustering machinery is thought to be cancer-cell specific, but is not well-understood. Multiple proteins such as ILK have been shown to be required for clustering, but it is not clear if they are selective for cancer cells[61,62]. For example, epithelial cells often have high numbers of apically localized centrosomes that nucleate

cilia for their function, and could also be sensitive to disruption[63,64]. In general, most of the machinery that regulates spindle microtubules is also required (to some extent) for clustering, suggesting that this is a microtubule-dependent phenomenon[65]. This makes it difficult to determine if the efficacy of the microtubule-targeting drugs described above is due to their effect on spindle microtubules per se, or their effect on clustering. However, HSET/KIFC1 seems to be selectively required for cancer cells, suggesting that there could be microtubule regulators that are differentially required in cancer cells[62]. Despite this exciting finding, inhibitors have not yet had any success in the clinic[66]. There are also many cytokinesis proteins (see next section) that are highly upregulated in cancer cells. It was initially hypothesized that these proteins are simply upregulated to support the high division rates of cancer cells. However, it is becoming clear that these levels are far above what would otherwise be needed to meet threshold requirements, and some proteins, such as anillin are so highly upregulated that they are used as diagnostic markers for some cancers (e.g., pancreatic cancer)[67,68]. Thus, it would be interesting to determine if any of these could be ideal targets, as one may predict that cancer cells rely more heavily on this machinery compared to healthy cells.

1.5 Mitotic exit and cytokinesis

Cytokinesis occurs as the last step in mitosis (Fig. 2). This process requires the assembly and ingression of a contractile ring, which pinches in to physically separate the cell into two daughters[69] (Fig. 5A). This process occurs as a series of events that initiates at anaphase, and proceeds until abscission (Fig. 5A).

Contractile ring assembly and ingression is regulated by the small GTPase RhoA[69]. Active RhoA (RhoA-GTP) is generated at the equatorial cortex by the GEF Ect2, and is inactivated globally by MP-GAP[70](Fig. 5C). Active RhoA binds to effector proteins such as formins and Rho kinase (ROCK) which polymerize linear F-actin and activate myosin, respectively[71]. Active RhoA also recruits anillin to the ring, which is a scaffold protein that is required for ring positioning and/or abscission[72] (Fig. 5C). As described below, Ect2 activity is tightly controlled to ensure that active RhoA is primarily generated in the equatorial plane[69,71]. In addition, multiple pathways restrict the localization of contractile proteins and/or regulators from the polar cortex[73,74]. There are also likely multiple factors that control the kinetics of assembly and ingression, which include actin crosslinkers and cortical flow.
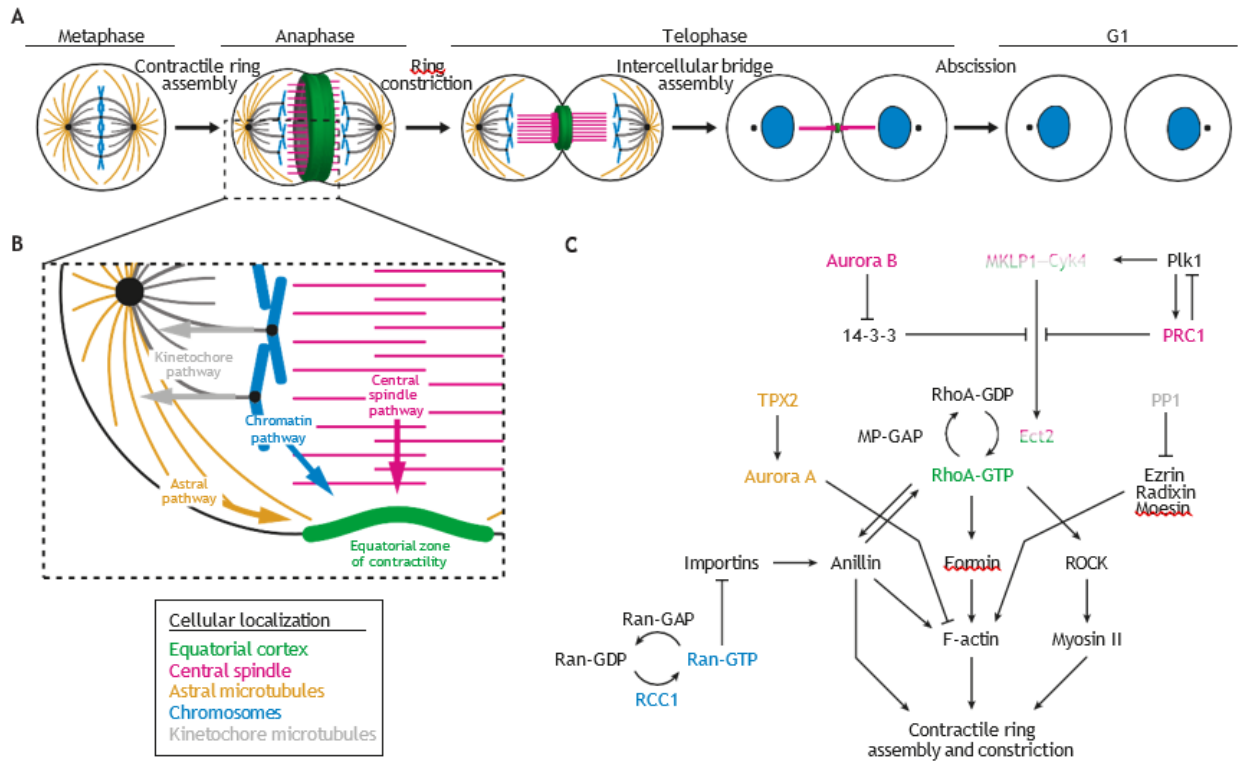
Figure 5: **Overview of cytokinesis**. A) The cartoon schematic shows a cell undergoing mitotic exit from metaphase to anaphase when a contractile ring (green) assembles, then telophase where the ring constricts followed by abscission, which occurs at the intercellular bridge (pink). The astral microtubules are shown in yellow, the chromatin is in blue, and the central spindle is in pink. B) A region of a late anaphase cell is enlarged to show how the different pathways regulate contractile ring assembly. These include the central spindle pathway (pink), chromatin pathway (blue), kinetochore pathway (grey) and astral pathway (yellow). These pathways work together to position the contractile ring equatorially. C) A schematic shows the molecular components of each pathway from B) The central spindle stimulates RhoA activation in the equatorial plane through the regulation of Ect2 to form an actomyosin ring, while the kinetochore and astral pathways prevent the accumulation of anillin, active myosin and/or linear F-actin at the polar cortex. The generation of active Ran near chromatin leads to the equatorial enrichment of importins that recruit anillin for ring positioning. Figure adapted from Husser et al., (2021)[74].

Anillin is required for ring positioning in some cell types. It anchors the contractile ring to the membrane through its multiple interactions that include F-actin, myosin, RhoA, septins and phospholipids among other proteins (Fig. 6)[72]. The loss of anillin causes rings to oscillate and cytokinesis failure in HeLa and *Drosophila* S2 cells[75,76]. However, anillin depletion also causes abscission phenotypes in Drosophila cells. Furthermore, in the early *C. elegans* embryo, depletion of ANI-1 (anillin) only causes mild ingression phenotypes, while it is required for cytokinesis in neuroblast cells during mid-embryogenesis[77,78]. These differences in anillin's requirement and function in cytokinesis could reflect differences in their mechanisms controlling ring assembly components and ingression kinetics. In the two-cell *C. elegans* embryo and in human cells, anillin's cortical localization varies with cell type, and we speculate that multiple parameters play a role including fate, ploidy and size[73,79,80].

Multiple spindle-dependent and -independent pathways control ring assembly and positioning (Fig. 5B). One of the spindle-dependent pathways involves the astral microtubules, and their role in restricting the localization of contractile proteins at the polar cortex. Astral microtubules extend from the centrosome to the polar cortex and prevent proteins like anillin and formins from accumulating nearby[81–83]. The mechanism is not clear, but anillin can directly bind to microtubules and this binding may be enriched in regions of the cell where active RhoA levels are lower[82]. In *C. elegans*, astral microtubules clear anillin from the polar cortex through the activation of Aurora A by TPXL-1 (TPX2) however, it is not clear if this mechanism also occurs in human cells[84]. Astral microtubules also clear F-actin from the polar cortex via inhibition of the Diaph1 formin through binding to the microtubule plus-end CLIP170 protein, and removal of IQGAP1, a cytoskeletal scaffold[83]. Through these functions, astral microtubules induce relaxation of mechanical tension at the polar cortex[85].

Another spindle-dependent pathway is associated with the central spindle, and stimulates the activation of RhoA at the overlying cortex[71](Fig. 5B). The central spindle is formed by anti-parallel bundled microtubules that arise between segregating chromosomes. The centralspindlin complex comprised of a heterotetramer of Cyk4 and MKLP1 helps form the central spindle, but also binds to Ect2[86,87](Fig. 5C). Ect2 is phosphorylated by Cdk1, which is hypothesized to cause it to form an inactive conformation[87,88]. At anaphase onset, the loss of Cdk1 activity, combined with the Plk1-mediated phosphorylation of Cyk4 helps a Cyk4-Ect2 complex to form, which is
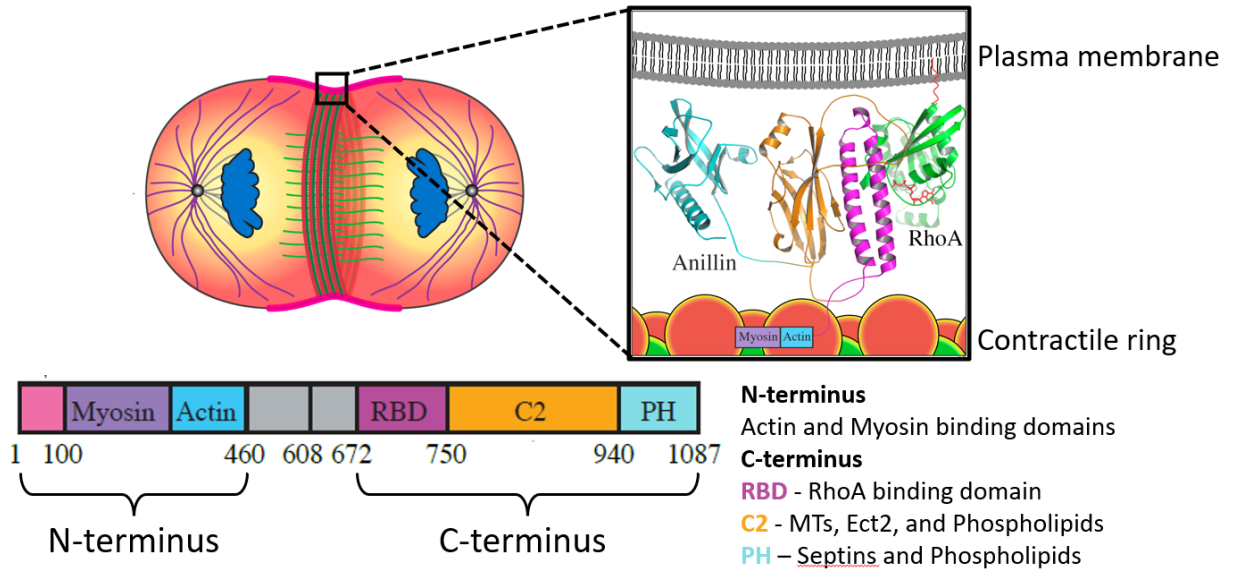
Figure 6: **Anillin structure and function**. The cartoon shows a cell with anillin enriched at the equatorial cortex. The zoomed in region shows a ribbon structure of the C-terminus of anillin (pleckstrin homology; PH domain in light blue, C2 domain in light orange and RhoA-binding domain; RBD in dark pink) interacting with RhoA (green) and connecting to the contractile ring (red and green) via the myosin (purple) and actin-binding (blue) domains in the N-terminus. Underneath, the same domains are shown in the linear structure along with the corresponding residues. Figure adapted from (Beaudet., 2019)[89].

required for Ect2's function in activating RhoA[90]. Furthermore, membrane localization is also required for this activation, since removal or disruption of the lipid-binding domain from Cyk4 or Ect2 prevents active RhoA from being generated[91–93]. It is not clear how centralspindlin-Ect2 becomes membrane-bound. Since centralspindlin is recruited to the central spindle microtubules in part via a PRC1-Kif4A complex, it was shown more recently that Plk1 phosphorylation may partially inhibit PRC1's microtubule binding, which could reduce the affinity of these complexes for the central spindle and cause them to localize to the overlying cortex[94,95](Fig. 5C). At the cortex, Aurora B kinase phosphorylates MLKP1, relieving its inhibition by 14-3-3 protein and permitting the oligomerization of centralspindlin[96](Fig. 5C). Despite the importance of the spindle pathways in controlling ring assembly, contractile rings can often form in the absence of microtubules altogether, supporting that signals can come from other subcellular structures to influence how these proteins localize.

Several pathways associated with chromatin can control the position of the contractile ring. Ezrin-radixin-moesin (ERM) proteins play a critical role in organizing the cortex due their ability to stabilize F-actin and crosslink it to the membrane[97,98](Fig. 5C). ERM proteins are regulated by phosphorylation, and PP1 phosphatase can inactivate moesin through Sds22, which is associated with the kinetochores[98]. Thus, as the sister chromatids segregate, moesin is lost from the polar cortex, leading to a reduction in linear F-actin[98]. CLIC4 is also involved in polar relaxation, and regulates Ezrin phosphorylation although it is not clear if this mechanism is distinct[99]. Another chromatin associated pathway involves Ran-GTP signaling (Fig. 7). As previously described, proteins with NLS's can be bound by importins, which are released in the presence of Ran-GTP (Fig. 7). In anaphase, Ran-GTP is enriched around the segregating chromosomes, and importins are predicted to be enriched at the equatorial cortex where they could influence the function of cytokinesis NLS proteins[32]. Earlier studies showed that Ran-GTP controls cortical polarity in mouse oocytes[100]. Specifically, they showed that the polar body, which extrudes chromosomes during meiosis, forms at a precise distance from DNA[100]. They proposed that Ran-GTP works as a molecular ruler to define the location where cortical changes occur. Our group recently found that Ran-GTP controls ring position for cytokinesis in human cells[101]. Importins can directly bind to and control the recruitment of anillin to the equatorial cortex[101]. We then found that active RhoA induces a conformational change in anillin that makes it more accessible to importin-binding, which in turn facilitates anillin's interaction with phospholipids[102]. However, all of these studies
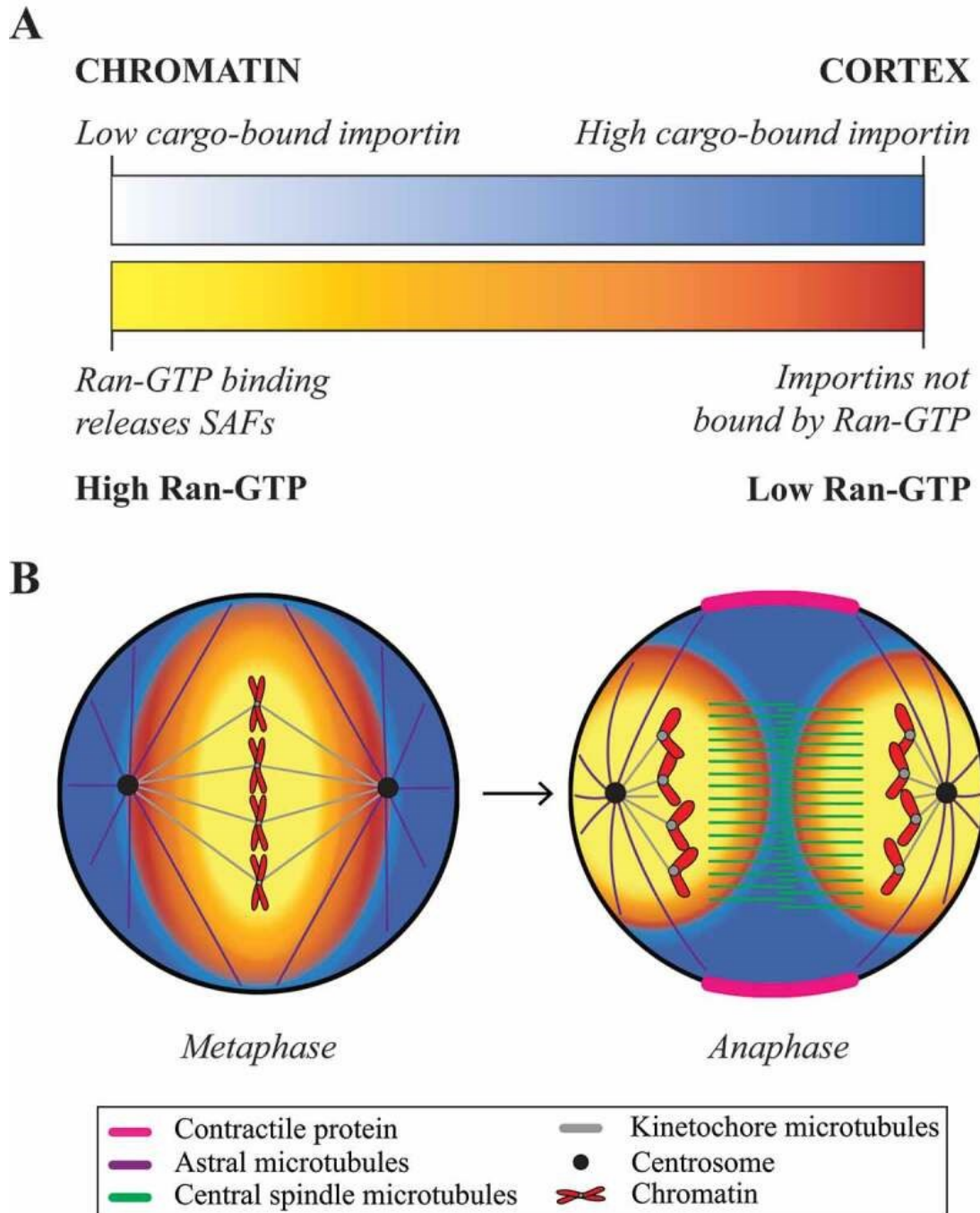
Figure 7: **The Ran and importin gradients in mitotic cells**. A) The inverse relationship between where active Ran and free importins are positioned within a mitotic cell are shown. The dark blue and orange refers to importins that are free to bind to cargo and low active Ran, while the lighter blue and orange refers to Ran-bound importins and high active Ran, respectively. B) The cartoon cells show the change in the Ran-GTP and importin gradients (orange and blue, respectively) as cells transition from metaphase to anaphase. Chromatin is in red, the astral microtubules are in purple, the kinetochore microtubules are in grey and the central spindle is in green. As the chromosomes segregate, importins are predicted to become enriched at the equatorial gradient. Figure adapted from Ozugerin and Piekny, (2020)[103].

were done in HeLa cells, yet, as described earlier, anillin's localization varies with cell type. Thus, we propose that the role of importins in controlling anillin may vary with ploidy, which is explored in Chapter 2 of this thesis.

The last step of cytokinesis is abscission, which relies on the formation of a stable midbody and intercellular bridge (ICB)[104]. As the ring ingresses, components of the ring are shed and/or depolymerized, and the remaining components form a compact structure around the condensed central spindle microtubules to form a midbody. In Drosophila, anillin is required to form a stable midbody[76]. Subsequent studies showed that anillin contributes to midbody ring maturation through the Rho-dependent recruitment of Sticky (citron kinase), which in turns retains anillin at the midbody[105,106]. While it is not clear if human anillin is required for midbody maturation, citron kinase localizes to the cleavage furrow and is required for midbody formation in HeLa cells[107,108]. Furthermore, anillin can form a complex with citron kinase and the overexpression of anillin in HeLa cells causes abscission delays[109]. However, since the loss of anillin causes early cytokinesis phenotypes, it has been difficult to determine if anillin is required for midbody formation and/or stability in HeLa cells. The region of compact midzone microtubules between the two daughter cells is referred to as the intercellular bridge (ICB), and elongates as the midbody matures[104,110]. At this later stage, several proteins are enriched at the midbody or flanking ICB regions which mediate abscission. For example, in HeLa cells, Cep55 localizes in a centralspindlin-dependent manner and recruits ESCRT proteins for secondary ingression and fission[111–113]. Multiple endocytic and secretory vesicles also localize to the midbody through kinesins and dynein motor proteins. FIP3 and RAB35 endosomes are required for ESCRTIII-dependent secondary ingression and to complete abscission[114–116].

1.6 Thesis overview

My thesis addresses several objectives that include determining how the mechanisms controlling cytokinesis vary with cell type and ploidy, and the characterization of a novel family of compounds with anti-cancer activity that preferentially targets cancer cells.

Objective 1. How does the requirement for chromatin-sensing and anillin change with ploidy? In Chapter 2, I used methods such as CRISPR-editing, microscopy and bicistronic vectors to show how the requirement, localization and function of anillin varies with ploidy. I found that anillin is

required for ring assembly and positioning in cells with higher ploidy, while it is required primarily at lower thresholds for stability of the ICB in cells with lower ploidy. I also show how this switch in anillin requirement in cells with higher ploidy is importin-dependent, implicating a preference for the chromatin-sensing pathway in controlling cytokinesis in these cells.

Objective 2. How does a family of rationally designed compounds affect the division of cancer cells? In Chapters 3 and 4, we used biochemical and cell biological methods to characterize a novel family of compounds for their mechanism of action and efficacy in different types of cancer cells grown as monolayers and as multi-cellular tumour spheroids. We found that an active derivative, C75, binds directly to tubulin and prevents microtubule polymerization *in vitro*. It causes multipolar spindle phenotypes and arrests cell in mitosis, with high efficacy for various cancer cell types. C75 synergizes with paclitaxel and colchicine, and causes distinct spindle phenotypes, suggesting that it could be explored further as an anti-cancer therapy.

Chapter 2. The requirement for anillin during cytokinesis changes with ploidy

Kevin Larocque, Mathieu C. Husser, Su Pin Koh, Natasha Letourneau, Alex Perlman, Noha Skaik & Alisa Piekny.

(manuscript in preparation)

2.1 Preamble

We hypothesize that the role of specific pathways controlling cytokinesis changes with parameters including cell size and ploidy. Anillin's requirement and role in cytokinesis varies with cell type and organism. However, prior studies were done independently using different model organisms. We compared anillin's localization in different cultured human cells and found that the timing and breadth of its cortical recruitment varies significantly[80]. Since one of the major differences between these cell lines is ploidy, we explored this further. Here, we induced changes in ploidy in cells with the same genetic background to determine the impact on anillin's localization and function. We also determined how changes in anillin function reflect changes in the requirement for chromatin sensing in regulating cytokinesis. Since many progressive cancer cells have increased aneuploidy, understanding how cell size and ploidy affect anillin function could reveal novel therapeutic targets.

2.2 Abstract

Cytokinesis typically occurs at the end of mitosis to separate the daughter cells. This process occurs due to the ingression of a contractile ring that is positioned between the segregating chromosomes. Multiple pathways control the ring, but it is not known how their relative contribution changes with ploidy. Importantly, most of our knowledge of human cell cytokinesis is derived from HeLa cells, which are hypotriploid. We previously found that a chromatin-sensing pathway, which functions via an importin-gradient, is required in HeLa cells for the localization and function of anillin, which controls ring positioning. We proposed that the requirement for the chromatin-sensing pathway changes with ploidy. In support of this hypothesis, we show that the requirement for anillin increases with ploidy in HCT116 cells. Consistent with this, we also found that the cortical localization of anillin and ring closure kinetics change with ploidy. To demonstrate

that these changes are due to the chromatin pathway, we mutated the importin-binding site (NLS) in anillin and found a reduction in cortical localization and failure to support cytokinesis in cells with higher ploidy. Our findings suggest that as cells gain ploidy, there is a switch in the mechanisms controlling cytokinesis to favor the chromatin-sensing pathway.

2.3 Introduction

Cytokinesis typically involves a series of events that initiate in anaphase with the assembly of a contractile ring that ingresses in telophase to pinch in the membrane, followed by its transition to a stable midbody for abscission. These steps are carefully controlled and involve core machinery that is conserved among metazoans. However, the regulation of this machinery is predicted to change with cell type in response to parameters that include cell size and ploidy[73].

Active RhoA regulates ring assembly and ingression in the equatorial plane[71,117]. The guanine nucleotide exchange factor (GEF) Ect2 generates active RhoA between the segregating chromosomes, which is globally downregulated by MP-GTPase activating protein (GAP)[70,87,118]. Active RhoA binds effector proteins such as formins and Rho-dependent kinase to polymerize actin and generate active myosin, respectively[69,71]. As RhoA-GTP accumulates in the equatorial cortex, linear actin filaments are crosslinked by myosin to form a ring that constricts to pinch in the overlying membrane. RhoA-GTP also recruits anillin, which controls ring position by anchoring the contractile ring to the cortex through its multiple interactions with F-actin, active myosin, active RhoA, septins, and phospholipids among other proteins[72,75]. In support of this function, anillin depletion causes rings to oscillate followed by cytokinesis failure in HeLa and Drosophila S2 cells[75,76]. Anillin also has other functions in cytokinesis depending on the cell type. In *C. elegans* embryos, ANI-1 controls asymmetric ingression and may influence ingression rates by crosslinking actomyosin filaments and/or controlling RhoA signaling[77,119,120]. In *Drosophila* S2 cells, anillin controls the shedding of Rho-anillin-septin complexes and the recruitment of Sticky (citron kinase) for midbody ring maturation[105,106,121]. The Hickson lab also proposed that the shedding of membrane microdomains reduces contractile ring components to facilitate ingression by reducing tension[122]. However, it is not clear if anillin is required for later stages of cytokinesis in human cells. Anillin depletion does not cause abscission failure in HeLa cells, however, anillin can form a complex with citron kinase, and the overexpression of anillin causes abscission delays[107,109,123]. Anillin also recruits septins to the intercellular bridge (ICB), although the

functional requirement for this complex in abscission is not clear[124,125]. These different functions and threshold requirements for anillin suggest that the mechanisms regulating cytokinesis vary with cell type.

Multiple pathways regulate cytokinesis, and the requirement for these pathways is predicted to change with cell type in response to different parameters[73,74]. These pathways work together to enrich contractile proteins at the equatorial cortex. We found that astral microtubules prevent their localization at the polar cortex, while the central spindle stimulates their accumulation between the segregating chromosomes[81,82,87]. Centralspindlin is a complex of Cyk4 (MgcRacGAP) and MKLP1 (kinesin) required for central spindle assembly[86]. Ect2 requires Cyk4-binding to become active, which recruits Ect2 to the central spindle and overlying membrane to activate RhoA[87,91–93,118,126]. While Plk1 phosphorylation of Cyk4 is required for Ect2-binding, this could also trigger the release of centralspindlin from the microtubules to the overlying cortex where it is also regulated by Aurora B kinase[90,95,127]. The spindle-dependent pathways are thought to be dominant in most cell types, but their relative contributions would be expected to vary depending on the timing and spatial distribution of the different sets of microtubules (e.g. large asters vs. large central spindle).

Chromatin-associated pathways also regulate cytokinesis by coordinating ring position with the segregating chromosomes[79,80]. Kinetochore-associated PP1-Sds2 phosphatase dephosphorylates and inactivates moesin, an ERM (Ezrin-Radixin-Moesin) protein that stabilizes F-actin[97,98,128]. Its inactivation reduces F-actin and cortical tension at the nearby cortex[97,128]. ERM proteins also accumulate at the equatorial cortex, where they could play a role in regulating ring kinetics[129]. Another chromatin-associated cue is Ran-GTP, which controls protein function through importins. In interphase, importins bind to the nuclear localization signals (NLSs) in proteins to transport them into the nucleus where high levels of Ran-GTP releases them[32,130]. During mitosis, Ran-GTP is maintained around chromosomes because its activator RCC1 (Ran GEF) is bound to histones, while RanGAP, which downregulates Ran, is cytosolic[30,32,131]. This creates an inverse relationship with importins that are free to bind to NLS proteins near the cortex. Our group recently found that importin-binding is required for anillin localization and function in cytokinesis[101,102]. We also found that active RhoA induces a conformational change in anillin that makes it more accessible to importin-binding, and our model is that this stabilizes anillin's open

conformation to facilitate its interaction with phospholipids at the equatorial membrane[102]. Since these studies were done in HeLa cells, which are hypotriploid, this led us to speculate that the requirement for this mechanism could differ with cell type. Indeed, in the early *C. elegans* embryo, we found that the levels of ANI-1 and its regulation by the chromatin pathway differed between two cell types with different fates[79]. We also found that in one of these cells, there is a correlation with cell size and ring closure kinetics, which relies on the chromatin pathway. This data supports the idea that parameters including cell size and ploidy could change the mechanisms controlling cytokinesis. Human cancer cells with higher aneuploidy tend to have more active Ran, and thus steeper gradients of Ran-GTP and importins, which strongly influence spindle assembly[132]. We also recently reported that anillin's cortical localization changes with cell type[80]. Anillin is already cortically localized at metaphase in near diploid HCT116 cells and broadly localizes to the equatorial cortex in anaphase, while anillin only localizes in anaphase to a narrow region in hyper diploid HepG2 cells[80]. These findings led us to speculate that in cells with higher ploidy, importins only reach a critical threshold to recruit anillin to the equatorial cortex after chromosome segregation in anaphase, while in cells with lower ploidy, importins are more uniform and globally recruit anillin, which then relies on other pathways for its equatorial enrichment.

Here we reveal how ploidy changes the requirement for anillin and its regulation by importins. We found that anillin is more strongly required in HeLa and A549 cells (male, human lung cancer), which are hypotriploid, compared to HCT116 and HFF1 (male, human fibroblast) cells, which are (near) diploid. To determine if this requirement changes with ploidy, we induced an increase in ploidy in HCT116 cells with $CoCl_2$ treatment to induce oxidative stress as previously described[133,134]. We found that HCT116 cells with higher ploidy have stronger requirements for anillin, and the localization of anillin more closely resembles what we had reported for HeLa cells with no cortical localization prior to anaphase and more restricted equatorial localization. We also found that anillin's cortical localization and function in HCT116 cells with higher ploidy depends on importin-binding. Thus, our findings support our model that the chromatin-sensing pathway plays a stronger role in ring positioning in cells with higher ploidy.

2.4 Methods

Cell culture

HeLa (non-edited and mNeonGreen-anillin) and HFF-1 cells were grown in DMEM (Wisent), while A549 cells were grown in F12K media (Wisent) and HCT116 (non-edited and mNeonGreen-anillin; p53-/-) cells were grown in McCoy's media (Wisent). All media was supplemented with cosmic calf serum (CCS; Hyclone) or 10% fetal bovine serum (FBS; Hyclone), with 100 U penicillin (Wisent), and 0.1 mg/mL streptomycin (Wisent). Antibiotics were not included in the media when cells were plated for transfection. Cells were maintained in humidified incubators at 37°C with 5% CO_2. Cells were split using 0.5% trypsin (Wisent) as per standard protocols. Cells were plated at 40% confluency in 6-well dishes on acid-etched No 1.5 glass coverslips (Warner instruments) prior to transfection for microscopy.

Cells were transfected to knockdown or over-express anillin. To knock down anillin by RNAi in different cell types, cells were transfected with 50-100 nM siRNAs using Oligofectamine (ThermoFisher Scientific) as per the manufacturer's protocol. Rescue experiments were done by transfecting cells with bicistronic vectors with a promoter expressing mScarlet-I fused to anillin (wt or KK850DE NLS mutant) and a separate promoter driving the expression of anillin shRNAs using Lipofectamine 3000 and P3000 (ThermoFisher Scientific) as per manufacturer's instructions, except we used 2.5 μL of Lipofectamine with 1.25 ug DNA and 3.2 μL of P3000 per 2 mL well of a 6-well dish. HCT116 cells were transfected in suspension while all other cell lines were transfected 24 hrs after plating. Cells treated with siRNAs were analyzed after 24 hours, while cells treated with shRNAs were analyzed after 48 hours.

To increase aneuploidy, cells were treated with $CoCl_2$. Specifically, HCT116 (p53-/-) were grown to 65% confluency in 35 mm tissue culture dishes and treated twice with 100-150 μM $CoCl_2$ (Sigma-Aldrich) for 24 hrs, with recovery for 48 hrs following each treatment[133,135]. Cells were monitored daily for an increase in cell size, and FACS was used to determine their ploidy (see below).

Generating p53-/- HCT116 cells

HeLa (mNeonGreen-anillin) and HCT116 (mNeonGreen-anillin) homozygous tagged cells were generated as described in Husser et al. (2022)[80]. For this study, HCT116 (mNeonGreen-anillin) cells were edited using CRISPR-Cas9 to introduce p53 loss-of-function mutations. First, the TP53 sgRNA spacer sequence described in Drost et al. (2015)[136] was cloned into the pX459V2.0-HypaCas9-mRuby2 plasmid (Addgene #183872) using previously described

methods[137]. The complementary oligos were: Forward 5'-CACCGGGGCAGCTACGGTTTCCGTC-3' and Reverse 5'-AAACGACGGAAACCGTAGCTGCCCC-3'. The oligo pair were annealed and ligated into the backbone pre-digested with BbsI (New England Biolabs). Positive clones grown from a single cell were confirmed by sequencing. The construct was then transfected as described above into HCT116 cells that were plated at 60% confluency in 6-well plates, with 2 μg plasmid DNA per well. Since Cas9 is fused to mRuby2, cells expressing the red fluorophore were sorted by FACS as described below. mRuby2 single cell positive clones were then expanded from 96-well into 48-well plates. After recovery, the p53 locus was amplified from cells resuspended in the Phire Plant Direct PCR mastermix (ThermoFisher Scientific) and sequenced to verify the presence of mutations. To verify their sequence, PCR products were cloned into the pJET1.2 vector using the CloneJET PCR cloning kit (ThermoFisher Scientific). The clone selected for this study had a pre-existing frameshift mutation in exon 4 of one allele, with a second frameshift mutation generated by CRISPR in the same exon on the second allele.

Cloning for rescue experiments

For rescue assays, a bicistronic vector modified from pX459V2.0-HypaCas9 (Addgene #108294)[138] to contain Golden Gate cloning sites downstream of the U6 and CBh promoters to express shRNAs and proteins of interest in mammalian cells used to co-express an ANLN shRNA and a tagged protein. We used the same shRNA sequence as described in Budnar et al. (2019)[139]. The vector backbone was pre-digested with BbsI and the shRNA sequence was cloned using the following complementary oligonucleotides:

Forward:5'CACCGGGCGATGCCTCTTTGAATAAATTCAAGAGATTTATTCAAAGAGGCATCGCC-3'

Reverse:5'AAAAGGCGATGCCTCTTTGAATAAATCTCTTGAATTTATTCAAAGAGGCATCGCCC-3'

To generate bicistronic vectors expressing anillin (wt) or anillin (NLS mutant; KK850DE), their cDNA, as well as mScarlet-I cDNA (obtained from Addgene #98839)[140] were individually amplified by PCR and cloned into the Golden Gate entry vector pYTK001 (Addgene #65108)[141]. Golden Gate assembly was then used to integrate mScarlet-I and anillin cDNA (wt or NLS mutant)

into the shRNA-containing vector for co-expression in mammalian cells. The Golden Gate assembly reaction was carried out using BsaI (New England Biolabs) using standard protocols[141]. Isolated colonies were picked and screened by PCR, followed by sequencing.

Immunofluorescence

Immunofluorescence was performed to determine the efficiency of RNAi and to monitor cytokinesis phenotypes. Cells were plated at a confluency of 40-50% on glass coverslips pre-washed with isopropanol and acid-treated with 0.1M HCl, then left overnight to adhere. Cells were fixed for immunofluorescence using freshly prepared ice-cold 10%w/v trichloroacetic acid for 14 mins at 4°C. Cells were washed 3 times with PBST (PBS with 0.3% Triton X-100) and kept at 4°C prior to staining. After blocking for 20 minutes with 5% normal donkey serum (NDS) in PBST, 1:400 mouse anti-tubulin antibodies (Sigma Aldrich) and 1:400 rabbit anti-anillin antibodies were added to the cells for 2 hours at room temperature[75]. After washing cells three times with PBST, anti-mouse Alexa 488 and anti-rabbit Alexa 561 secondary antibodies were added at a dilution of 1:400 in PBST with 5% NDS for 2 hours at room temperature. After washing twice with PBST, 4′,6-diamidino-2′-phenylindole dihydrochloride (DAPI, Sigma Aldrich) was added at a 1:1000 dilution in PBS for 5 mins. Cells were then washed once with PBST, followed by a wash with 0.1 M Tris pH 8.8, then 14 μL of mounting media (0.5% propyl gallate in 50% glycerol) was added to each coverslip, which were then added to clean glass slides and sealed with nail polish.

Microscopy

Fixed slides were imaged using the Nikon-TiE inverted epifluorescence microscope with a Lambda XL LED light source for imaging fluorescence in blue to red spectra using a 60x/1.4 PLAN APO oil objective, piezo Z stage (ASI), and a Photometrics Evolve 512 EMCCD camera with Elements acquisition software (Nikon). Optical settings were set based on control cells. Images were acquired at z-planes of 0.5 μm and image files were exported as TIFFs. Images were opened in Image J to make projections from z-stacks and to create merged colour images, which were then converted into 8-bit format and imported into Illustrator (Adobe) to make figure panels.

For live imaging, cells were plated on 25-mm round coverslips and transfected as described above, then placed in a 35-mm Chamlide magnetic chamber (Quorum), or on a 35-mm μ-dish

(ibidi) in 2 mL of media. Cells were imaged on an inverted Nikon Eclipse Ti microscope with a Livescan Swept Field confocal unit (Nikon), using a 60×/1.4 PLAN APO oil immersion objective, 405, 488, and/or 561 lasers, a piezo Z stage (MadCityLabs), and an iXON897 EMCCD camera (Andor). Cells were kept at 37°C with 5% CO_2 using the INU-TiZ-F1 chamber (MadCityLabs). To visualize chromatin, Hoechst 33342 (Invitrogen) was added to a final concentration of 160 nM 45 minutes before imaging. Images were taken every 2 minutes, except for kymographs which were captured every 30 seconds, with multiple z planes of 0.5 μm. Image files were exported as TIFFs, which were then opened in ImageJ for analysis (see below). They were also converted into 8-bit images to generate figures using Adobe Illustrator.

Fluorescence-activated cell sorting

To isolate HCT116 p53-/- cell lines, transfected cells were selected by FACS 24-48 hours after transfection. Since the Cas9 enzyme was fused to mRuby2, single cells expressing mRuby2 were sorted to improve the possibility of obtaining edited clones. To sort, cells were resuspended thoroughly in FACS buffer composed of 1 mM EDTA, 25 mM HEPES pH 7.0 and 1% FBS in PBS, then passed through a 35 μm strainer to remove large cell clumps and transferred to 5 mL FACS tubes for sorting. Cells were added to the FACSMelody cell sorter (BD Biosciences) with gates set to capture individual cells in wells of a 96-well plate containing recovery media [media supplemented with 20% FBS and 1X Penicillin-Streptomycin (50 units/mL Penicillin and 50 μg/mL Streptomycin; Wisent)]. The cells were left to recover for 12 days before expansion and media was supplemented as needed.

FACS was also used to measure the change in ploidy after $CoCl_2$ treatment. Cells were resuspended at a concentration of $5x10^5$ cells/ml in Hank balanced salt solution (HBSS), then treated with 5 μM Vybrant™ DyeCycle™ Ruby (Invitrogen) for 30 minutes at 37°C with 5% CO_2 to stain chromatin as per manufacturer's instructions. Cells were then added to the FACS Melody cell sorter (BD Biosciences) and the proportion of cells with different intensities of the dye were measured and graphed using FlowJo (BD).

Quantification of data

All images were analyzed using ImageJ (NIH). To determine the proportion of cells that failed cytokinesis, cells with one or two nuclei were counted manually using Image J. Numbers were entered into an excel spreadsheet to calculate the average and perform statistical analyses.

To measure cell size, a 5-pixel wide band was drawn around the periphery of metaphase cells, and the area inside the circle was calculated using the measurements tool.

To determine the efficiency of anillin depletion by RNAi, changes in the cortical levels of anillin were measured around the entire cell. Specifically, we measured cells that were ~8 minutes after anaphase onset, when anillin signal had accumulated in the equatorial plane. A 5 pixel-width line was drawn around the perimeter of the cell, and then a macro was used to measure the intensity of the pixels in the line, and to subtract background levels. Then, the average levels in control cells (n=10 and n=15 for near diploid and hyperploidy respectively) were used as the maximum, and the levels remaining in the anillin-depleted cells were calculated as a percentage of this value.

To calculate the ratio of anillin at the cortex compared to the cytosol, three small regions of interest were chosen in each location and the average intensity was measured, then averaged together for each location. The average cortex intensity was then divided by the average cytosol intensity.

To measure the breadth of anillin, a macro was used to perform measurements. Linescans were drawn along each side of the cortex, and the macro measured the intensity of each pixel on the line, then subtracted background levels. Then, the number of pixels above 50% of the maximum intensity were converted into a length (μm; breadth) and divided by the total length (e.g., determined by the total number of pixels) using Prism (GraphPad).

To measure ring closure kinetics, kymographs were created in Image J. To do this we opened timelapse movies of mNeonGreen or mScarlet-anillin taken at 20-30 second intervals, then drew a region of interest that included the equatorial plane. A modified macro was used to measure the distance between two sides of the initial ring from anaphase onset until the membranes appeared to meet[79]. The distance between the two sides for each timepoint was measured by a line, and the number of pixels in the line was converted into um. The values were then normalized so that the distance at anaphase onset was set to 0% ring closure, while 100% closure was when the membranes touched. The data was then plotted on a graph using Prism (GraphPad). To determine

the different phases of ingression, the second derivative of the curve was measured using the line of best fit determined by Prism (GraphPad) analysis function.

Statistical analysis

We carried out the following statistical analysis for each dataset. To determine if the proportion of binucleate cells for the control and RNAi treatment for each cell type was significantly different, we performed a multiple unpaired t test analysis, with significance $p<0.05$ (Fig. 8A). We then compared the proportion of binucleate cells after RNAi treatment between the different cell types using a Welch and Brown-Forsythe one-way ANOVA with Dunnett's T3 multiple comparisons test with significance $p<0.0001$ (Fig. 8A). To determine if there was a significant difference in levels of anillin corresponding to the different phenotypes, we performed an unpaired two tailed Welch's t test (Fig. 9B). To show that the size of HCT116 cells changed after gaining ploidy, a Welch and Brown-Forsythe one-way ANOVA with Dunnett's T3 multiple comparisons test was performed (Fig. 10A). To compare the ratio of cortical anillin in the different cells, a Welch and Brown-Forsythe one-way ANOVA with Dunnett's T3 multiple comparisons test was used (Fig. 11B). To determine if the breadth of anillin significantly changed, we performed an unpaired two tailed Welch's t test (Fig. 11C). To compare the difference in the duration of overall ingression, and the ring assembly phase, a Welch and Brown-Forsythe one-way ANOVA with Dunnett's T3 multiple comparisons test was used (Fig. 12B). To determine if the breadth of anillin was significantly different for the NLS mutant compared to control, we performed an unpaired two tailed Welch's t test (Fig. 13B). A Fisher exact test was performed to compare the proportion of binucleate cells expressing wt vs. NLS mutant anillin (Fig. 13C).

2.5 Results

The threshold requirement and function of anillin in cytokinesis changes with cell type

We determined if the requirement for human anillin changes with cell type. Human anillin has primarily been studied in HeLa cells, with little knowledge of its requirement in other cell types[75]. We recently found that the localization of anillin varies with cell type; while it is cortical in metaphase HCT116 cells, it only localizes to the equatorial cortex in HeLa and HepG2 cells[80]. We hypothesized that changes in ploidy or size may control these differences. To determine if the requirement for anillin changes with cell type, we performed anillin RNAi in four different human

27

cell lines [HFF-1 (male foreskin fibroblast), HeLa (female cervical adenocarcinoma), A549 (male lung carcinoma), and HCT116 (male colorectal carcinoma)]. We chose these cell lines because they have different tissues of origin and different ploidy; HFF-1 and HCT116 are diploid or near diploid (with 46 and 45 chromosomes, respectively), while A549 and HeLa are hyperdiploid or hypotriploid (with 66 and 82 chromosomes, respectively). When cells fail cytokinesis, they have two nuclei within a single cytoplasm, and we counted the proportion of binucleate cells after anillin RNAi. As shown by the graph, and representative field-of-view images of the different cell lines, we found that anillin depletion caused a significantly lower proportion of HCT116 and HFF-1 cells (20 and 22%, respectively) to fail cytokinesis compared to A549 and HeLa cells (47% and 67%, respectively; Fig. 8A,B). To determine if the difference in cytokinesis failure was due to transfection efficiency, we performed a western blot to measure the levels of anillin after knockdown. We found that the extent of anillin knockdown was similar between the different cell types (Fig. S1). These results show that some cell types have stronger requirements for anillin compared to others.

Next, we determined the threshold levels of anillin required to support cytokinesis in HCT116 and HeLa cells. While our anillin knockdown was efficient at the population level, there could still be differences in the knockdown efficiency at the single cell level. We recently reported the CRISPR-editing of these cell lines to endogenously fuse mNeonGreen (mNG) with anillin, and characterized the differences in anillin localization during mitosis (Fig. 8D)[80]. We used these cell lines to measure the levels of endogenous anillin in HCT116 and HeLa cells after anillin knockdown by RNAi. To do this, we imaged mNG-anillin in HCT116 and HeLa cells treated with anillin siRNAs and stained with Hoechst (to visualize chromatin, magenta) from anaphase onset until the end of cytokinesis. We measured the levels of anillin ~8-10 minutes after anaphase onset, when it is typically enriched at the equatorial cortex, and determined the percentage of anillin remaining compared to the average levels in control cells (Fig. 9A)[80]. We found that RNAi-treated HeLa cells with <41% anillin failed cytokinesis compared to cells with higher levels which succeeded, while RNAi-treated HCT116 cells failed cytokinesis with <12% anillin (Fig. 9A,B). These values support what we observed at the population-level. In addition, while all HeLa cells failed cytokinesis with rings that partially ingressed and oscillated as reported previously[75], we observed two major phenotypes in HCT116 cells: 1) rings ingressed and regressed prior to midbody formation, and 2) late regression (Fig. 9B). We observed the earlier phenotype in cells

A
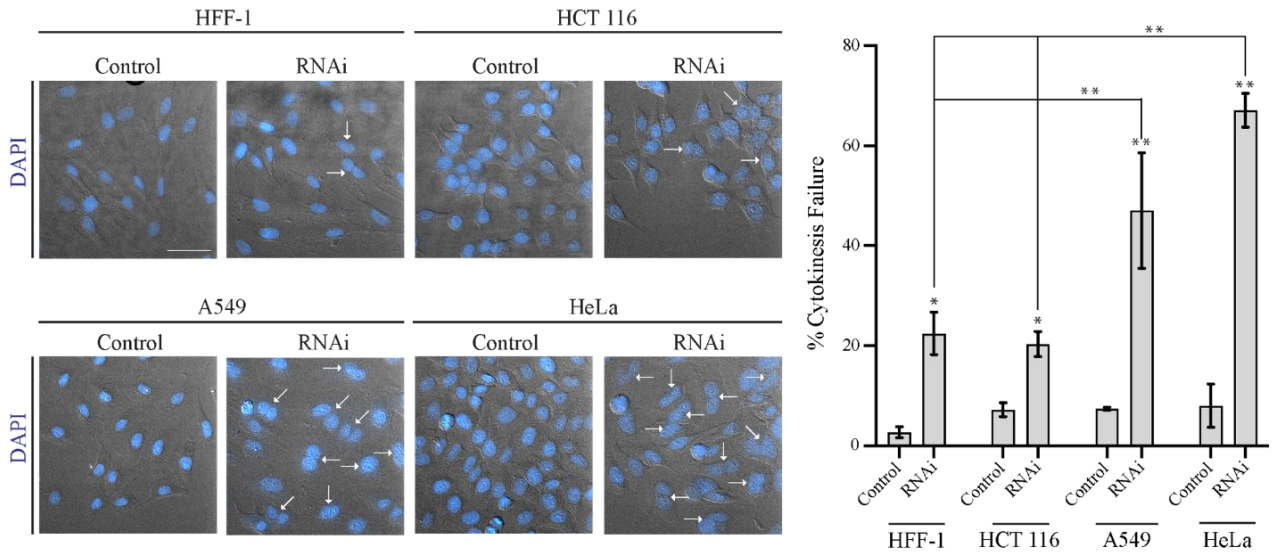
B
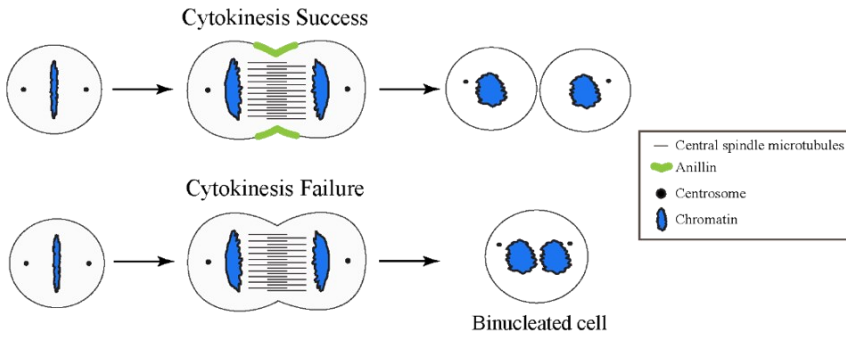
C
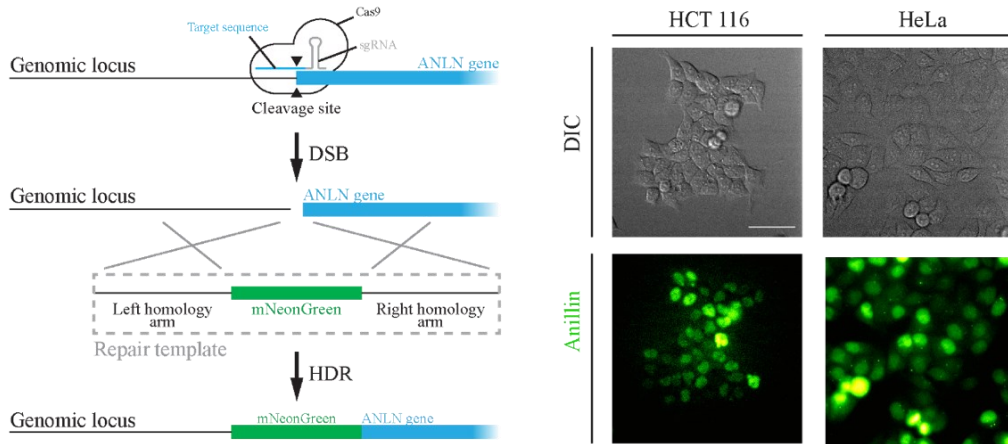
Figure 8: Anillin's requirement for cytokinesis varies with cell type. A) DIC images on the left show fields of view of HFF-1, HeLa, A549 and HCT116 control fixed cells and after anillin RNAi. The nuclei are stained with DAPI (chromatin; blue) and white arrows indicate binucleate cells. The scale bar is 50 μm. On the right, a bar graph shows the proportion of control or anillin RNAi cells that failed cytokinesis (binucleate) for HFF-1 (control, n=198; RNAi, n=188), HCT116, A549 and HeLa cells (control, n=200; RNAi, n=200 per cell line). The bars show standard deviation. Statistical significance is indicated for comparisons between control and RNAi cells for each line, and for RNAi cells between the different cell types (*$p<0.05$, ** $p<0.0001$, ns = not significant). B) A cartoon schematic shows a cell completing cytokinesis successfully to produce two mononucleate daughters, and a cell failing cytokinesis to form a binucleate cell. C) On the left, a cartoon schematic shows the CRISPR-Cas9 mediated endogenous tagging of the anillin locus with the repair template in human cells. The repair template contains the mNeonGreen cDNA flanked by homology arms from the anillin locus. DIC images on the right show fields of view of the anillin-mNeonGreen tagged HeLa and HCT116 cell lines (mNeonGreen-anillin in green). The scale bar is 50 μm.
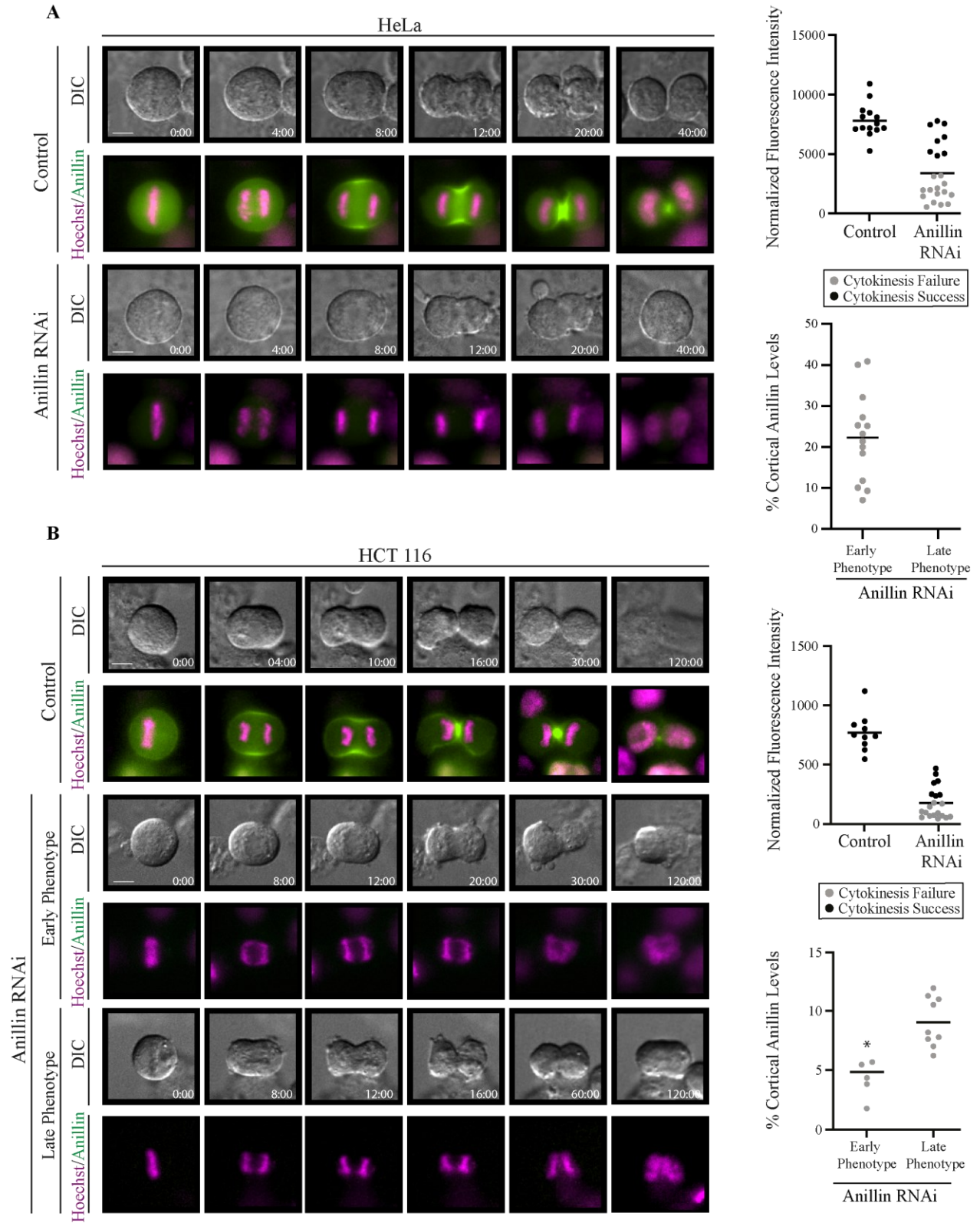
Figure 9: Anillin has different threshold requirements and functions in cytokinesis in HeLa and HCT116 cells. A) and B) Timelapse DIC and fluorescence images show endogenous mNeonGreen-anillin (green) control or anillin RNAi HeLa (A) or HCT116 (B) cells undergoing cytokinesis (Hoechst stains chromatin, magenta). Times are shown in minutes and the scale bar is 10 μm. On the right, dot plots show the normalized fluorescence intensity (a.u.) of anillin in control (n=15) and anillin RNAi HeLa cells (n=22; A) and in control (n=10) and anillin RNAi HCT116 cells (n=20; B). The cells that failed cytokinesis are in grey, and those that succeeded are in black. Also shown are dot plots for the % of cortical anillin remaining in HeLa or HCT116 cells with early vs. late cytokinesis phenotypes. Statistical significance is indicated (*; $p = 0.0004$).

with <6% anillin, while we observed the later phenotype when anillin levels were between 6-12% (Fig. 9B). Our data suggests that anillin is more strongly required in HeLa than HCT116 cells for cytokinesis, and has multiple functions in cytokinesis, similar to Drosophila S2 cells[76]. Our data also shows that the threshold levels of anillin required for these functions are different; less anillin is required for the ring-midbody transition compared to midbody stability. This is the first time, to our knowledge, that anillin was shown to be directly required for the late stages of cytokinesis in human cells.

The requirement for anillin increases with ploidy in HCT116 cells

Our data supports that anillin is more strongly required for cytokinesis in some cell types compared to others. Although the cells we tested have different genetic backgrounds, cells with higher ploidy have stronger requirements for anillin. Thus, we speculate that an increase in ploidy could change the requirements for the pathways controlling cytokinesis. We previously found that the chromatin sensing pathway coordinates the ring with the segregating chromosomes in HeLa cells[101]. In this pathway, importin-binding controls the equatorial localization and function of anillin in cytokinesis[101,102]. We speculate that cells with higher ploidy, such as HeLa, rely more on the chromatin pathway to position the ring compared to diploid cells where spindle-dependent mechanisms may be more dominant. Since the cell lines have different genotypes that could influence pathway requirements, we determined how increasing ploidy in the same cell type changes the requirement for the chromatin pathway. We induced an increase in ploidy in HCT116 cells (mNG-anillin), since they have lower requirements for anillin and are near-diploid. Before inducing ploidy, we mutated p53 to be loss-of-function on both alleles to avoid senescence[142]. Then, we treated the mNG-anillin; p53-/- cells with $CoCl_2$ to cause a stress response similar to hypoxia, which typically triggers a mechanism that involves G2 phase-arrest[133,134]. After treatment, we observed a population of cells that were variable in size, with some that were ~1.5x larger compared to the control cells, and similar in size to HeLa cells (Fig. 10A). To confirm that their increase in size reflects an increase in ploidy, we performed FACS, and indeed saw a population of hyperploid cells that was not present in the control cells (Fig. 10B). Next, we determined how the requirement for anillin changes with ploidy by using anillin RNAi against the mixed population of lower and hyperploidy cells. Anillin depletion in the larger cells caused an increase in cytokinesis failure compared to the smaller cells (51% vs. 14%; Fig. 10C; Fig. S2).

33
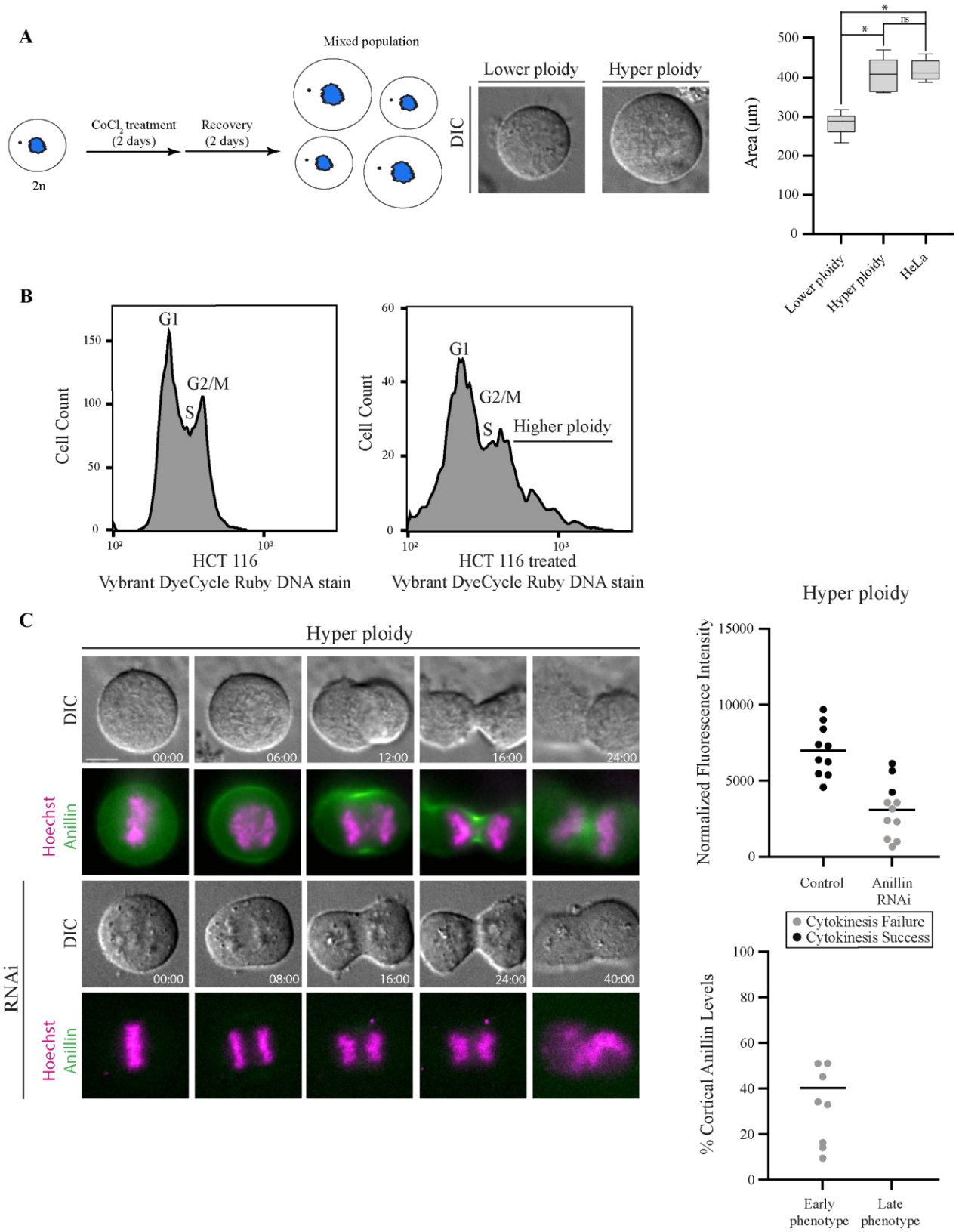
Figure 10: The requirement for anillin increases with ploidy. A) A cartoon schematic shows the workflow to generate HCT116 (mNeonGreen-anillin; p53-/-) cells with higher ploidy using CoCl$_2$ treatment. The DIC images show mitotic cells of different sizes. Times are shown in minutes and the scale bar is 10 μm. The box and whiskers plot shows the area of HCT116, hyperploidy HCT116 and HeLa cells (n=15 for each cell type). Lines show standard deviation and significance is indicated (*p<0.0001; n.s. = not significant). B) Graphs show flow cytometry of cells stained with a DNA dye Vybrant™ DyeCycle™ Ruby (fluorescence intensity; X-axis) and the corresponding stages of the cell cycle G1, S and G2/M (Y-axis). The peaks with hyperploidy cells are indicated. C) Timelapse fluorescence (and DIC) images show control or anillin RNAi mNeonGreen-anillin in HCT116 cells with hyperploidy undergoing cytokinesis (Hoescht to stain chromatin, magenta). Times are shown in minutes and the scale bar is 10 μm. On the right, dot plots show the normalized fluorescence intensity (a.u.) of anillin in control (n=10) or RNAi (n=11) hyperploidy cells. The cells that failed cytokinesis are in grey, and those that succeeded are in black. Also shown are dot plots for the % of cortical anillin remaining in hyperploidy cells with early vs. late cytokinesis phenotypes.

These results show that increasing ploidy caused an increase in the requirement for anillin to support cytokinesis in HCT116 cells.

Anillin localization and ring closure kinetics change with ploidy in HCT116 cells

To determine why the requirement for anillin changes with ploidy, we examined differences in anillin localization in the hyperploidy HCT116 (mNG-anillin; p53-/-) cells compared to control HCT116 (mNG-anillin; p53-/-) cells that are near diploid. To do this we performed live imaging of anillin in cells co-stained with Hoechst to visualize chromatin from anaphase onset through cytokinesis (Fig. 10A). The movies revealed several differences in anillin localization; while it was cortical in metaphase and early anaphase in cells with lower ploidy, it was only visible at the cortex at later timepoints in cells with higher ploidy, where it also appeared to be more narrowly distributed. To quantify this, we drew linescans along each side of the cortex as shown in Fig. 11A, and anillin intensity was measured and plotted vs. cell length in μm starting at anaphase onset (time = 0 minutes) and every 2 minutes until peak accumulation of anillin was reached (8 minutes for smaller control cells, and 12 minutes for larger cells; Fig. 11A). Indeed, the cortical signal in the larger cells became visible after 4 minutes, and remained narrow compared to the smaller cells (Fig. 11A). To compare the differences in anillin's cortical localization prior to anaphase onset, we measured the ratio of cortical anillin vs. cytosol. We found that while the average ratio was 1.39 in near diploid HCT116 cells, it was lower in hyperploidy HCT116 cells, which was similar to HeLa cells (1.00 and 0.89, respectively; Fig. 11B). Thus, there is a clear cortical enrichment in HCT116 cells prior to anaphase onset that is reduced with an increase in ploidy. We also compared the difference in the breadth of anillin just prior to furrow ingression (6 minutes in near diploid HCT116 cells and 8 minutes in HCT116 cells with higher ploidy). We measured the number of pixels with intensities above 50% of the peak levels as a proportion of the total number of pixels (cell length) (Fig. 11A). Indeed, we found that the average breadth was significantly smaller in the larger HCT116 cells with hyperploidy compared to the smaller near diploid cells (14.5 vs. 30.5%). Therefore, the cortical localization of anillin is more restricted to the equatorial plane in HCT116 cells with higher ploidy. This delayed timing and restricted spatial distribution of anillin in cells with higher ploidy could indicate that the chromatin pathway plays a stronger role in these cells.

An increase in the reliance on the chromatin pathway in cells with higher ploidy could
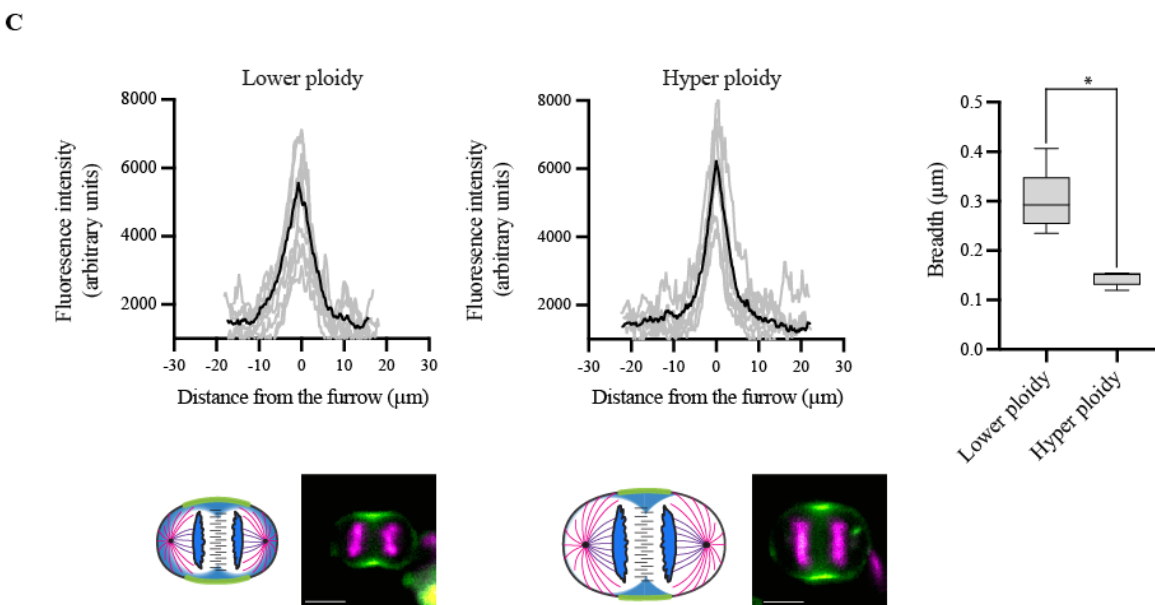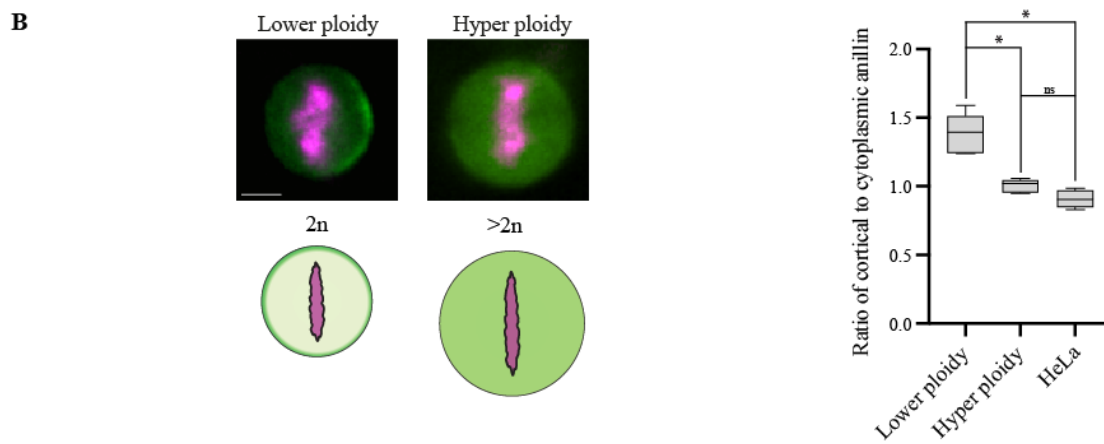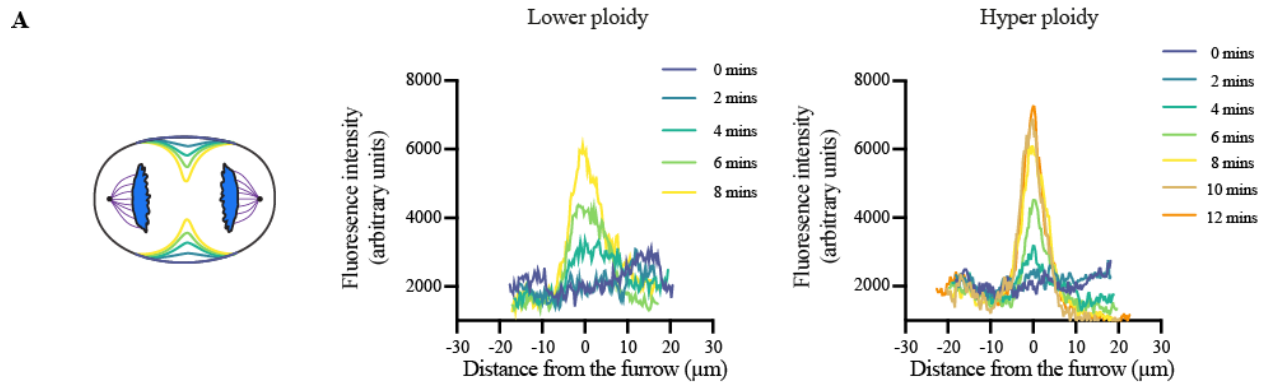
A

Lower ploidy | Hyper ploidy

B

Lower ploidy | Hyper ploidy

2n | >2n

C

Lower ploidy | Hyper ploidy

Figure 11: The cortical localization of anillin changes with ploidy. A) A cartoon cell illustrates the change in the equatorial plane (different colours) until the furrow is partially ingressed (chromatin in blue; kinetochore microtubules in purple). On the right, the graphs show linescans of cortical anillin in a HCT116 (mNeonGreen-anillin; p53-/-) cell with lower (left) and hyperploidy (right). The colours represent the different timepoints as indicated from 0 min (anaphase onset) and every two minutes until the furrow partially ingressed. B) Images show live metaphase HCT116 (mNeonGreen-anillin; p53-/-) cells with lower vs. hyperploidy co-stained with Hoescht (magenta; chromatin). Cartoon cells show the difference in cortical and cytosolic anillin (green; chromatin in magenta) in cells with lower vs. hyperploidy. A box and whiskers plot shows the ratio of cortical to cytosolic anillin in HCT116 cells with different ploidy and HeLa cells (n=10 for each cell line; * $p<0.0001$; ns = not significant). C) Graphs show linescans of cortical anillin fluorescence intensity (a.u.) at furrow initiation (6 mins) for HCT116 cells with different ploidy (n=10 cells per graph). To the right, a box and whiskers plot shows the breadth of anillin at the furrow for HCT116 cells with different ploidy as indicated. Bars show standard deviation (* $p<0.0001$). Fluorescence images show live HCT116 (mNeonGreen-anillin; p53-/-) cells with lower (left) and higher ploidy (right; anillin in green, chromatin in magenta) just prior to ingression. Cartoons highlight differences in the cortical localization of anillin (green), chromatin (blue), importins (pink).

ensure that the ring is properly positioned between the segregating chromosomes. The switch in mechanisms controlling the ring could be reflected by differences in assembly kinetics. To measure ring closure kinetics, we performed timelapse imaging of near diploid and hyperploid HCT116 (mNG-anillin; p53-/-) cells with higher temporal resolution (z-stacks collected every 30 seconds), then created kymographs that we used to measure ring closure over time (Fig. 12A). First, we saw that ring closure took longer in the hyperploid HCT116 cells (21.2 minutes) and HeLa cells (26.7 minutes) compared to the near diploid HCT116 cells (16.8 minutes; Fig. 12A,B). We noticed that the ring closure curves were shifted for each cell type. Different parts of the curve represent the different stages of ring closure; the plateau at the beginning corresponds to the ring assembly phase, followed by a transition to furrow initiation/indentation phase when the formed ring begins to generate force that pulls in the membrane, and the constriction phase when the ring ingresses[79]. To measure these phases, we calculated the inflection points of the curve for the different cell types (see methods). We found that ring assembly took an average of 153 seconds in near diploid HCT116 cells, and longer in hyperploidy HCT116 cells and HeLa cells (321 and 433 seconds, respectively; Fig. 12B). Thus, our data shows that in cells with increased ploidy, there is a significant increase in the overall duration of cytokinesis, which is likely due to the increase in time needed for ring assembly. We speculate that this is due, at least partly, to the delayed accumulation of anillin at the equatorial cortex to ensure that the ring is properly positioned between the segregating chromosomes.

The requirement for the chromatin pathway increases with ploidy in HCT116 cells

Our model is that in cells with higher ploidy, the levels of importins that are sufficient to facilitate anillin's cortical localization are restricted to the equatorial plane during mid-late anaphase, while importins already meet that threshold prior to anaphase in cells with lower ploidy. To test this model, we mutated the NLS in anillin (850KK851 to DE; NLS mut) so that it can no longer bind to importins, and performed rescue assays using this mutant construct[101]. To do the rescue assays, we designed a bicistronic vector that co-expressed shRNAs to knockdown endogenous anillin and mScarlet-I fused to RNAi-resistant anillin (wt or NLS mut; Fig. 13A). As expected, mScarlet-I-anillin (wt) localization in 'rescued' near diploid or hyperploid HCT116 (mNG-anillin; p53-/-) cells was similar to control cells (Fig. 13A). However, mScarlet-I-anillin
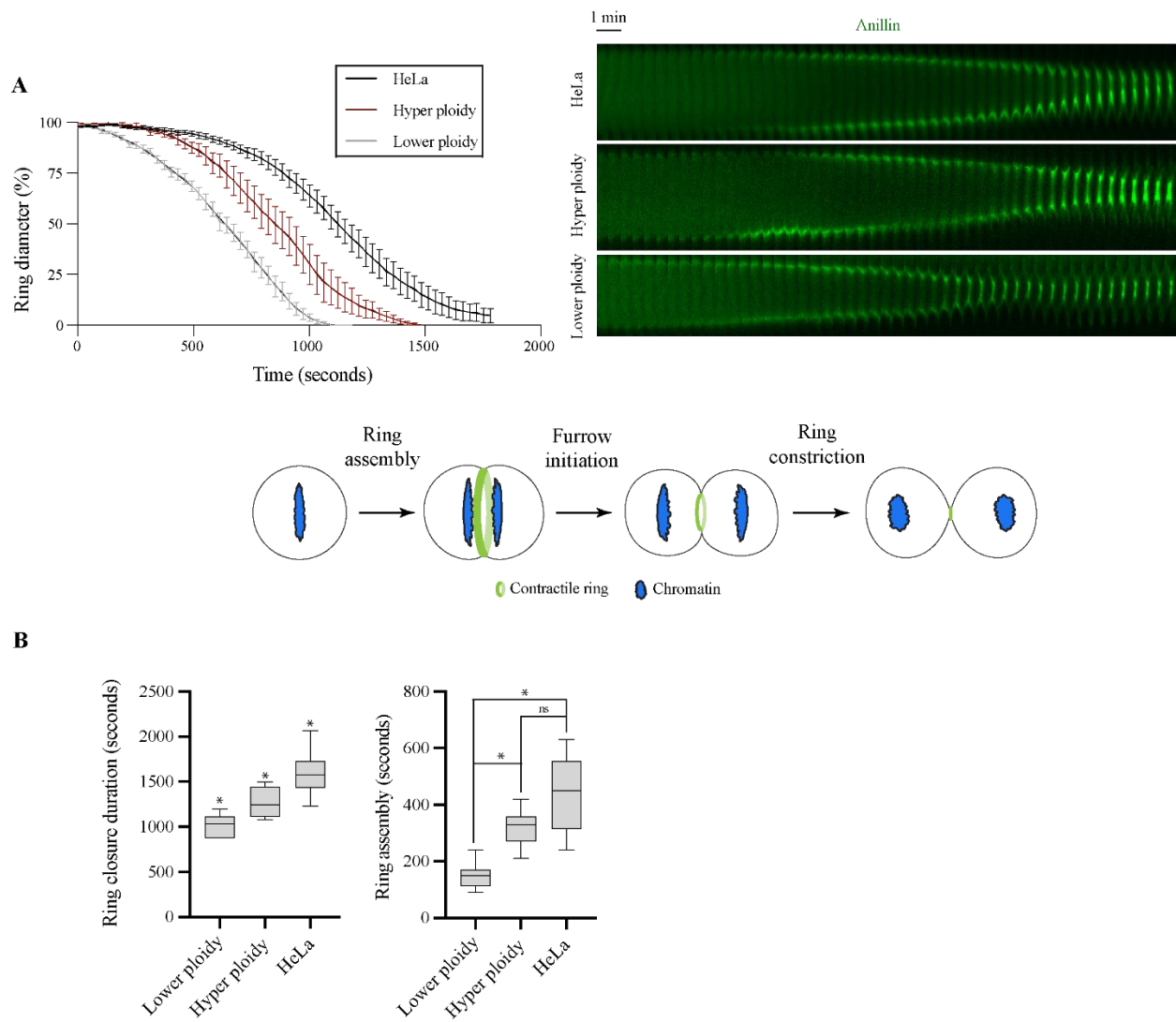
Figure 12: Ring assembly takes longer in cells with higher ploidy. A) A line graph shows the change in ring diameter (%) as a measure of ring closure over time (seconds) for HCT116 (mNeonGreen-anillin; p53 -/-) cells with different ploidy and HeLa cells (n=10 for each). Representative kymographs of mNeonGreen-anillin are shown to the right, taken from a region-of-interest at the equatorial plane at time intervals of 30 seconds. A cartoon shows the different stages of ring closure; ring assembly, initiation and constriction. B) A box and whiskers plot shows the overall duration of ring closure in the cells from A), and the plot to the right shows the duration of ring assembly. The bars show standard deviation (*$p<0.001$; ns = not significant).

A Rescue HCT116 cells

Hoechst / Anillin^WT

Hoechst / Anillin^NLS Mut

B Rescue hyper ploidy HCT116 cells

DIC

Hoechst / Anillin^WT

DIC

Hoechst / Anillin^NLS Mut

RNAi

C

Metaphase   Anaphase   Late anaphase

>2n

2n

— Central spindle microtubules
— Astral microtubules
\ K-microtubules
▶ Anillin
● Centrosome
◗ Chromatin
▨ Ran-free importins
▢ Ran-bound importins

Figure 13: Importin-binding is required for anillin's function in cytokinesis in cells with higher ploidy. A) Timelapse images show HCT116 (mNeonGreen; p53-/-) cells co-expressing RNAi-resistant wt (top) or NLS mutant anillin (bottom; orange) with anillin shRNAs and stained with Hoechst (chromatin, magenta). Times are shown in minutes and the scale bar is 10 µm. To the right, a schematic shows the bici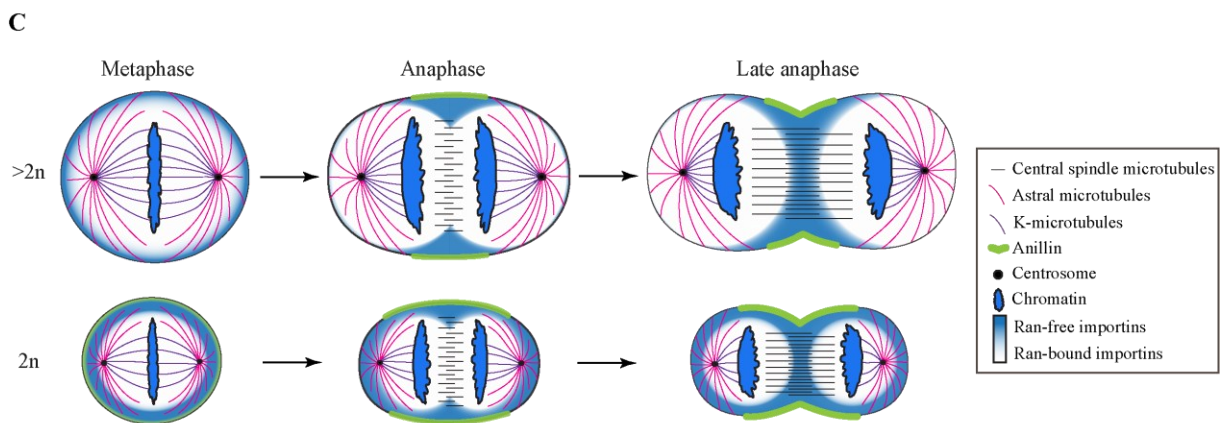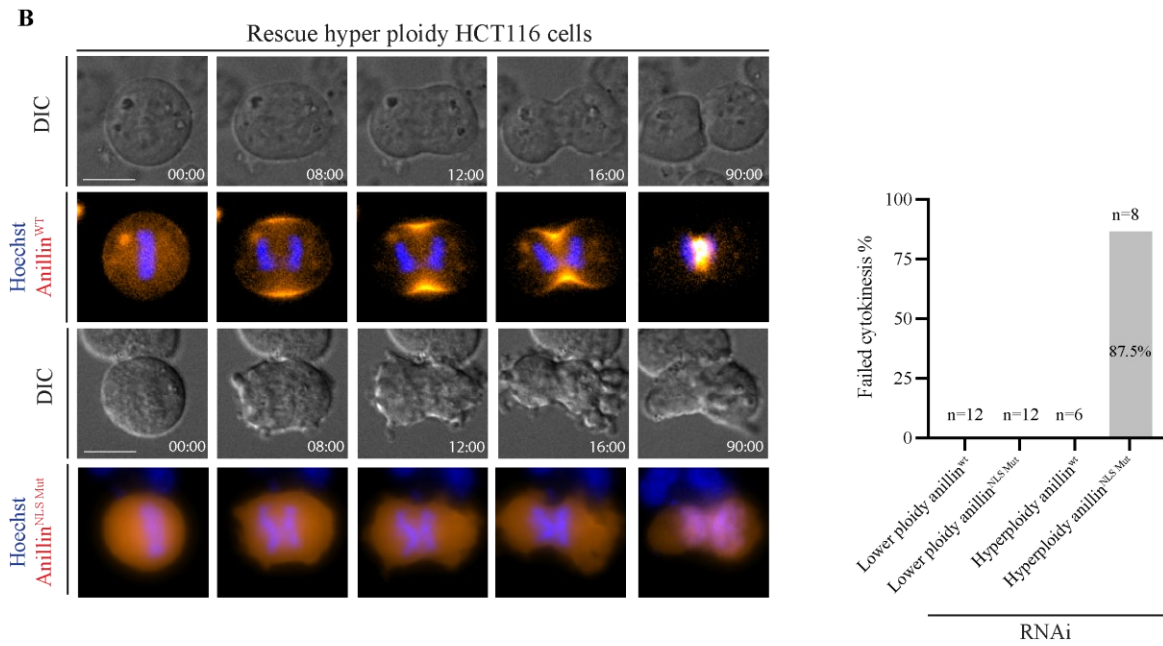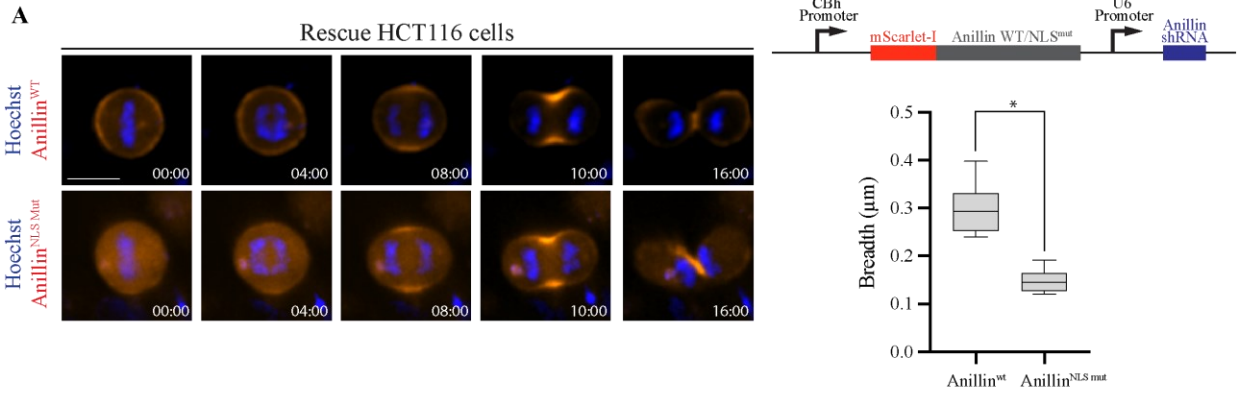stronic vector used for the rescue assays, which has a pCBh promoter driving the expression of an mScarlet-I-RNAi-resistant anillin fusion (red; wt or NLS mutant), and a U6 promoter driving the expression of anillin-specific shRNAs (blue). A box and whiskers plot shows the breadth of anillin (in µm) in HCT116 (mNeonGreen; p53-/-) cells rescued with wt or NLS mutant (n=10 for each). Bars show standard deviation (* $p<0.0001$). B) DIC and fluorescence timelapse images show hyperploidy HCT116 (mNeonGreen; p53-/-) cells co-expressing RNAi-resistant wt (top) or NLS mutant anillin (bottom; orange) with anillin shRNAs and stained with Hoechst (chromatin, magenta). Times are shown in minutes and the scale bar is 10 µm. To the right, a bar graph shows the percentage of cells that failed cytokinesis in lower and hyperploidy cells rescued with wt or NLS mutant as indicated. Sample sizes are indicated on the graph. C) A cartoon schematic of dividing cells depicts our model of how ploidy could cause a switch in the mechanisms controlling cytokinesis. In cells with lower ploidy (bottom), importins are more uniform and recruit anillin prior to anaphase, causing them to rely on other pathways to define the equatorial plane. In cells with higher ploidy (top), importins only reach a critical threshold to recruit anillin in the equatorial plane, and become a major mechanism for ring assembly and positioning.

(NLS mut) localization was different in both near diploid and hyperploid cells; it failed to localize cortically in metaphase, and was more restricted at the equatorial cortex and/or barely visible compared to control cells. We found that as with endogenous anillin, mScarlet-I-tagged wt anillin was enriched at the cortex prior to anaphase, while the NLSmut was cytosolic (Fig. 13A). We also measured the breadth of wt and NLSmut anillin in near diploid HCT116 cells (we did not measure the cells with higher ploidy as the cortical signal was too weak). Indeed, while the breadth of wt anillin was 29.9%, it was only 14.7% for the NLS mutant (Fig. 13A). To determine if importin-binding is also required for cytokinesis, we imaged HCT116 cells with lower or higher ploidy after rescue with wt or NLSmut anillin. As expected, there was no cytokinesis failure in HCT116 cells rescued with wt or NLSmut anillin, or in HCT116 cells with higher ploidy rescued with wt anillin (Fig. 13B). However, the majority of HCT116 cells with higher ploidy that were rescued with NLSmut anillin failed cytokinesis (87.5%; Fig. 13B). These results show that cells with higher ploidy rely more strongly on the chromatin pathway and the importin-regulation of anillin compared to cells with lower ploidy.

2.6 Discussion

Our study shows that the mechanisms controlling cytokinesis change with ploidy. Cytokinesis must occur with high precision, or it can lead to pathologies. Thus, multiple pathways are known to robustly control this process. These pathways include spindle and spindle-independent mechanisms that result in the equatorial accumulation of active RhoA and the generation of a contractile ring that is positioned between the segregating chromosomes[69,71]. The relative requirement for different pathways is predicted to change with parameters including ploidy, but few studies have investigated this. First, we found that anillin is more strongly required in HeLa and A549 cells, which are hypotriploid, compared to HCT116 and HFF1 cells, which are near diploid (Fig. 8). We then compared the threshold requirements for anillin in individual HeLa and HCT116 cells where anillin is endogenously tagged with mNeonGreen (Fig. 9). We found that HeLa cells require significantly more anillin to support cytokinesis compared to HCT116 cells. Further, we also found that anillin is required for midbody formation and stability in HCT116 cells, while it is required for ring positioning in HeLa cells (Fig. 9). Since the cell lines have different genetic backgrounds and tissues of origins, we induced an increase in ploidy in HCT116 cells to determine if anillin requirement changes with ploidy. To do this, we used CRISPR-Cas9 editing

to generate cells lacking functional p53, and induced aneuploidy using $CoCl_2$ treatment to induce oxidative stress (Fig. 10). Indeed, increasing ploidy caused HCT116 cells to have stronger requirements for anillin, with ring closure kinetics and anillin localization patterns similar to HeLa cells (Figs 11, 12). Finally, we found that anillin requires importin-binding for cytokinesis in HCT116 cells with higher ploidy, but not in cells with lower ploidy (Fig. 13). Thus, our data supports a model where in cells with higher ploidy, anillin's regulation by importin-binding plays a stronger role in ring positioning, as importins are predicted to be enriched between the segregating chromosomes compared to cells with lower ploidy where they are more uniformly distributed (Fig. 13C).

It is not clear why HCT116 cells tolerate more anillin loss compared to HeLa cells or HCT116 cells with higher ploidy. If importins are globally enriched in metaphase HCT116 cells, this would explain why anillin is already cortical prior to anaphase. The cells would then rely on spindle-dependent or kinetochore-dependent pathways to define the division plane in anaphase[110,143]. Cells relying on spindle-dependent pathways to control the equatorial accumulation of active RhoA for ring assembly and ingression may not require as much anillin to position the ring and/or may rely on other partially redundant mechanisms. Anillin and other ring components are broadly localized in HCT116 cells and rapidly assemble into rings that ingress faster compared to HeLa cells or HCT116 cells with higher ploidy (Fig. 12)[80]. It is not clear why these rings are more efficient, which could be due to a combination of cortical flow, actin crosslinkers and/or shedding of micromembrane domains[79,80,119,122,144]. This improved efficiency could make rings less reliant on anillin. Alternatively, ERM proteins could play a stronger role in the clearance of actin at the polar cortex to define the division plane, since their regulation is independent of anillin[98,145]. ERM proteins accumulate in the cleavage furrow, and may help support ingression in HeLa cells, but it is not clear how they are influenced by ploidy, or if they control cytokinesis in other human cell types[129].

An important factor to consider for the interpretation of our findings is that cell size scales with ploidy. We previously generated tetraploid cells in the early *C. elegans* embryo to compare cytokinesis in these cells with diploid cells[79]. The AB daughter fated to be somatic tissue is larger than the P1 daughter, which is fated to be germline. We found that tetraploid cells increased in size by ~1.5-fold, and the tetraploid P1 daughter was the same size as the diploid AB daughter[79]. Interestingly, cytokinesis kinetics were similar between the two cells, supporting a correlation with

size[79]. Thus, our model considers the impact of increasing ploidy on the chromatin to cytosolic ratio; as ploidy increases, size also increases, but not proportionally. In addition, a prior study showed that different cancer cell types with high aneuploidy also have more Ran-GTP with steeper gradients caused by increased RCC1 activity[132]. Presumably this would reduce the levels of cortical importins that are free to bind to NLS proteins, which would only increase after chromosomes move apart in anaphase to create a zone of depleted Ran-GTP.

A caveat to our study is that we increased ploidy using $CoCl_2$ treatment, which causes aneuploidy due to oxidative stress[133]. In addition to gene expression changes that could be caused by this treatment, presumably random chromosomes are gained (or lost) that could also affect gene expression. Our analyses always included control cells that had been treated with $CoCl_2$ and we grouped cells from different treatments to account for this genetic variability.

It was interesting to see that anillin is required for midbody formation and stability in HCT116 cells. Anillin is required for both ring positioning and to form a stable midbody in Drosophila S2 cells, and each of these functions is controlled through independent complexes[105,106,121]. The N-terminus of anillin plays a stronger role in midbody stabilization through its interactions with proteins including Sticky (citron kinase), among other proteins, that can crosslink to the microtubules of the intercellular bridge (ICB)[105,106,121]. We speculate that anillin could play a similar role in human cells, in addition to an even later function in stabilizing the midbody for abscission. Co-localization studies suggest that CHMP4B and the abscission machinery is recruited to the midbody only after anillin dissipates[125]. While there is evidence from other studies to support this hypothesis, since they primarily used HeLa cells where the loss of anillin causes earlier phenotypes, it has been challenging to directly show a role for anillin in midbody stabilization.[71] For example, anillin is required to organize septins for elongation of the intercellular bridge[124,125]. In addition, citron kinase was shown to regulate abscission in HeLa cells via RhoA and anillin through a mechanism that is not clear, and over-expression of anillin caused abscission delays[109]. Thus, this is the first time, to our knowledge, that loss of anillin has been shown to cause midbody phenotypes in HCT116 cells, and this could be an ideal cell type to explore the mechanism by which human anillin controls the later stages of cytokinesis.

We found that cells with higher ploidy require more anillin for cytokinesis. Anillin is one of the most significantly upregulated proteins in a plethora of cancers and is used as a tool for both diagnosis and prognosis[67]. Our findings could reveal the biological significance of this

upregulation. As cancer cells gain ploidy, they rely more heavily on anillin to position the ring between the masses of segregating chromosomes to avoid catastrophe. Cancer cells work on the 'edge' of catastrophe and undergo physiological adaptations to help them survive. Since anillin relies on importin-binding for its cortical accumulation, their own chromosomal gains now act as a dominant mechanism to control cytokinesis.

Chapter 3. Design, structure-activity relationship study and biological evaluation of the thieno[3,2-c]isoquinoline scaffold as a potential anti-cancer agent

Adapted from: Jiang Tian Liu, Dilan B. Jaunky, Kevin Larocque, Fei Chen, Keegan Mckibbon, Mehdi Sirouspour, Sarah Taylor, Alexandre Shafeii, Donald Campbell, Helena Braga, Alisa Piekny, Pat Forgione. (2021). Design, structure-activity relationship study and biological evaluation of the thieno[3,2-c]isoquinoline scaffold as a potential anti-cancer agent. *Bioorg med chem lett*. (52), 15.

3.1 Preamble

Dr. Forgione's (Chemistry and Biochemistry) laboratory synthesized compounds with a thienoisoquinoline scaffold, as they hypothesized that they could probe biological space (e.g., domains in proteins, nucleic acids) and have properties that could be ideal for *in vivo* use. To determine if these compounds affect cells, they initiated a collaboration with our lab. We found that one of these derivatives, 16g, caused HeLa cells to arrest in mitosis in the nanomolar range. Encouraged by this finding, we more rigorously tested 16g, as well as additional derivatives generated for structure-activity-relationship studies to compare their efficacy (IC$_{50}$). This chapter shows how 16g could be considered a lead compound compared to other derivatives. We show that 16g has higher toxicity in cancer cells, and shrinks multi-cellular tumour spheroids *in vitro*. We also found that 16g binds to tubulin *in vitro* and prevents microtubule polymerization. For this thesis, the synthetic pathways and structure-activity-relationship studies were omitted.

3.2 Abstract

Several derivatives of a series that share a thienoisoquinoline scaffold have demonstrated potent activity against cancer cell lines A549, HeLa, HCT-116, and MDA-MB-231 in the submicromolar concentration range. Structure- activity relationship (SAR) studies on a range of derivatives aided in identifying key pharmacophores in the lead compound. A series of compounds have been identified as the most promising with submicromolar IC$_{50}$ values against a lung cancer cell line (A549). Microscopy studies of cancer cells treated with the lead compound revealed that it causes mitotic arrest and disrupts microtubules. Further evaluation via an *in vitro* microtubule

polymerization assay and competition studies indicate that the lead compound binds to tubulin via the colchicine site.

3.3 Introduction

Cancer continues to pose a dramatic health risk and is one of the leading causes of death worldwide. Of the treatments that are currently available, chemotherapy is the most affordable option for patients globally. Various aspects of the cell cycle machinery are targeted by some of the most successful anti-cancer drugs[2,36]. While not selective for any cell type per se, these drugs have high efficacy in rapidly proliferating cells and act more effectively on cancer cells relative to healthy cells[2]. In particular, the mitotic spindle is particularly sensitive to disruption in cancer cells. The spindle begins to assemble in prometaphase, and forms stable attachments with the kinetochores of sister chromatids for their alignment at the metaphase plate[18]. Once this alignment occurs, the spindle assembly checkpoint is satisfied, and cells will exit mitosis[12]. Microtubules need to be highly dynamic to form stable kinetochore attachments, and microtubule-targeting drugs disrupt dynamics causing mitotic arrest, or catastrophe. Several microtubule regulators are differently expressed in cancers, making them more sensitive to microtubule disruption compared to their healthy cell counterparts[146].

There are several classes of microtubule-targeting agents (MTAs) that are grouped based on whether they stabilize microtubules by preventing depolymerization, or destabilize microtubules and/or prevent polymerization. Microtubules are made of protofilaments of α- and β-tubulin heterodimers that roll into a microtubule polymer with directionality – the β-subunit faces the plus/growing end of the microtubule, while the α-subunit faces the minus end[19]. When the β-subunit is GTP-bound, it typically promotes growth, while GTP hydrolysis will cause catastrophe due to changes in conformation that are kinetically unfavorable[20]. Microtubule-targeting agents that stabilize microtubules will prevent growth, and include taxanes (e.g., paclitaxel). Paclitaxel (or derivatives) is a naturally-derived compound that is among one of the most commonly used anti-cancer drugs, but has poor solubility requiring high doses and conjugation to protein or nanoparticles to overcome this limitation[41,42]. Paclitaxel can cause severe side-effects, and cancers can develop resistance, leaving patients with few treatment options[44,48,147]. Other microtubule-targeting agents destabilize microtubules and include colchicine, nocodazole and vinca alkaloids. While colchicine and nocodazole bind to the same site, the vinca site is distinct. Colchicine has a

narrow window of selectivity and is no longer used in cancer therapy, but is used to treat gout among other diseases[50]. Nocodazole is not used *in vivo* because of serious side-effects[58]. However, several compounds from the vinca family are used as anti-cancer therapies including vincristine and vinblastine, among others[148]. Thus, microtubule-targeting agents have proven efficacy in the clinic, but there is a need to expand the repertoire of synthetic compounds that can be designed to be more selective for cancer cells.

Here, we perform SAR with a thienoisoquinoline scaffold, by generating multiple derivatives, and testing their anti-cancer potential. We show that the addition of a 5' bromo group as well as a p-methoxy substitute to the D ring confers high potency. These findings suggest that 16g is a lead compound. We characterized 16g, and found that it reduces viability of A549 cells by causing mitotic phenotypes. We further reveal that 16g can reduce multi-cellular tumour spheroids *in vitro*. Lastly, we explore the mechanism of action of 16g by showing that it binds to tubulin *in vitro,* competes with colchicine, and prevents microtubule polymerization. These findings show that 16g has anti-cancer properties by disrupting mitotic spindles and justifies further exploration and characterization of this compound.

3.4 Materials and Methods

Viability assays

HFF-1 cells were grown in DMEM (Wisent), while A549 cells were grown in F12K media (Wisent) in humidified incubators at 37°C with 5% CO_2. The media was supplemented with 10% fetal bovine serum (FBS; Thermo Scientific), 2 mM L-glutamine (Wisent), 100 U penicillin (Wisent), and 0.1 mg/mL streptomycin (Wisent).

Compounds were dissolved in DMSO and stored at -20°C as 1 mM stocks. Working stocks of 100 μM were made in DMSO:H_2O (9:1). A549 cells were plated at 20-30% confluency in 96-well dishes and left overnight to adhere. Drug dilutions were prepared and added to the cells using the Acoustic Liquid Handler: LabCyte ECHO 550. After 3 population doubling times (33 – 36 hours for HFF-1, and 24 hours for A549), cells were assessed for viability using the WST-8 cell proliferation assay kit (Cayman Chemicals). Absorbance readings at 450 nm were collected using the TECAN 200 PRO plate reader. Values for each replicate were adjusted to the controls and

plotted using GraphPad Prism 7 to generate graphs and IC_{50} values. All assays were performed in triplicate for each treatment.

A549 spheroids were grown using the hanging drop method. Drops of media containing 50-100 cells were added to the surface of a lid from a 2 cm cell-culture petri dish. PBS was added to the bottom of the dish to prevent the drops from drying. The lid was then flipped and placed over the bottom of the dish to form hanging drops over the PBS. Dishes were incubated as described above for 3 days. Spheroids were transferred in media to wells of a 24-well dish after growing to an appropriate size and appearance as monitored by light microscopy. Treatments were performed as described above. To measure the change in area of the spheroids, image files were exported as TIFFs and analyzed using a macro written for Image J (FIJI; NIH). Images containing a spheroid were passed through "IsoData" thresholding and 10 iterations of the "close" function to fill in pixel size gaps. Spheroids were identified using the "analysis of particles" command in Image J and the area was measured by the software. For spheroids where the integrity was disrupted, the macro was modified to calculate the area. First images were converted to a black background and masked. Then, the "max inscribed circle" function was used to fit a perfect circle to the remaining spheroid structure. The function gives a radius from which the area was calculated.

Microscopy

A549 cells were imaged at 24-hour intervals after adding various concentrations of 16g using the Nikon-TiE inverted microscope with the 20x objective, a Piezo Z stage (ASI), a Photometrics Evolve 512 EMCCD camera and Elements acquisition software (Nikon) with DIC (differential interference contrast). Images were exported as TIFFs and converted into 8-bit images using ImageJ (NIH) and imported into Illustrator (Adobe) to make figures.

A549 cells were fixed for imaging microtubules. For fixation, cells were plated on coverslips at a confluency of 40-50% and left overnight to adhere. Cells were fixed using freshly prepared ice-cold 10% w/v cold trichloroacetic acid (TCA) for 14 minutes at 4°C. Cells were washed with phosphate buffered saline (PBST (0.3% Triton X-100) and kept at 4°C prior to staining. After blocking, fixed cells were immunostained for microtubules using 1:400 mouse anti-α-tubulin antibodies (DM1A; Sigma) and centromeres using 1:500 human anti-centromere antibodies (ACA; Sigma) for 2 hours at room temperature. After washing, anti-mouse Alexa 488

and anti-human Alexa 647 (Invitrogen) secondary antibodies were used at a 1:500 dilutions for 2 hours at room temperature. After washing, 4′,6-Diamidino-2′-phenylindole dihydrochloride (DAPI; Sigma) was added for 5 minutes. Cells were then washed with PBST, followed by a wash with 0.1 M Tris pH 9, then a drop of mounting media (0.5% propyl gallate in 50% glycerol) was added to the coverslip, which was mounted onto a slide and sealed. Fixed slides were imaged using the Nikon-TiE inverted microscope with Lambda XL LED light sources, using the 60x/1.4 oil objective, a Piezo Z stage (ASI), a Photometrics Evolve 512 EMCCD camera and Elements acquisition software (Nikon). Exposures were kept constant based on controls. Images were acquired as 1 μm Z-stacks and exported as TIFFs. Merged colour images were converted into 8-bit images using ImageJ (NIH) and imported into Illustrator (Adobe) to make figures.

Images of spheroids were collected each day at the same time using a Nikon-TiE inverted microscope with the 4x/0.2 (HeLa) or 10x/0.45 (A549 and HCT116) objectives using the DS-Ri2 ultra high-resolution colour camera (Nikon) and Elements acquisition software (Nikon). HCT116 spheroids treated with paclitaxel, 16g or both in combination were imaged using the 4x/0.2 objective and the 1.5 magnification changer. Files were opened in Image J for analysis as described below.

Microtubule polymerization assay

A 10 mg/mL flash frozen purified tubulin stock (Cytoskeleton, Inc) was thawed on ice and 1.5 mg/mL was diluted in G-PEM buffer (80 mM PIPES pH 6.9, 2 mM MgCl$_2$, 0.5 mM EGTA with 1 mM GTP) in 20% glycerol with 10% DMSO (control), 0.6 or 5 μM of colchicine (Bioshop) or 16g. Assays were performed in a preheated 50 μL sub micro Z15 black Q/Spectrosil cuvette in a Varian Cary 1 spectrophotometer. Reagents were added to the cuvette and blanked immediately before recording absorbance at 340 nm in 0.1 second intervals for 45 minutes. Light scattering at 340 nm is caused by the turbidity associated with the polymerized microtubules. Between trial runs, the cuvette was washed with HPLC grade methanol and rinsed thoroughly three times with PEM buffer.

Colchicine competition assay

Colchicine-bound tubulin causes a distinct excitation/emission spectra that is not observed for colchicine or tubulin on their own. This is proposed to be due to the tropolone (cyclic ketone)

and A-ring of the colchicine in the binding pocket, and can be used as an assay to measure binding efficacy[149]. To determine if 16g binds to the colchicine-site on tubulin, assays were performed with 100 ug/mL tubulin (porcine; Cytoskeleton, Inc) in 25 mM PIPES buffer, pH 6.8 in a 400 μL Q fluorometer cell, Z=20 (Varian) using a fluorescence spectrophotometer Cary Eclipse (Varian) at 25 °C for 1 hour. Nocodazole (Sigma), vinblastine (Bioshop) or 16g were used at a final concentration of 1 μM and added together with 2 μM colchicine (Bioshop). Reaction mixtures were excited at 350 nm and the emission spectra were recorded from 380 to 500 nm (Bhattacharyya and Wolff, 1974). Emission values were normalized to the spectra recorded at time zero. All values were exported as excel files and graphs were generated in Prism V8.1.0 Graphpad.
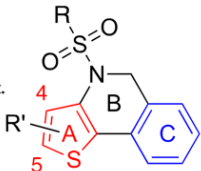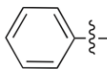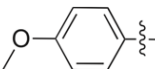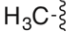
3.5 Results
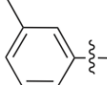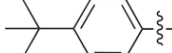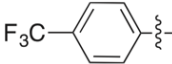
A series of derivatives with a hydrogen at the 5-position of the thiophene A-ring (15a-h) were treated with NBS to yield the corresponding brominated compounds (16a-16g). The brominated lead compound 16a showed a two-fold increase in potency to 1.9 μM compared to 15a. Similar to the trend observed in Table 1 (15a) a methyl substitution on the phenyl D-ring resulted in improved potency. The para-substituted methyl derivative 16c showed increased efficacy from 3.4 to 2.1 μM, and the meta-substituted derivative 16d showed about a 3-fold increase, from 6.0 to 2.3 μM. These modifications resulted in improvements relative to the non-brominated counterparts (Table 1, 15a and 15e). Adding an α-bromo to the thiophene of inactive D group methyl-substituted derivative 15b (Table 1) to produce 16b (Table 2) failed to restore activity (IC$_{50}$ > 10 μM). This was also observed for the brominated bulky para-t-butyl phenyl derivative 16e, and the electron withdrawing p-CF3 derivative 16f (Table 2). Encouragingly, bromination of the para-methoxy substituted 15g generated the most active derivative of the series, 16g. The IC$_{50}$ of this derivative improved by two-fold from 0.78 μM (15g) to 0.37 M (16g; Table 2). These results indicate that bromination at the α-position of the thiophene moiety enhances the activity of previously active compounds (16a,c,d,g), but does not confer activity on previously inactive compounds (16b,e,f). Nevertheless, this substitution can also be identified as a key pharmacophore, given the improved efficacy.

This result motivated us to evaluate additional substituents on the thiophene A-ring. A substituted 5-chloro derivative 17 had similar potency as the brominated counterpart (16g) with an

Table 1: Initial screening of D-ring substituents for thienoisoquinoline scaffolds.

SAR mapping for thiophene A-ring substituent.

Compd.	R	R'	A549 IC$_{50}$ (μM)	Comparative toxicity[a]	Compd.	R	R'	A549 IC$_{50}$ (μM)	Comparative toxicity[a]
16a		5-Br	1.9	118.7	16g		5-Br	0.37	23.1
16b			>10	>625	17		5-Cl	0.43	36.8
16c			2.1	131.2	18		5-I	0.78	48.7
16d			2.3	143.7	15i		4-CH$_3$	0.63	39.3
16e			>10	>625	19		4-CH$_3$, 5-Cl	0.55	34.3
16f			>10	>625	20		4-CH$_3$, 5-Br	2.8	175
					Colchicine			0.016	–

[a] Comparative toxicity: Thienoisoquinoline IC$_{50}$ against A549 / Colchicine IC$_{50}$ against A549

Table 2: SAR mapping for the thiophene A-ring substituent.

Initial screening of D-ring substituents for thienoisoquinoline scaffolds.
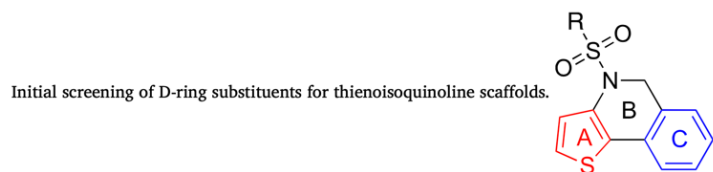
Compd.	R	A549 IC$_{50}$ (μM)[a]	Compd.	R	A549 IC$_{50}$ (μM)[a]
15a		5.2	15e	H$_3$C-	6.0
15b		>10	15f		>10
15c		>10	15g		>10
15d	F$_3$C-	3.4	15h		0.78
			Colchicine		0.016

[a] IC$_{50}$ are determined against lung cancer cell A549.

IC$_{50}$ of 0.43 μM, while the 5-iodo substituted derivative 18 had a 2-fold decreased potency compared to 16g (Table 2). We also synthesized the 4-methyl substituted derivative 15i to evaluate substitution at the 4-position of the thiophene A-ring that interestingly had an IC$_{50}$ of 0.63 μM, which was similar to the unsubstituted derivative 15h (Table 1). Adding a chloro group to the 5-position of the 4-methyl thiophene derivative (19) improved potency to 0.55 μM, and the 5-bromo substitution (20) lowered the potency four-fold to 2.8 μM (Table 2). Overall, the most drug like molecule synthesized was the 5-bromo derivative 16g (Table 2) with a p-methoxy substituted D-ring, which had an IC$_{50}$ of 0.37 M. The identification of two key pharmacophores is promising for the synthesis of future analogues.

The effect of 16g in cells was explored. As shown in Fig. 14, A549 cells treated with derivative 16g died within 2–3 days. By 24 h, the majority of cells had rounded up, indicative of mitotic arrest. Spindle defects typically lead to unattached sister chromatids, which triggers cell cycle arrest by the spindle assembly checkpoint[146]. To determine if 16g causes spindle defects, A549 cells were fixed and stained for chromatin with DAPI (blue), tubulin to visualize microtubules (green) and ACA to stain centromeres (site of kinetochore attachments; red) after 8 h of treatment with 0.30 or 0.50 μM of derivative 16g. Mitotic cells had reduced or aberrant mitotic spindles, with misaligned chromosomes and fragmented spindle poles at higher concentrations of derivative 16g (top panel; Fig. 15), and no obvious phenotypes during interphase (bottom panel; Fig. 15). To determine if 16g retains efficacy on A549 cells grown in 3D cultures, A549 cells were induced to form intact, stable multicellular tumor spheroids *in vitro* (Fig. 16). Spheroids mimic small tumors, with an outer proliferative ring, and quiescent middle zone of cells that are not dividing due to limited resources[150,151]. A549 spheroids treated with 0.50 or 1.0 μM of 16g showed disrupted morphology compared to control spheroids treated with DMSO (Fig. 16). Measurements of the change around the core revealed that the spheroids reduced in size in response to 16g (Fig. 16). These results show that 16g retains its efficacy when cells are grown in more complex environments. Overall, these experiments suggest that 16g causes mitotic arrest and eventual cell death, however, additional experiments are required to explore this further.

Other compounds that cause mitotic arrest affect microtubule polymerization, leading to mitotic spindle phenotypes. To determine if derivative 16g causes spindle phenotypes by targeting tubulin, a microtubule polymerization assay was performed in the presence of 16g or colchicine,
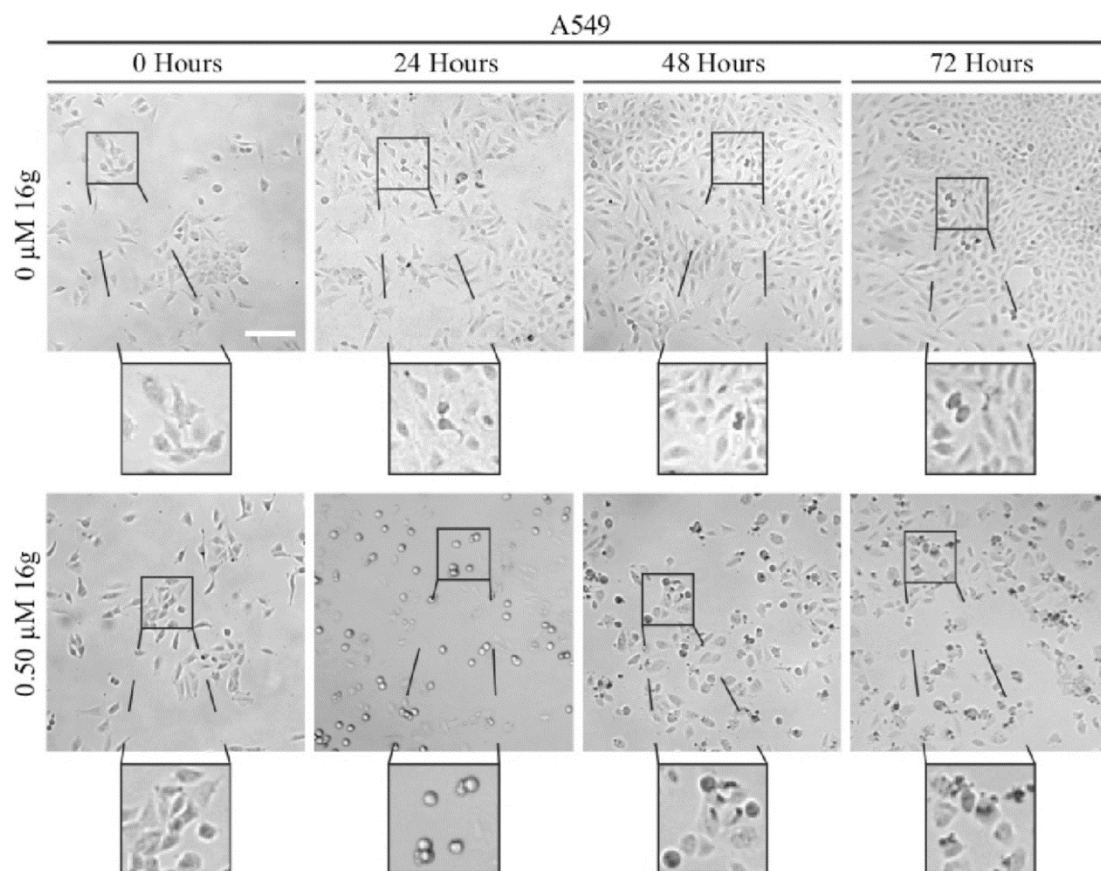
Figure 14: 16g prevents A549 cancer cell division and causes death. Brightfield images show A549 cells with or without treatment of 0.5 μM 16g. Images were taken every 24 hrs. Zoomed-in fields of view show healthy (top) and dying (bottom) cells. The scale bar is 50 μm.
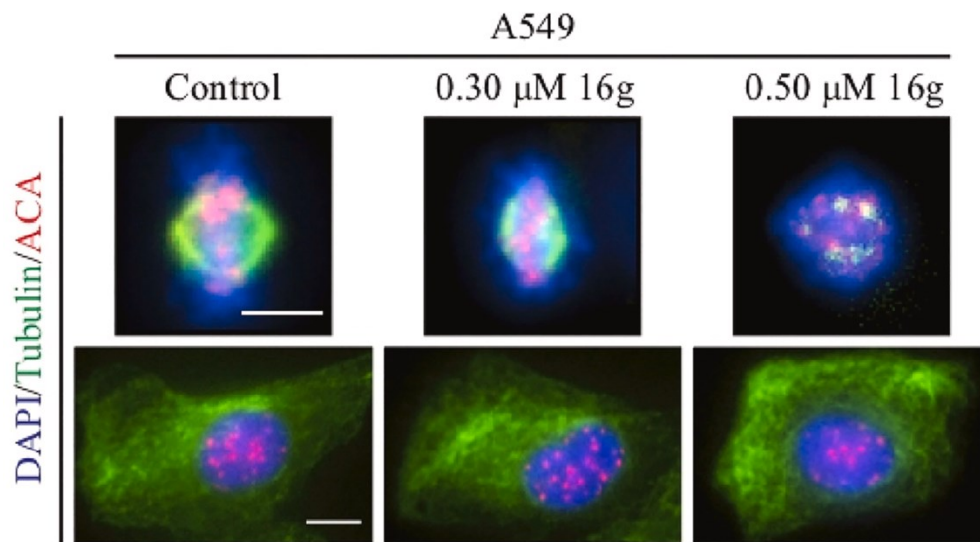
Figure 15: **16g causes mitotic phenotypes**. Immunofluorescent images at the top show control or treated A549 cells in mitosis as indicated. Metaphase cells were co-stained to reveal DNA (blue; DAPI), microtubules (green) and kinetochores (red; ACA). Interphase cells are shown with the same staining underneath. The scale bar is 10 μm.
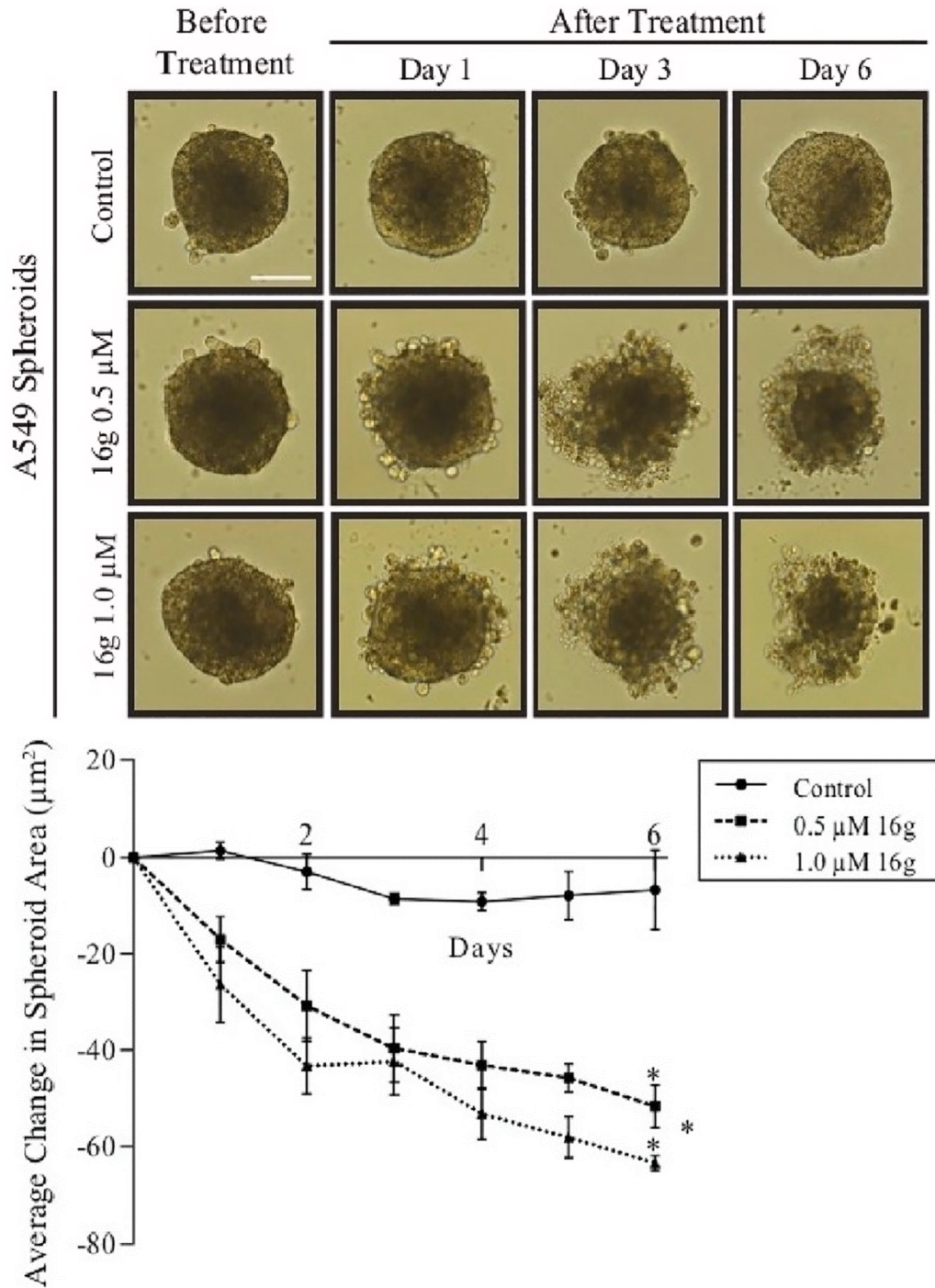
Figure 16: **16g causes multi-cellular tumour spheroids to shrink**. At the top, brightfield color images show A549 multi-cellular tumour spheroids with or without treatment of 0.5 μM and 1.0 μM 16g. Images were taken before the addition of the drug, and after every 24 hrs. The scale bar is 100 μm. Underneath, a line graph shows the average change in spheroid size (area) over time (days). The lines show standard deviation, and the asterisks indicate $p<0.05$.

a known tubulin-targeting compound that depolymerizes microtubules[152]. When at sufficiently high concentrations, and in the presence of Mg^{2+} and GTP, tubulin polymerizes into microtubules *in vitro*[153]. Microtubules polymerized in the presence of 0.6 μM, but not with 5 μM of colchicine (Fig. 17). Derivative 16g partially or fully blocked microtubule polymerization at concentrations of 0.6 or 5 µM, respectively (Fig. 17). This data shows that derivative 16g directly prevents microtubule polymerization. To determine if derivative 16g binds to the same site as colchicine, a competition assay was performed *in vitro*. Multiple tubulin-targeting compounds similarly block polymerization, but act via different binding sites[59]. Colchicine, which was used for the discovery of tubulin, binds to a well-characterized site in the tubulin heterodimer and causes a distinct excitation/emission spectra compared to tubulin or colchicine on their own (Fig. 18)[154,155]. As previously reported, adding 1 μM of nocodazole reduced the spectra caused by colchicine, demonstrating competition[156] (Fig. 18). Adding 1 μM of derivative 16g similarly reduced the spectra, while 1 μM of vinblastine did not (Fig. 18). Therefore, these findings demonstrate that derivative 16g could directly or allosterically compete with colchicine for binding. Knowledge of this location as a possible binding site for 16g would allow for docking studies and the generation of new derivatives with improved selectivity toward cancer cells.
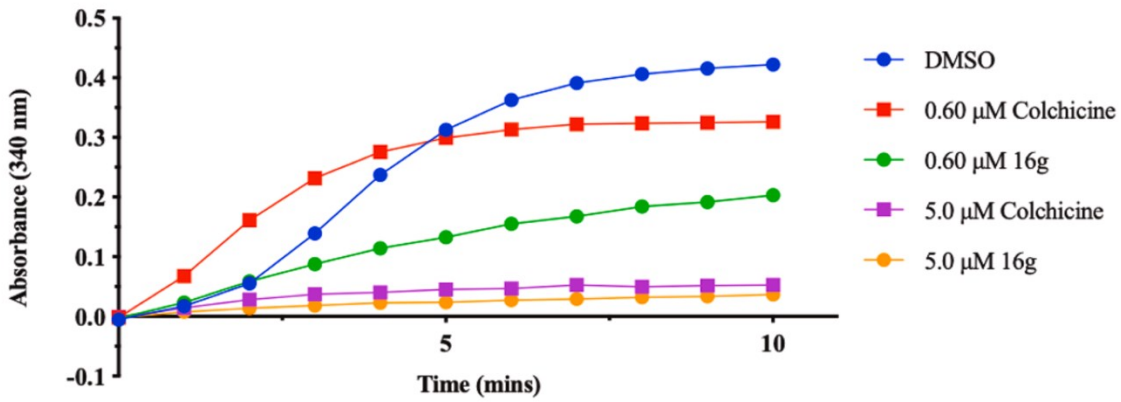
Figure 17: Microtubule polymerization *in vitro* is inhibited by 16g. The line graph shows the change in microtubule absorbance at 340 nm over time (minutes). The colors refer to the different treatments as indicated (blue, DMSO; red, 0.6 μM colchicine; green, 0.6 μM 16g; purple, 5 μM colchicine; orange 5 μM 16g).
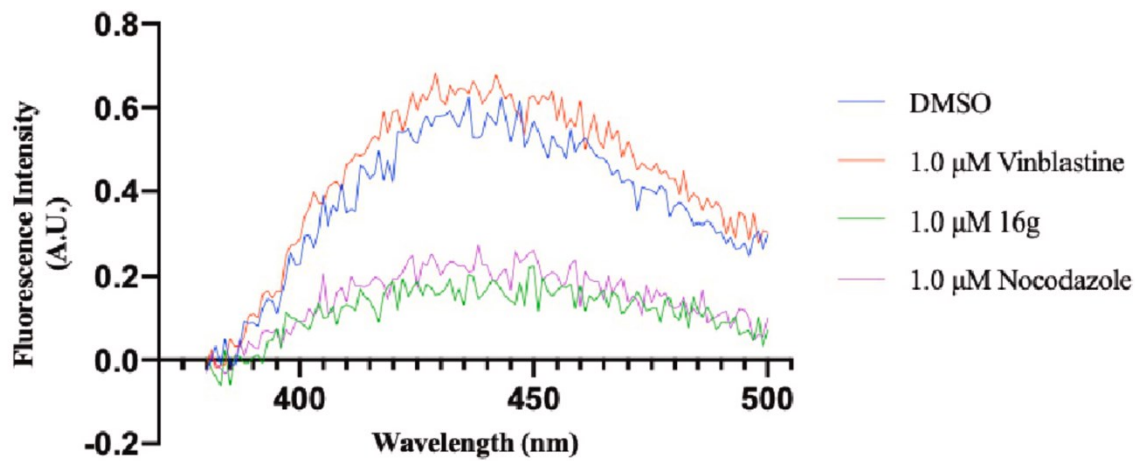
Figure 18:. **Colchicine-binding is competed by 16g**. A graph shows the fluorescence intensity (a.u.) over different wavelengths (nm) for colchicine-bound tubulin (blue, DMSO), or after co-incubation with 1 μM vinblastine (orange), 16g (green) or nocodazole (purple).

3.6 Discussion

A new series of thienoisoquinoline derivatives were generated and tested for their activity in A549 cells, a human lung cancer cell line. Dr. Forgione's group modified both the A-ring and the D-ring on the thienoisoquinoline scaffold with a variety of chemical moieties and we tested their efficacy through IC_{50} experiments (Table 1). These studies revealed a lead compound 16g with an IC_{50} of 0.37 μM, demonstrating its potential cytotoxicity to cancer cells (Table 2). A bromo substituent on the A-ring in combination with electron-donating groups on the D-ring are important structural features required to confer the highest activity against cancer cells. Further, comparison of 16g efficacy among several cell types revealed 3.5-fold selectivity for cancer cell types compared to normal fibroblasts. Future efforts will focus on further improvements based on these key structural features, and modifications of the core heterocyclic ring system to improve toxicity and selectivity.

We also obtained data demonstrating the effect of 16g in cells. We found that 0.5 μM 16g causes A549 cells to arrest mitosis and die after several days of treatment. We also found that 16g caused A549 multi-cellular tumour spheroids to shrink, suggesting that the compound can affect cells within 3D environments (Fig. 16). Multi-cellular spheroids better predict dug efficacy compared to monolayers because they mimic some aspects of the tumour microenvironment and organization[150,151]. For example, spheroids typically have a rim of proliferating cells, with a quiescent zone and necrotic core[150,151]. These results suggest that 16g has anti-cancer properties.

We found that the molecular target of 16g is tubulin. 16g effectively competes with colchicine for the same binding site and more effectively prevents microtubule polymerization *in vitro* (Fig. 18). Knowledge of the target will help drive future SAR studies to find derivatives with improved efficacy. Microtubule-targeting agents have had high success in the clinic, but as mentioned earlier, nocodazole is too toxic and colchicine has too narrow of a window to be used therapeutically for cancers and instead is used to treat gout. It will be important to compare 16g with the mechanism of action of these other compounds to determine if it has the potential to be used *in vivo*.

Chapter 4. Characterization of a recently synthesized microtubule targeting compound that disrupts mitotic spindle poles in human cells

4.1 Preamble

Chapter 4 provides an in-depth characterization of 16g (hereafter referred to as C75) in cells to determine the mechanism of action more precisely, and to compare it to other microtubule-targeting agents. Here, we show how C75 causes the formation of multipolar spindles in a way that is unique compared to other microtubule-targeting drugs. We also show that it synergizes with colchicine and paclitaxel, suggesting that its mechanism of action in cells is distinct.

4.2 Abstract

We reveal the effects of a new microtubule-destabilizing compound in human cells. C75 has a core thienoisoquinoline scaffold with several functional groups amenable to modification. Previously we found that sub micromolar concentrations of C75 caused cytotoxicity. We also found that C75 inhibited microtubule polymerization and competed with colchicine for tubulin-binding *in vitro*. However, here we found that the two compounds synergized suggesting differences in their mechanism of action. Indeed, live imaging revealed that C75 causes different spindle phenotypes compared to colchicine. Spindles remained bipolar and collapsed after colchicine treatment, while C75 caused bipolar spindles to become multipolar. Importantly, microtubules rapidly disappeared after C75-treatment, but then grew back unevenly and from multiple poles. The C75 spindle phenotype is reminiscent of phenotypes caused by depletion of ch-TOG, a microtubule polymerase, suggesting that C75 blocks microtubule polymerization in metaphase cells. C75 also caused an increase in the number of spindle poles in paclitaxel-treated cells, and combining low amounts of C75 and paclitaxel caused greater regression of multicellular tumour spheroids compared to each compound on their own. These findings warrant further exploration of C75's anti-cancer potential.

4.3 Introduction

Dynamic microtubules are required to form mitotic spindles, and drugs that suppress these dynamics are used to treat cancer[146,157]. At the G2/M transition, there is an increase in microtubule growth from the maturing centrosomes. Dimers of α-tubulin and β-tubulin form 13 protofilaments that roll into a tubule, which are templated by the γ-tubulin ring complex[158,159]. GTP-bound dimers at the plus end promote microtubule growth, while the loss of this cap favors catastrophe[20,21,158]. During catastrophe the protofilaments adopt a curved state and bend away from the lumen[51,160]. Microtubule dynamics are required to form stable kinetochore attachments, and many microtubule associated proteins (MAPs) influence these dynamics by stabilizing minus or plus ends[19]. MAPs include enzymes such as CKAP5/ch-TOG and MCAK that control polymerization and depolymerization, respectively, for bipolar spindle assembly[21,27,35,161–165]. Microtubule-targeting drugs that suppress microtubule dynamics and prevent the formation of stable kinetochore attachments can lead to cell cycle arrest or catastrophe, and cell death.

Several microtubule-targeting drugs are currently being used to treat cancers. Uncontrolled cell proliferation is a hallmark of cancer, which makes cancer cells more sensitive to drugs that disrupt the cell cycle compared to healthy cells[1,166]. Taxol™ is a microtubule-targeting compound that is used to treat several cancers[38]. Taxol binds to microtubules and stabilizes the lattice to prevent depolymerization[40,167]. These reduced dynamics disrupt the formation of stable kinetochore attachments triggering the spindle assembly checkpoint to cause cell cycle arrest or mitotic catastrophe[43]. Although Taxol has been successful in the clinic, it causes side-effects and some patients develop resistance[44]. Thus, there is a need to find alternative drugs that can reduce the amount of Taxol needed for treatment, reducing side-effects and resistance.

Other microtubule-targeting compounds destabilize microtubules. These altered dynamics also cause mitotic arrest or catastrophe and have been used or considered for use as anti-cancer therapies. One of these compounds is colchicine, which binds to a deep pocket on β-tubulin and prevents growth or causes catastrophe at the plus end and has a low off-rate[55,57,168]. Colchicine is used to treat gout, but failed as an anti-cancer therapy[50,169]. Another compound is vinblastine, which is used as an anti-cancer drug[51,170]. It binds to the interface of the heterodimer and introduces a molecular wedge causing the protofilaments to adopt a curled conformation that destabilizes the microtubule[50,51]. Vinblastine has fewer side-effects compared to colchicine. In addition to having

64

distinct binding sites, they have different properties *in vivo*, including accessibility to the minus vs. plus ends and how they affect microtubule polymers[51]. *In vitro*, vinblastine favours depolymerization at the minus ends and suppresses dynamics at the plus ends[171]. In HeLa cells, low concentrations (e.g. 2 nM) do not cause changes in the microtubule polymer mass, but block mitosis by decreasing kinetochore attachments, and causing the dissociation of mother and daughter centrioles[172,173].

Cancer cells often accumulate mutations that alter the expression or function of MAPs, which can increase their sensitivity to microtubule-targeting drugs[146,174]. Coupling MCAK depletion with low concentrations of Taxol or vinblastine in cancer cells increases mitotic spindle phenotypes and causes apoptosis[175]. Aurora A kinase, which regulates centrosome maturation and plus-ends for kinetochore attachments, and ch-TOG (CKAP5), a microtubule polymerase, are over-expressed in colorectal cancer cells[27,28,154,155,176–179]. Their overexpression correlates with increased rates of microtubule assembly and chromosomal instability (CIN) due to an excess of lagging chromosomes[28,176]. These properties could make mitotic spindles sensitive to further disruption by microtubule targeting drugs compared to healthy cells.

We recently synthesized a novel family of theionoisoquinoline compounds that target microtubules. We strategically designed the compounds to have properties ideal for *in vivo* use and screened derivatives for their ability to block cancer cell proliferation. The compounds share a core scaffold amenable to modifications[156]. We identified several derivatives that caused toxicity and mitotic arrest with IC_{50} values in the sub micromolar range[180]. Some derivatives had no or little effect on cells (e.g. C87, $IC_{50} > 10$ μM) while others, such as C75, had high efficacy (e.g. IC_{50} between 0.1 and 0.4 μM) depending on the cell type[180]. We also found that C75 prevented microtubule polymerization and competed with colchicine for tubulin-binding *in vitro*[180].

Here, we characterized the phenotypes caused by C75 to elucidate its mechanism of action in cells. While longer treatments of C75 or colchicine caused similar mitotic spindle phenotypes, the two compounds synergistically increased cytotoxicity, supporting differences in how they affect microtubules in cells. Indeed, colchicine and C75 caused different spindle phenotypes. When added in metaphase, spindles remained bipolar and eventually collapsed after colchicine treatment, while C75 caused bipolar spindles to become disorganized and/or multipolar. C75 phenocopies ch-TOG depletion suggesting that it blocks microtubule polymerization in cells. In addition, C75

caused an increase in the number of spindle poles in cells where microtubules were stabilized by paclitaxel. Excitingly, combining low doses of C75 and paclitaxel caused greater regression of multicellular tumour spheroids compared to each compound on their own, warranting further exploration of C75 as an anti-cancer drug.

4.4 Materials and Methods

Cell culture and drug treatments

HeLa and HFF-1 cells obtained from the American Type Culture Collection (ATCC) were grown in DMEM (Wisent), while A549 cells were grown in F12K media (Wisent) and HCT116 (p53-/-) cells were grown in McCoy's media (Wisent) in humidified incubators at 37 °C with 5% CO_2. All media were supplemented with 10% fetal bovine serum (FBS; Thermo Scientific), 2 mM l-glutamine (Wisent), 100 U penicillin (Wisent), and 0.1 mg/mL streptomycin (Wisent).

C87 and C75 were stored at −20°C as 1 mM stocks in dimethyl sulfoxide (DMSO). Working stocks of 100 μM C75 or C87 were made in DMSO:H2O (9:1). Colchicine (Sigma) was dissolved in ethanol as a 1 M stock and diluted to 10 μM before use. Nocodazole was dissolved in DMSO as a 1 mg/mL stock (Sigma). Paclitaxel (Bioshop) was dissolved in DMSO as a 10 mM stock and diluted to a range of smaller concentrations before use. Cells grown as monolayer cultures or as spheroids were treated with C75, C87, colchicine, or paclitaxel as indicated, and the final concentrations of DMSO or ethanol were kept below 0.5%.

Tubulin binding assays

Tubulin binding was assessed using a fluorescence quenching assay[58]. This assay was performed with 1.5 μM of purified tubulin taken from a flash frozen 10 mg/mL stock (Cytoskeleton Inc.) thawed on ice and diluted in 600 μL of 25 mM PIPES pH 6.9. Tubulin was placed in a Q fluorometer cell, Z = 20 (Varian), and incubated with DMSO, or 5 μM of C87, C75 or nocodazole at 25 °C for 20 min. Measurements were taken using a fluorescence spectrophotometer Cary Eclipse (Varian). The sample was excited at 295 nm and the fluorescence intensity was measured over a range of emission spectra from 300 to 500 nm. Scans were repeated 10 times through computer averaging of transients (CAT) application which averages each individual scan. All

values were exported as excel files and graphs were generated in GraphPad Prism v.9.2.0. The experiment was replicated three times.

Viability assays

Assays were performed to determine the viability of cells after treatment with C75 and/ or colchicine. The concentration of colchicine or C75 used in the combination experiments was the highest concentration that caused little to no toxicity based on dose–response curves. HFF-1, HeLa, A549 and HCT116 cells were plated with 4,000 cells/well in 96-well dishes and left overnight to adhere. Drug dilutions were prepared and added to the cells using an acoustic liquid handler (LabCyte ECHO 550). After 3 population doubling times, cells were assessed for viability using the WST-8 cell proliferation assay kit (Cayman Chemicals). Absorbance readings at 450 nm were collected using the TECAN 200 PRO plate reader. Values for each replicate were adjusted to the controls and plotted using GraphPad Prism v.9.2.0 to generate graphs and IC$_{50}$ values. All assays were performed in triplicate for each treatment. For the combination assays, C75 or colchicine were repeated alongside the combination treatments to ensure accurate comparison.

Flow cytometry

Flow cytometry was used to measure changes in the proportion of cells in different stages of the cell cycle after C75-treatment. HeLa, HCT116 and A549 cells were grown to 80% confluency and treated with a range of C75 concentrations for 8 h. Cells were harvested in falcon tubes, then fixed with 70% cold ethanol and washed with cold phosphate buffered saline (PBS; Wisent). Cells were permeabilized and stained for 15 min at 37 °C with a solution containing 500 μg/mL PI (Sigma) in PBS with 0.1% (v/v) Triton X-100 and DNAse-free RNAse A (Sigma). Cells were protected from light and measured for PI intensity using the BD LSR Fortessa flow cytometer with excitation at 561 nm and detection at 600 nm (LP) using the D-BP filter. Each treatment was done in triplicate with 20,000 cells per sample analyzed using FCS 7 Cytometry (https://denovosoftware.com/). Data was exported and plotted using GraphPad Prism v.9.2.0 to make bar graphs.

Immunofluorescence staining

Immunofluorescence was performed to monitor mitotic spindle phenotypes. Cultured cells were plated on coverslips at a confluency of 40–50% and left overnight to adhere. Cells were fixed

using freshly prepared ice-cold 10% w/v cold trichloroacetic acid (TCA) for 14 min at 4 °C. Cells were washed with PBST (0.3% Triton X-100) and kept at 4 °C prior to staining. After blocking, fixed cells were immunostained for microtubules using 1:400 mouse anti-α-tubulin antibodies (DM1A; Sigma) or centrosomes using 1:400 mouse anti-γ-tubulin antibodies (Santa Cruz Biotechnology) or mouse anti-Centrin 2 (clone 20H5; Sigma), and centromeres using 1:500 human anti-centromere antibodies (ACA; Sigma) for 2 h at room temperature. After washing, anti-mouse Alexa 488 and anti-human Alexa 647 (Invitrogen) secondary antibodies were used at a 1:500 dilutions for 2 h at room temperature. After washing, 4′,6-Diamidino-2′-phenylindole dihydrochloride (DAPI; Sigma) was added for 5 min. Cells were then washed with PBST, followed by a wash with 0.1 M Tris pH 9, then a drop of mounting media (0.5% propyl gallate in 50% glycerol) was added to the coverslip, which was mounted onto a slide and sealed.

Microscopy

Fixed slides were imaged using the Nikon-TIE inverted epifluorescence microscope with Lambda XL LED light sources, using the 60x/1.4 oil objective, a Piezo Z stage (ASI), a Photometrics Evolve 512 EMCCD camera and NIS Elements (Nikon). Exposures were determined by control cells, and the same settings were used in the treatment conditions. Images were acquired as 1 μm Z-stacks and exported as TIFFs, which were opened as maximum intensity Z-stack projections in ImageJ v.2.0.0 (NIH;https://imagej.nih.gov/ij/index.html). Merged colour images were converted into 8-bit images and imported into Adobe Illustrator v.25 to make figures.

For live imaging, HeLa cells were plated to 50–60% confluency on 25 mm round coverslips (No. 1.5; Neuvitro). Cells were treated with 75 nM Hoescht 33,342 and 200 nM SiR-tubulin (Cytoskeleton Inc.) for 90 min prior to imaging. Depending on the experiment, HeLa cells were transfected with a plasmid that expresses RNAi-resistant ch-TOG:GFP plus a hairpin RNA (sh ch-TOG) to knockdown endogenous protein and minimize overexpression (Addgene ID# 69,113). HeLa cells stably expressing GFP:tubulin and mCherry:tubulin were previously generated[82]. Coverslips were transferred to a 35 mm chamlide magnetic chamber (Quorum) and kept at 37 °C with 5% CO_2 using an INU-TiZ-F1 chamber (MadCityLabs). Images were acquired at 1 or 5-min intervals using the 60x/1.4 oil objective on the Nikon Livescan sweptfield confocal microscope with an Andor iXon X3 EMCCD camera and NIS Elements (Nikon). The 405 nm, 480 nm and 640 nm lasers were used to image Hoescht, GFP and sir-Tubulin, respectively, with a quad filter

and exposures set to controls. Z-stacks of 1 μm were collected using a NI-DAQ piezo Z stage (National Instruments). Images were used to make figures as described above.

HeLa cells that stably express GFP:tubulin or mCherry:tubulin were plated onto coverslips and treated with 50 nM colchicine or 300 nM C75 for 2 h and transferred to a 35 mm chamlide magnetic chamber (Quorum). The cells were transferred to 37 °C with 5% CO_2 using an INU-TiZ-F1 chamber (MadCityLabs) and random fields of view were chosen on the cover slip and imaged for > 4 h using 60x/1.4 oil objective on the Nikon Livescan sweptfield confocal microscope with an Andor iXon X3 EMCCD camera and NIS Elements (Nikon). The 480 nm laser was used to image GFP:tubulin with a quad filter and exposures set to controls. Z-stacks of 1 μm were collected using a NI-DAQ piezo Z stage (National Instruments). Images were used to make figures as described above.

To analyze the recovery of microtubules after cold-treatment in cells, HeLa cells were plated onto coverslips and transferred to a 35 mm chamlide magnetic chamber (Quorum), which was placed in an ice-cold water bath to cause spindle collapse. After 30 min, the cells were transferred to 37 °C with 5% C O2 using an INU-TiZ-F1 chamber (MadCityLabs) and C75 or colchicine was added after acquisition of the first timepoint. Images were acquired using the 60x/1.4 oil objective on the Nikon Livescan sweptfield confocal microscope with an Andor iXon X3 EMCCD camera and NIS Elements (Nikon). The 405 nm and 480 nm lasers were used to image Hoescht 33,342, GFP:tubulin respectively, with a quad filter and exposures set to controls. Z-stacks of 1 μm were collected using a NI-DAQ piezo Z stage (National Instruments). Images were used to make figures as described above.

Multicellular tumour spheroids

HCT116 spheroids were grown on agarose. In a 96-well dish, 1,000 HCT116 cells were added to wells coated with 1.5% agarose. After spheroids grew to an appropriate size and appearance (~ 5 days), they were transferred to agarose-coated wells in a 24-well dish in 1 mL of media. After the addition of DMSO, C75, paclitaxel or both C75 and paclitaxel in combination, images were collected every 24 h for 6 days using a Nikon-TIE inverted microscope with the 4x/0.2 objective and the 1.5 magnification changer using the DS-Ri2 ultra high-resolution colour camera (Nikon) and NIS Elements (Nikon).

Analysis

For the analysis of spindle phenotypes, 1 mm z-stack projections of individual cells were used. To calculate the proportion of mitotic cells in Fig. 19A, we counted the following number of rounded HeLa cells: 0 nM n = 568, 100 nM n = 847, 200 nM n = 266, 300 nM n = 105, 400 nM n = 96, 500 nM n = 75), A549 cells: 0 nM n = 461, 100 nM n = 519, 200 nM n = 181, 300 nM n = 154, 400 nM n = 150, 500 nM n = 253), and HCT116 cells: 0 nM n = 813, 100 nM n = 742, 200 nM n = 297, 300 nM n = 296, 400 nM n = 314, 500 nM n = 301 (N = 4 experimental replicates). To calculate the proportion of cells with different mitotic spindle phenotypes in Fig. 20B,C, the following number of HFF-1 cells were counted after treatment with DMSO n = 85, 300 nM C87 n = 99 and 300 nM C75 n = 84, HeLa cells after treatment with DMSO n = 152, 300 nM C87 n = 147 and 300 nM C75 n = 332, A549 cells with DMSO n = 87, 300 nM C87 n = 130 and 300 nM C75 n = 204, and HCT116 cells with DMSO n = 131, 300 nM C87 n = 128 and 300 nM C75 n = 245 (N = 3 experimental replicates). To determine the number of centrin-2-positive foci in HeLa cells (Fig. 20D), an average of 25 cells were counted for the control (DMSO treated) and 30 cells after treatment with 300 nM C75 (N = 3 experimental replicates). To calculate changes in the proportion of mitotic spindle phenotypes in HeLa cells after treatment with C75 and/or colchicine (Fig. 21B,C), we counted the following numbers of cells: DMSO n = 128, 20 nM colchicine n = 186, 50 nM colchicine n = 215, 100 nM colchicine n = 223, 100 nM C75 n = 127, 200 nM C75 n = 134, 300 nM C75 n = 370, 400 nM C75 n = 219, 500 nM C75 n = 200, 100 nM C75 + 20 nM colchicine n = 223, 200 nM C75 + 20 nM colchicine n = 273, 300 nM C75 + 20 nM colchicine n = 321, 400 nM C75 + 20 nM colchicine n = 303 and 500 nM C75 + 20 nM colchicine n = 277 (N = 3 experimental replicates). To count the proportion of cells with multipolar or bipolar spindles in HeLa cells after release from C75 or colchicine (Fig. 22B), we counted the following number of cells: DMSO n = 61, 500 nM C75 n = 50 and 500 nM colchicine n = 64 (N = 3 experimental replicates). For Fig. 24A, we counted 534 ch-TOG RNAi cells and 81 DMSO cells (N = 3 experimental replicates). To calculate changes in the proportion of mitotic spindle phenotypes in HCT116 cells after treatment with C75 and/or paclitaxel (Fig. 25A), we counted the following number of cells: DMSO n = 116, 2.5 nM paclitaxel n = 99, 10 nM paclitaxel n = 91, 50 nM paclitaxel n = 79, 100 nM paclitaxel n = 75, 100 nM C75 n = 52, 200 nM C75 n = 53, 2.5 nM paclitaxel + 100 nM C75 n = 112, 2.5 nM paclitaxel + 200 nM C75 n = 72 (N = 3 experimental replicates). To measure the distance between fragmented spindle poles in Fig. 25B, we counted

the following number of cells: 2.5 nM paclitaxel n = 21, 10 nM paclitaxel n = 21, 2.5 nM paclitaxel + 400 nM C75 n = 31, 2.5 nM paclitaxel + 400 nM C75 n = 22 (N = 3 experimental replicates).

To determine synergy for the viability of cells treated with C75 and colchicine in combination, CompuSyn (https://www.combosyn.com/index.html) was used (Figs. 21A, S4A). We used the non-constant ratio method of analysis since the concentration used for the combination studies was selected based on the highest concentration without lethality. The analysis indicated what combination of drug concentrations yielded an antagonistic, synergistic or additive effect based on the well-documented combination index (CI) described by the ChouTalalay method[181].

To determine the effect of C75 on spindle poles, images of HeLa cells stably expressing GFP:Tubulin and/or ch-TOG:GFP; sh ch-TOG were collected and used to measure changes in spindle volume and maximum intensity. To do this, z-stacks of images collected by sweptfield confocal microscopy were deconvolved using Autoquant and then reconstructed into 3D cells by rendering in Imaris v.9.7.2 (Bitplane). Thresholding was used to identify the spindle poles and render them as distinct objects using the spot analyzer function. The spherical objects were tracked and quantified over time for changes in their volume and intensity. The values were exported and organized in csv format using a macro in Python v.3.0 (https://www.python.org/download/releases/3.0/) to extract the volume and maximum intensity of each pole. The csv files were then imported into GraphPad Prism v.9.2.0 to build graphical representations, including heat maps, bar graphs and distribution plots. Statistical analyses were also done in GraphPad Prism v.9.2.0, to determine the significance between slope distributions using the Welch's two-tailed t test with a 99% confidence interval (p < 0.0001). Peaks corresponding to changes in spindle pole volume was determined for each pole using the built-in function "findpeaks" in MatLab R2017b (coding in Spyder v.4.0.1; https://www.spyder-ide.org). The parameters were set to identify any peaks that corresponded to a change in volume with an amplitude > = 20%. Identified peaks were then tabulated in Excel (Microsoft) and imported to GraphPad Prism v.9.2.0 for graphical representation.

The distances between spindle fragments in Fig. 25B were analyzed using a macro written for Image J v.2.0.0 (NIH; https://imagej.nih.gov/ij/index.html). Image files were exported as TIFFs and opened as Z-stack projections of maximum intensity and converted to a binary mask. Using

the ROI manager, each cell was first identified using DAPI, then the tubulin fragments were identified. Each fragment correlated with a point of maximum intensity, and the coordinates for that point were recorded. The distance between two points was measured using the coordinates of each point, and triangulating the distance based on Pythagorean theorem: A2 + B2 = C2, C being the distance between 2 given points.

To measure changes in spheroid area in Fig. 25C, images were exported as TIFFs and analyzed using a macro written for Image J v.2.0.0 (NIH; https://imagej.nih.gov/ij/index.html). Images were subjected to "IsoData" thresholding and 10 iterations of the "close" function to fill in pixel size gaps. Spheroids were identified using the "analysis of particles" command and the area was measured from the radius generated by the software.

4.5 Results

Compound 75 causes cells to arrest in G2/M phase

C75 is a new microtubule-targeting compound, and we wanted to characterize its mechanism of action in cultured human cells. The structure of C75 is shown in Fig. 19A along with C87, an inactive derivative. We previously found that C75 competes for colchicine binding to tubulin *in vitro*[180]. Since this competition could be indirect, we determined if C75 directly binds to tubulin. By monitoring changes in the emission spectra of tubulin, we found that C75 or nocodazole, another microtubule-depolymerizing compound, caused a similar decrease in emission compared to DMSO (control) or C87 (Fig. 19B). C75 was identified by structure–activity-relationship studies assaying for cytotoxic effects on A549 cells[180]. We found that C75 also caused toxicity in other cell types. The IC_{50} in HFF-1 (male foreskin fibroblast), HeLa (female cervical adenocarcinoma), A549 (male lung carcinoma), and HCT116 (male colorectal carcinoma) cells was 789, 427, 377 and 431 nM, respectively, while there was little/no toxicity for C87 (Fig. 19C). This data shows that C75 has ~ two fold higher sensitivity for some cell types compared to others. To determine if the reduced cell viability is due to cell cycle defects, we performed flow cytometry on HeLa, A549 and HCT116 cells after treatment with increasing concentrations of C75 for 8 h. There was a significant increase in the proportion of cells in G2/M with 400 or 500 nM C75 in all three cell lines with a corresponding decrease in G1 (Figs. 19D, S3A). We also observed significant changes in the proportion of cells in G2/M and G1 in HCT116 cells after treatment with

A

C75

C87

B

- Control Tubulin
- 5 uM C87
- 5 uM C75
- 5 uM Nocodazole

C
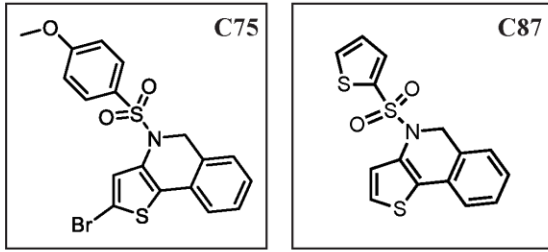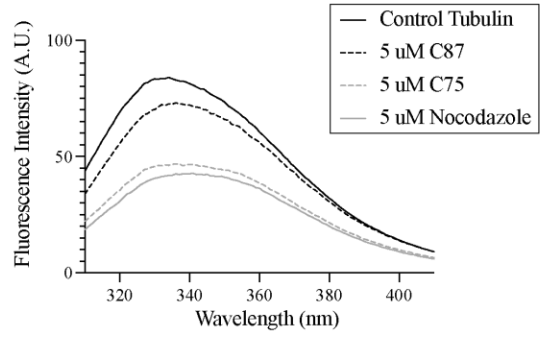
	Viability IC$_{50}$, nM	
Cell Lines	**C75**	**C87**
HFF-1	789	> 1000
HeLa	427	> 1000
A549	377	> 1000
HCT 116	431	> 1000

D

- G2/M
- S
- G0/G1
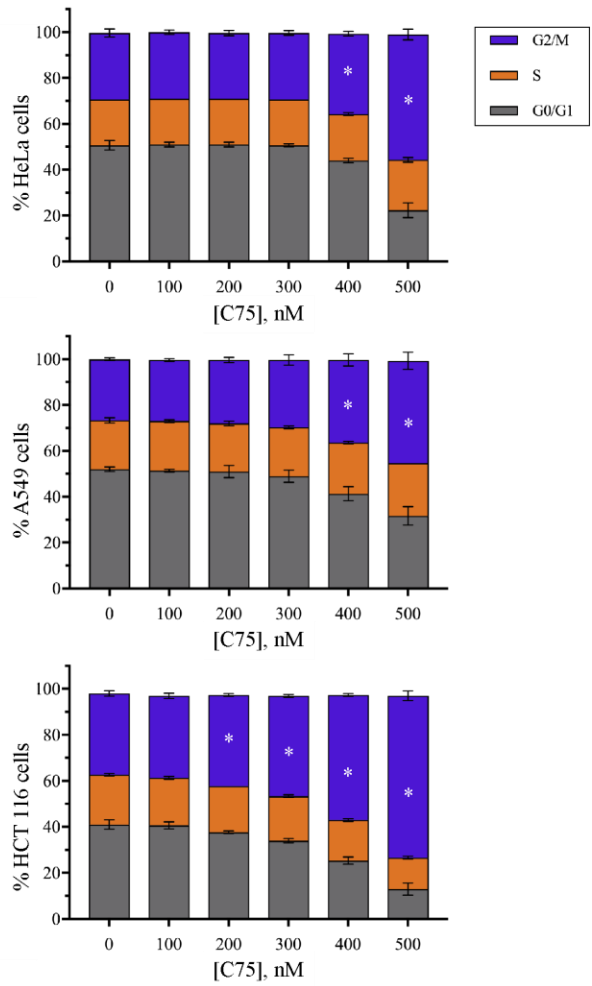
E
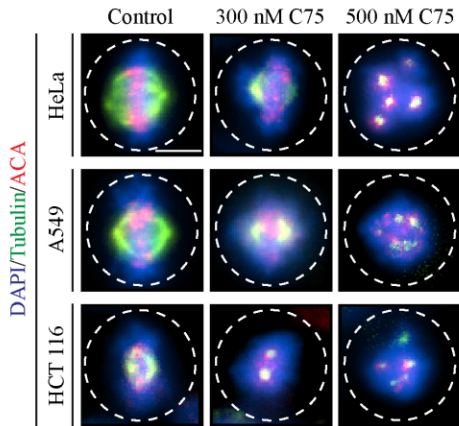
Figure 19: C75 is a thienoisoquinoline compound that causes G2/M arrest in cultured human cells.
(A) The structures of C75 and C87, a derivative with minimal activity, are shown. (B) A graph shows the absorbance of tubulin (control, grey line) measured by a change in fluorescence (y-axis), compared to when 5 μM of C87, C75 or nocodazole was added to tubulin for the wavelengths as shown on the x-axis. (C) A table shows the I C50 for the viability of HFF-1, HeLa, A549 and HCT116 over three population doubling times after treatment with C75 or C87 (N = 3). (D) Bar graphs show the distribution of cells in G0/G1, S and G2/M phases of the cell cycle measured by flow cytometry, for HeLa, A549 and HCT116 cells treated with increasing concentrations of C75 for 8 h (n = 20,000 cells per treatment; N = 3 experimental replicates). Asterisks indicate statistical significance using two-way ANOVA test and post-hoc Tukey's multiple comparison test with a 95% CI, multiplicity adjusted p = < 0.0004. (E) Images show fixed HeLa, A549 and HCT116 cells immunostained for DNA (DAPI; blue), tubulin (green), and centromeres (ACA; red) after treatment with 300 or 500 nM of C75 for 8 h. Dotted lines outline the cells. The scale bar is 10 μm.

200 and 300 nM C75 (Fig. 19D, S3A). In contrast, the proportion of HeLa and A549 cells in S phase remained the same and changed only in HCT116 cells after treatment with 500 nM C75 (Figs. 19D, S3A).

The increase in G2/M cells caused by C75 implies mitotic delays or arrest. To assess mitotic phenotypes, cells were fixed and stained for DNA, microtubules and centromeres after treatment with 300 or 500 nM C75. While control HeLa, A549 and HCT116 metaphase cells had bipolar spindles and aligned chromosomes, treated cells had spindles with reduced microtubule intensity, misaligned chromosomes and multiple spindle poles (Fig. 19E). We also measured the proportion of rounded, mitotic HeLa, A549 and HCT116 cells 24h after treatment with varying concentrations of C75 (Fig. 20A). We saw a dramatic increase in the proportion of mitotic cells at 300 nM (55.7% HeLa, 76.4% A549 and 71.7% HCT116, respectively). Therefore, increasing concentrations of C75 appear to cause mitotic arrest in different cell types. To determine the fate of C75-treated HeLa cells, we followed individual cells for ~ 17 h by live imaging. While control cells underwent mitosis as expected, C75-treated cells failed to exit mitosis and underwent apoptosis (Fig. S3B).

C75 causes spindle phenotypes

We propose that C75 arrests cells in mitosis by causing spindle defects. Since our previous experiments were done over long periods of time (e.g. 8–24 h), we quantified spindle phenotypes after treatment for less time to capture a broader range of phenotypes. HFF-1, HeLa, A549 and HCT116 cells were treated with 300 nM C75 for 4 h and stained for DNA, γ-tubulin and centromeres (Fig. 20B). While spindles in C75-treated HFF-1 cells were similar to control, HeLa, A549 and HCT116 cells had monopolar (centrosomes failed to separate), bipolar misaligned (misaligned sister chromatids) and multipolar spindles (Fig. 20B,C). HeLa cells had a significant increase in bipolar misaligned (41.1 vs. 7.1% control) and multipolar spindles (30.6 vs. 7.6% control), while A549 cells had an increase in monopolar (5 vs. 0% control) and multipolar spindles (77.6 vs. 3% control) and HCT116 cells had monopolar (34.5 vs. 9.5% control), bipolar misaligned (21.5 vs. 4.4% control) and multipolar spindles (12.5 vs. 6.9% control; Fig. 20C). The different proportions of spindle phenotypes caused by C75 in each cell line likely reflects differences in their genetic backgrounds.

To determine if other centrosome components localize to the poles of multipolar spindles,

A

B

HFF-1 | HeLa | A549 | HCT 116

DAPI / g-Tubulin / ACA

Control: 98% | 92% | 97% | 84% — Bipolar aligned

C75 300 nM: 96% | 41% | 17% | 22% — Bipolar misaligned

31% | 78% | 13% — Multipolar/Fragmented

35% — Monopolar

Centrosome
Tubulin
Chromosome
Centromere

C

D

DAPI/Tubulin/Centrin-2

Control | C75 300 nM

Monopolar
Bipolar misaligned
Bipolar aligned
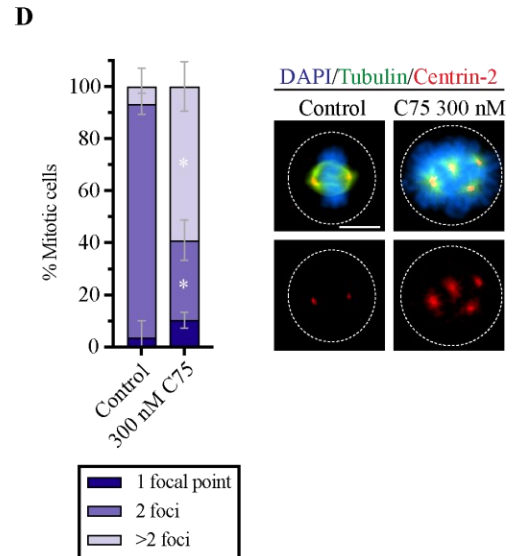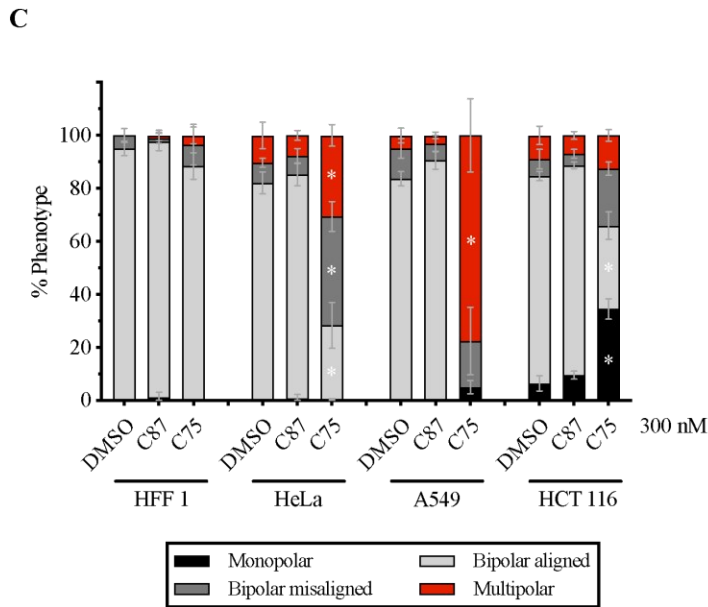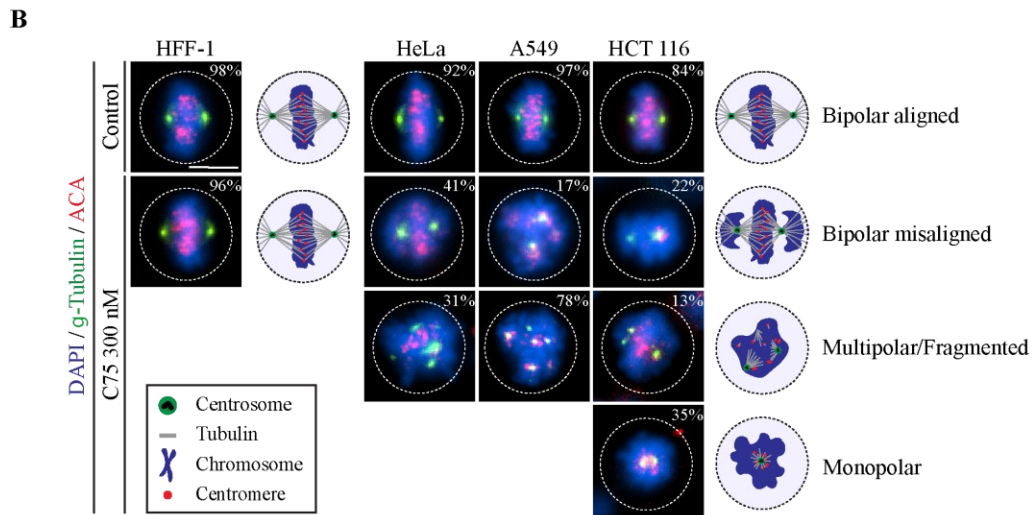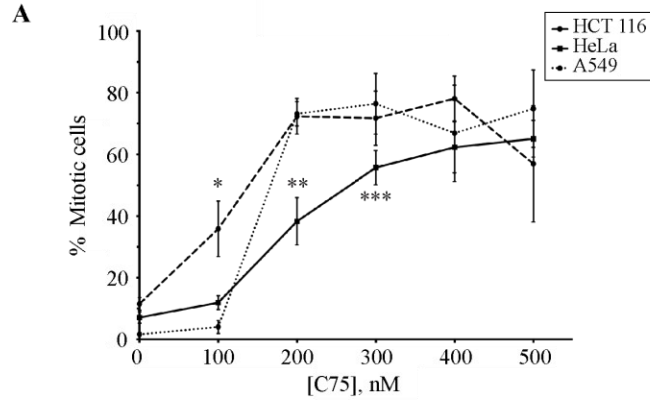Multipolar

1 focal point
2 foci
>2 foci

Figure 20: C75 causes the formation of multipolar spindles and mitotic arrest. (A) A line graph shows changes in the proportion of mitotic HeLa, A549 and HCT116 cells after treatment with increasing concentrations of C75 for 24 h. Asterisks indicate statistical significance using a two-way ANOVA test and post-hoc Tukey's multiple comparison test with a 99% CI; a single asterisk means that HCT116 is significantly different than HeLa and A549 (multiplicity adjusted $p = 0.0007$ and $p < 0.0001$, respectively), two indicates that HeLa is significantly different than A549 and HCT116 (multiplicity adjusted $p < 0.0001$ for both), and three indicates that HeLa is significantly different than A549 (multiplicity adjusted $p = 0.0035$). (B) Images show fixed HFF 1, HeLa, A549 and HCT116 cells stained for DNA (DAPI; blue), g-tubulin (green), and centromeres (ACA; red) after treatment with 300 nM of C75 for 4 h. Cartoon schematics (green circles, centrosomes; blue, chromatin; grey lines, microtubules; red, centromeres) show the different phenotypes observed, including bipolar spindles with aligned chromosomes (top), bipolar spindles with misaligned chromosomes (second from top), multipolar spindles (third from top), or monopolar spindles (bottom). The proportion of cells with each phenotype is shown in the top right corner of each image. The scale bar is 10 µm. (C) A bar graph shows the proportion of each spindle phenotype (bipolar aligned in light grey; bipolar misaligned in dark grey; multipolar in red; monopolar in black) for HFF 1, HeLa, A549 and HCT116 cells treated as in B). Bars show standard deviation and asterisks indicate two-way ANOVA test and a post-hoc Tukey's multiple comparison test with a 99% CI, and multiplicity adjusted $p < 0.001$ for each phenotype vs. DMSO and C87. (D) A bar graph shows the proportion of HeLa cells with 1 (dark purple), 2 (purple) or more (light purple) centrin-2 foci after treatment with DMSO or 300 nM C75. Cells were fixed and stained for DNA (DAPI; blue), tubulin (green), and centrin-2 (red). Asterisks indicate statistical significance of C75 with 2 foci and > 2 foci compared to DMSO using multiple t test with a 95% CI with a multiplicity adjusted $p = 0.0009$ and $p = 0.0031$, respectively. The scale bar is 10 µm.

we repeated this experiment using HeLa cells and stained for DNA, tubulin and centrin-2, which marks centrioles (Fig. 20D). Since individual centrioles were difficult to resolve by light microscopy, we quantified the number of foci and assumed that each contains a minimum of two centriole pairs. Indeed, a significantly greater proportion of C75-treated cells had more than 1 or 2 centrin-2 foci compared to control cells (59 vs. 10%). Therefore, both γ-tubulin and centrin-2 are localized to multipolar spindles in C75-treated cells.

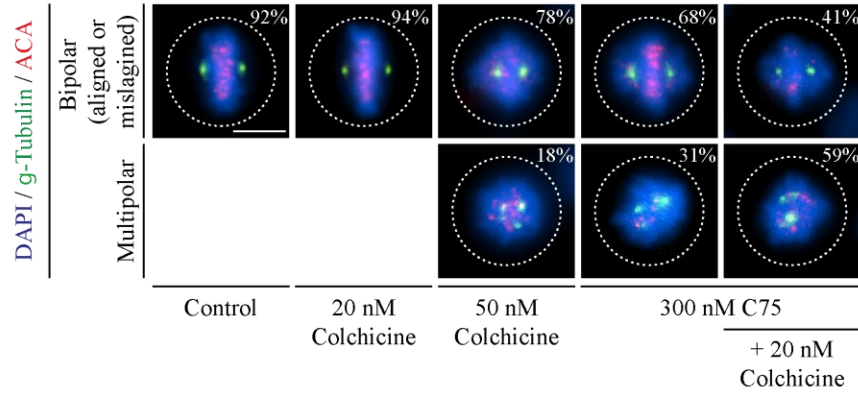**Combining C75 and colchicine increases spindle phenotypes**

Mitotic spindle phenotypes have been previously reported for colchicine[57]. Although C75 competed with colchicine for tubulin-binding *in vitro*, they could bind to different sites or have different accessibility to microtubules in cells. In this case, we expect to see additive or synergistic interactions, which we tested using toxicity assays and comparing the IC_{50} for each compound alone vs. adding them together. The IC_{50} for C75 and colchicine in HeLa cells was 425 and 9.5 nM, respectively (Fig. 21A). Adding 3 nM colchicine, a sub-optimal concentration that had little effect on viability, lowered the IC_{50} of C75 to 153 nM (Fig. 21A). Similarly, adding 250 nM of C75 to colchicine lowered its IC_{50} to 1.9 nM (Fig. 21A). To ascertain whether the combinatorial treatments were synergistic, additive or antagonistic, we analyzed the data with CompuSyn (https://www.combosyn.com/index.html)[181]. Using the non-constant ratio method, we determined the Combination Index (CI) for each drug combination and found synergies with 3 nM of colchicine and 300 nM of C75 (CI = 0.20), and when 250 nM C75 was combined with 5 nM colchicine (CI = 0.25; Fig. S4A).

Next, we measured changes in the spindle phenotypes caused by combining the two compounds. HeLa cells were treated for 4 h with 20 or 50 nM colchicine, and 100, 200 or 300 nM of C75 with or without 20 nM colchicine. Cells were fixed and stained for DNA, γ-tubulin and centromeres, and the proportion of cells with bipolar, bipolar misaligned or multipolar spindles was counted for each treatment (Fig. 21B,C). While cells treated with DMSO (control), 20 nM colchicine, 100 or 200 nM C75 had similar proportions of bipolar misaligned or multipolar spindles, higher concentrations of colchicine (50 nM) or C75 (300 nM) caused an increase in spindle phenotypes (Fig. 21B,C). Adding 20 nM of colchicine to 300 nM C75 caused a significant increase in the proportion of cells with multipolar spindles beyond the sum of each compound on
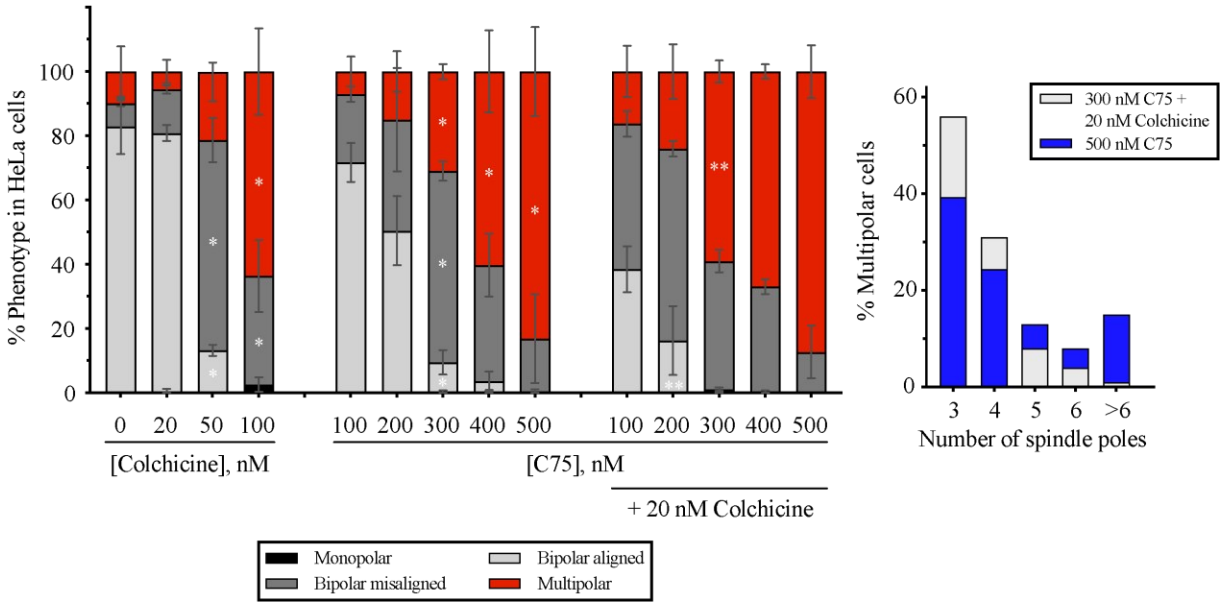
A
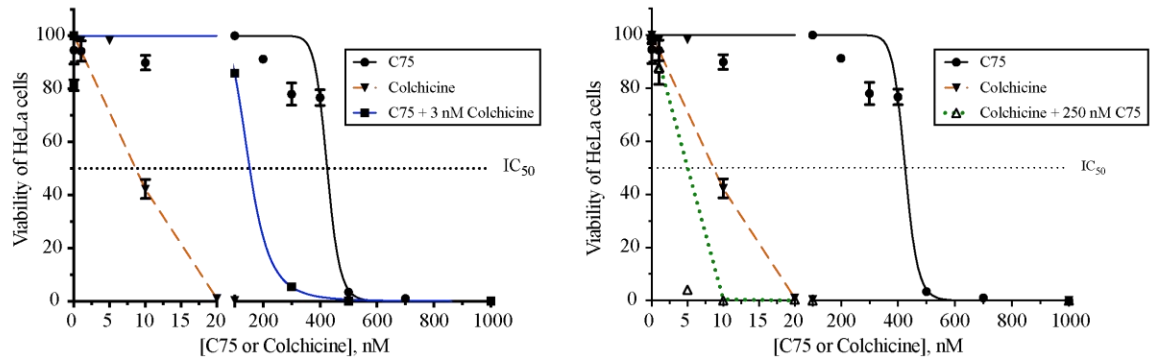
B

C

Figure 21: Combining C75 with colchicine enhances lethality and increases spindle phenotypes. (A) Line graphs show the IC_{50} for the viability (dotted black lines) of HeLa cells treated with varying concentrations of C75, colchicine, or both after three population doubling times as indicated. The graph on the left shows changes in viability (Y-axis) with increasing concentrations of C75 (X-axis; black line), colchicine (dotted orange line), and C75 with 3 nM colchicine (blue line). The graph on the right shows the changes in viability with colchicine and 250 nM C75 (green dotted line). The bars indicate SEM for N = 3 experimental replicates. (B) Images show fixed HeLa cells stained for DNA (DAPI; blue), g-tubulin (green) and ACA (centromeres; red) after treatment for 5 h with colchicine, C75 or both. The proportion of cells with bipolar spindles (aligned or misaligned chromosomes) and multipolar spindles are indicated on the images. The scale bar is 10 μm. (C) Bar graphs show the proportion of HeLa cells from B) with bipolar aligned (light grey), bipolar misaligned (dark grey), multipolar (red) or monopolar (black) spindles. Bars show standard deviation. Statistical analysis was done using two-way ANOVA test and a post-hoc Tukey's multiple comparison test with a 90% CI, and multiplicity adjusted $p < 0.0831$; a single asterisk indicates significance to the control (DMSO) and two indicates significance to C75. (D) A bar graph shows the percentage of multipolar HeLa cells from (C) with different numbers of spindle poles after treatment with 300 nM C75 plus 20 nM colchicine (light grey) or 500 nM C75 (blue).

their own at those concentrations (Fig. 21B,C). Therefore, C75 and colchicine enhance each other at sub-lethal concentrations. We also determined if combining C75 and colchicine causes more severe multipolar spindle phenotypes. While the number of spindle poles in multipolar cells was similar for cells treated with 300 nM C75, 50 nM colchicine or 300 nM C75 with 20 nM colchicine, cells treated with 500 nM of C75 had a greater proportion of cells with six or more poles (Fig. 21D, also Fig. S4B). This data suggests that colchicine and C75 have different effects on spindles.

C75 and colchicine have different effects on mitotic spindles in cells

Next, we compared the spindle phenotypes caused by C75 and colchicine. We performed live imaging to determine the effects of C75 and colchicine on mitotic spindles. HeLa cells were pre-treated with Hoechst 33342 and SiR-tubulin to visualize chromatin and microtubules, respectively. Cells with bipolar spindles and aligned chromosomes were treated with 50 nM or 300 nM colchicine, or 300 nM C75 and imaged for changes in spindle morphology. The majority of control cells (DMSO) had bipolar spindles that matured to segregate sister chromatids and form a midbody (14/15), while one cell had a tripolar spindle (Fig. 22A). The majority of cells treated with 50 nM colchicine had bipolar spindles that arrested (30/33), although a small proportion had multipolar spindles (3/33; Fig. 22A). Cells treated with 300 nM colchicine also had bipolar spindles that arrested (20/20), and 5/20 had extensive microtubule loss and collapsed spindles (Fig. 22A). Cells treated with 300 nM C75 showed a mix of phenotypes including arrested bipolar spindles with reduced microtubules (12/21), multipolar spindles (7/21) and a monopolar spindle (1/21; Fig. 22A). We were surprised to see that microtubules regrew in C75-treated cells, which was not observed in any of the colchicine-treated cells (Fig. 22A). Thus, C75 and colchicine cause different spindle phenotypes, with the caveat that few concentrations were tested.

Next, we compared how mitotic spindles recover after release from short-term treatments. HeLa cells were treated with 500 nM of C75 or colchicine for 5 min, then the drugs were washed out, and cells were left to recover for 40 min prior to fixing and staining them for DNA and tubulin (Fig. 22B). With this time frame, cells could have been in late G2 or early mitosis upon treatment. A larger proportion of C75-treated cells had multipolar spindles (49.7 vs. 45.7% bipolar) compared to those treated with colchicine (17.7 vs. 79.2% bipolar; Fig. 22B). The small, but significant increase in multipolar spindles after colchicine treatment suggests that multipolar spindles arise from effects caused prior to metaphase.
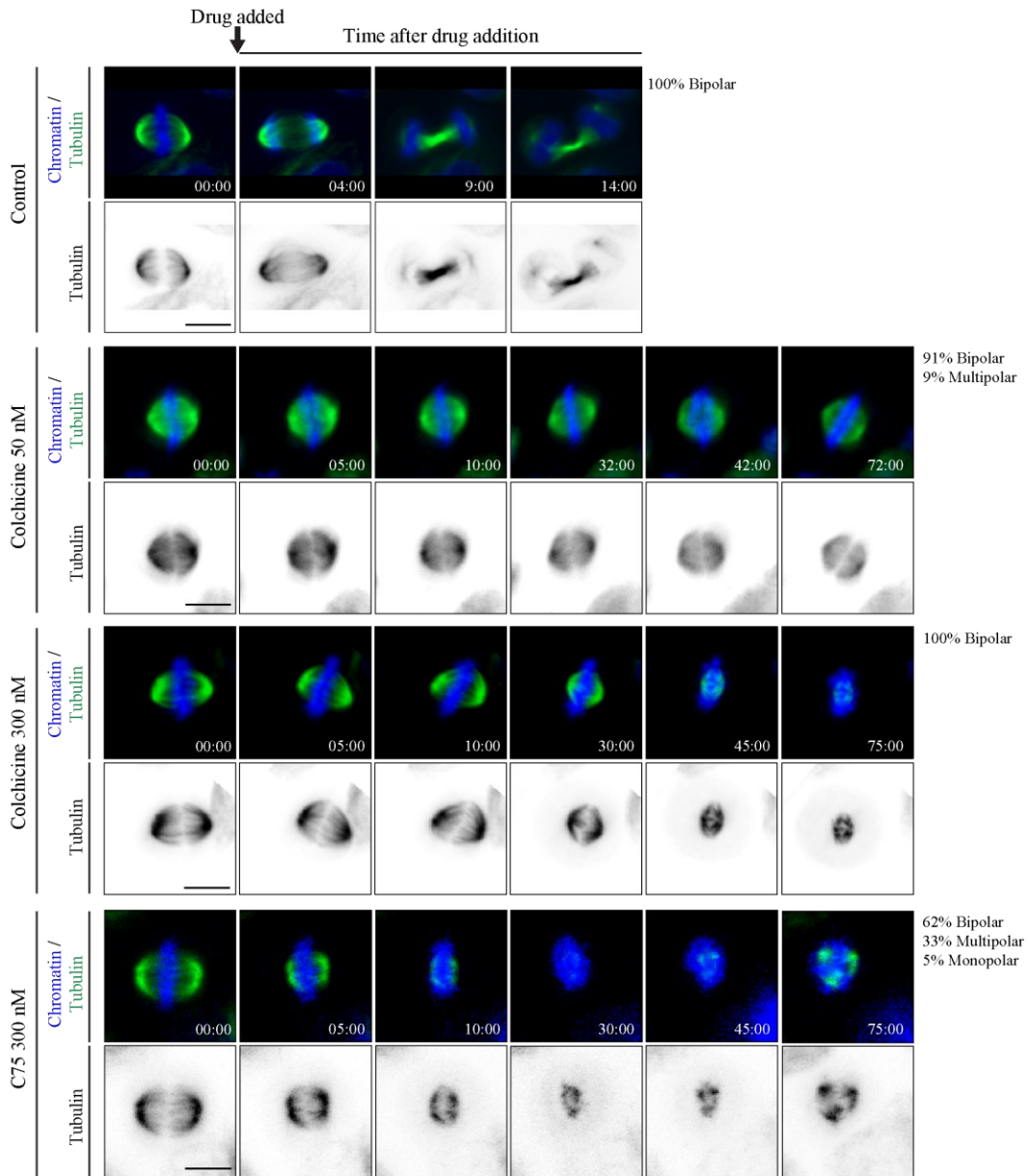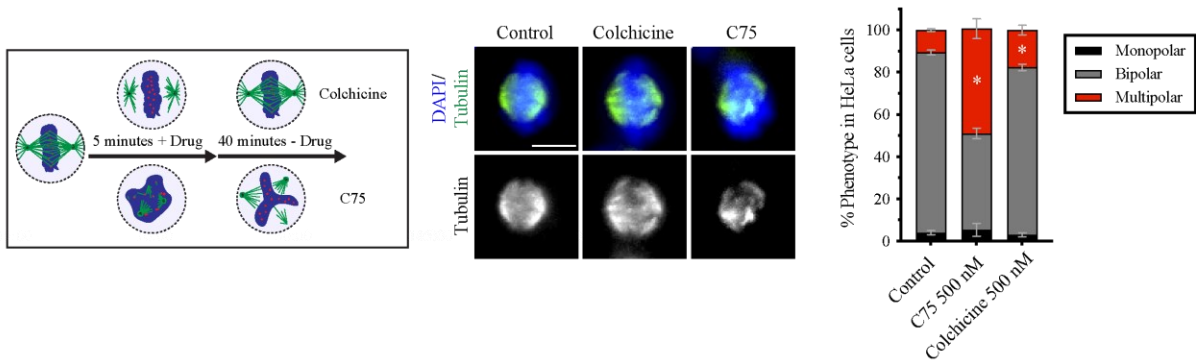
Figure 22: C75 and colchicine cause different spindle phenotypes. (A) Timelapse images show live HeLa cells co-stained for DNA (Hoechst 33342; blue) and microtubules (SiR-tubulin; green). Times are indicated in minutes. An arrow points to the time of addition of DMSO (control; n = 15), 50 nM colchicine (n = 33), 300 nM colchicine (n = 20) or 300 nM of C75 (n = 21) to cells. The proportion of cells with bipolar, multipolar or monopolar spindles are indicated. (B) A cartoon schematic shows how HeLa cells were treated with drug (DMSO, 500 nM C75 or colchicine) for 5 min, then fixed 40 min after the drugs were washed out. Underneath, images show fixed HeLa cells co-stained for DNA (DAPI; blue) and tubulin (green or white) after treatment with C75 or colchicine. To the right, a bar graph shows the proportion of cells with monopolar (black), bipolar (dark grey) or multipolar (red) spindles. Bars show standard deviation and asterisks indicate $p < 0.05$ by multiple t tests vs. control. The scale bar for all cells is 10 μm.

Next, we determined if C75 and colchicine cause spindle phenotypes when added prior to mitosis. HeLa cells stably expressing GFP- or mCherry-tagged tubulin were imaged entering mitosis after treatment with 50 nM colchicine or 300 nM C75 in late S or G2 phase (Fig. S5A,B). Control cells entered mitosis with bipolar spindles that progressed to telophase (12/12, Fig. S5A; 22/22, Fig. S5B). We observed multiple centrosomes clustering to form bipolar spindles in many control cells (e.g. Fig. S5B). Colchicine caused multipolar spindles to form without transitioning through a bipolar state in 24% of cells (18/74), while only 9% of C75-treated cells (4/44) had multipolar spindles (Fig. S5A,B). This data shows that the multipolar spindle phenotypes observed after longer colchicine treatments arise prior to mitosis, while the multipolar spindles caused by C75 occur in metaphase, after bipolar spindles have already formed.

Spindle microtubules regrow in the presence of C75

To further compare the effect of C75 and colchicine on microtubules in cells, we monitored the re-growth of microtubules in the presence of the two compounds. HeLa cells stably expressing GFP-tagged tubulin were cold-treated for 30 min to depolymerize microtubules, then 300 nM C75 or colchicine was added upon upshift to 37 °C, noting that the temperature upshift took a few minutes. Cells with bipolar spindles were imaged during recovery as shown in Fig. 23A. All of the control cells formed functional spindles and were in telophase by ~ 40 min. In colchicine-treated cells, microtubules decreased with no detectable GFP signal by ~ 50 min, as expected given its low off-rate (24/24; Fig. 23A). In C75 treated cells, microtubules also decreased, but GFP regained intensity as microtubules regrew to some extent in all cells (15/15; Fig. 23A). To further characterize these phenotypes, we quantified changes in spindle pole volume and maximum intensity over time (Figs. 23A–D, S6A,B). The spindle poles were identified as spherical objects in 3D-reconstructed cells in Imaris v.9.7.2 (Bitplane), which were tracked and quantified over time for changes in volume and intensity. Colchicine-treatment caused a decrease in the volume and maximum intensity of spindle poles over time (Figs. 23A–D, S6A,B). While some fluctuation was observed, there was a net linear decrease in volume and intensity over time as indicated by the best-line fits with negative slopes (Figs. 23A,B, S6A,B). Heatmaps of the proportional changes in spindle volume or intensity show how each pole decreased over time, albeit some sooner than others (purple to orange; Figs. 23D, S6B). However, C75-treatment caused an initial decrease in spindle volume or intensity followed by recovery in multiple cells (Figs. 22A,B, S6A,B). This was
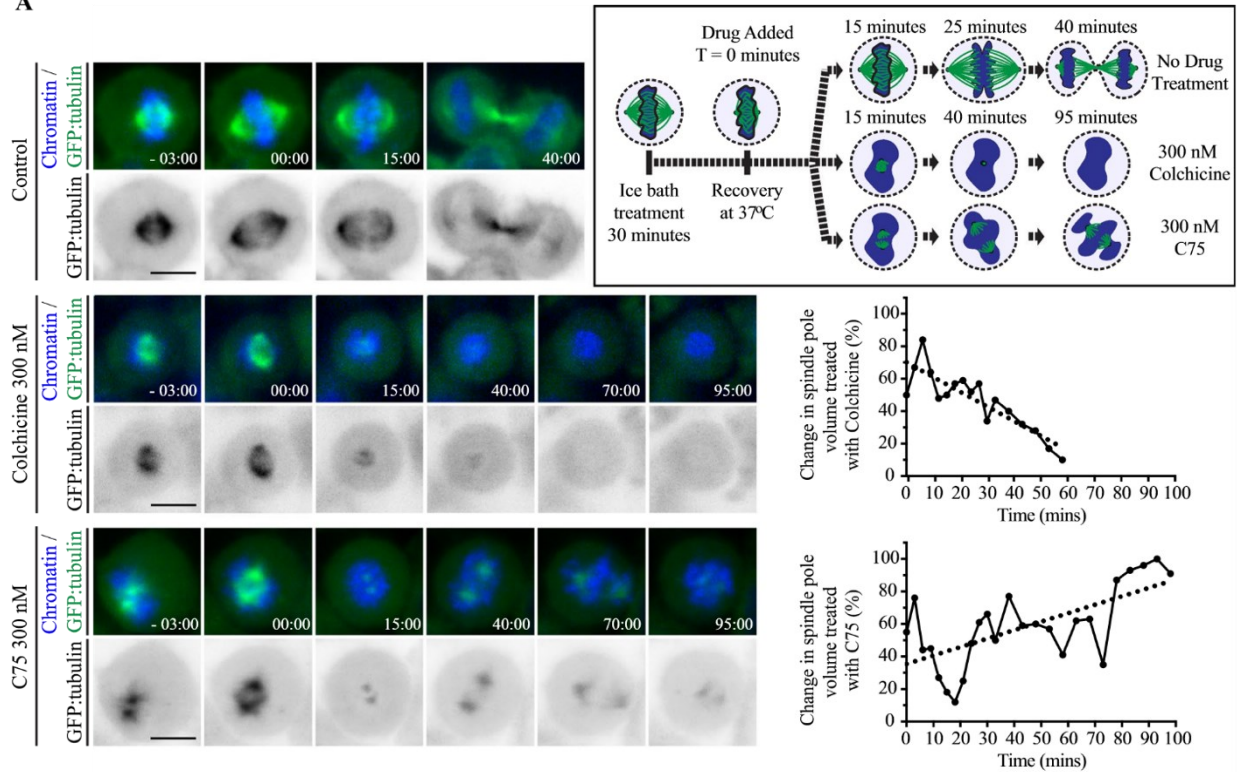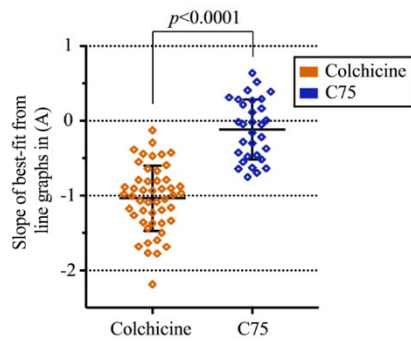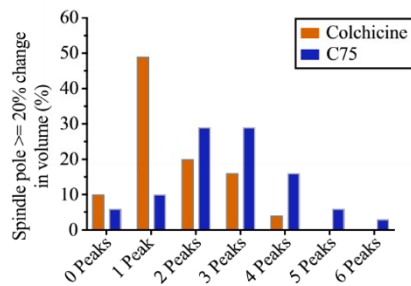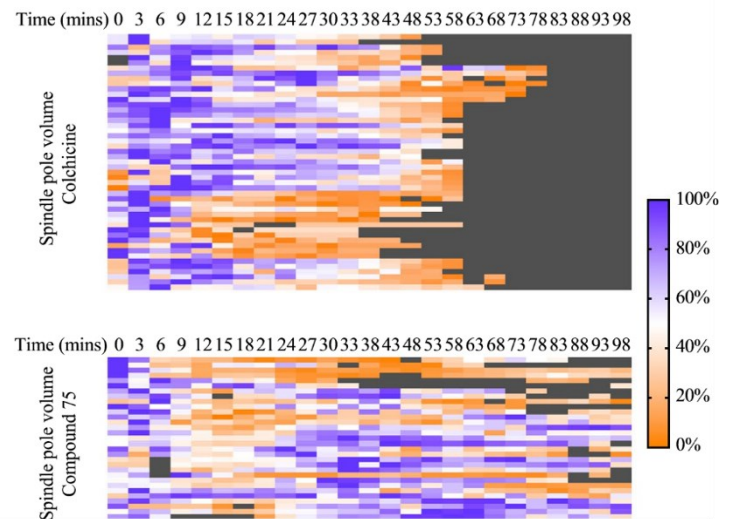
Figure 23: **Microtubules recover in the presence of C75**. (A) A cartoon schematic (box at upper right) shows the experimental design. HeLa cells were cold-treated for 30 min in an ice bath to collapse microtubules, then upshifted to 37 °C and imaged for microtubule regrowth in the presence or absence of 300 nM colchicine or C75. Timelapse images show live HeLa cells stably expressing GFP:tubulin (green) and co-stained for DNA by Hoechst (blue), with the times indicated in minutes. DMSO (control, n = 6), 300 nM colchicine (n = 24) or 300 nM C75 (n = 15) was added at 0 min. To the right, line graphs show changes in spindle pole volume (%; Y-axis) over time (X-axis) after addition of colchicine or C75 (dotted line indicates best-fit). (B) A scatter plot shows the distribution of slope values obtained from best-fit line graphs (Y-axis) for the changes in each spindle pole volume over time after treatment with C75 or colchicine as in A). Significance was determined using the two-tailed Welch's t test, p < 0.0001. (C) A bar graph shows the number of peaks (X-axis) with an amplitude equal to or greater than 20% of the maximum volume of the spindle pole after treatment with C75 or colchicine (Y-axis). (D) Heat maps show the change in volume (%) of individual spindle poles over time (minutes, at the top) in cells treated with colchicine or C75 as in A). Purple indicates larger volumes while orange indicates smaller volumes. Each line represents a different spindle pole.

evident in the heatmaps where spindle poles continued to recover and fluctuate over time (alternating orange and purple; Figs. 23D, S6B). To better understand this oscillatory pattern, we quantified the number of peaks where there was a > 20% change in pole volume (Fig. 23C). More poles in C75-treated cells had > 2 peaks (54 vs. 46% with 1 or 2) compared to colchicine-treated cells (31 vs. 69% with 1 or 2; Fig. 23C). Thus, microtubules can polymerize in the presence of C75, but this growth is not evenly distributed between the poles. This data suggests that C75 could have a high off-rate and/or a limited window of accessibility to microtubules.

The C75 phenotype is reminiscent of a disruption in microtubule polymerization

Since C75 destabilizes spindle microtubules, we compared spindle phenotypes with those caused by depletion of CKAP5/ ch-TOG, a microtubule polymerase that balances the activity of MCAK, a microtubule depolymerase[27,35,154,162]. HeLa cells treated with ch-TOG siRNAs had an increase in the proportion of bipolar spindles with misaligned chromosomes (51 vs. 17% for control) and multipolar spindles (42 vs. 8% for control; Fig. 24A). As shown in Fig. 20C, we saw an increase in these phenotypes with increasing amounts of C75. Given these similarities, we determined if C75 impacts ch-TOG localization. Metaphase HeLa cells co-expressing ch-TOG shRNA for endogenous knockdown and RNAi-resistant ch-TOG:GFP were imaged immediately after treatment with 300 nM C75. In control cells, ch-TOG localized to the spindle poles and microtubules, which decreased during anaphase, and was no longer detectable in telophase (13/13; Fig. 24B). Treatment with 300 nM C75 caused ch-TOG to increase at the spindle poles, then dissipate after ~ 50 min (10/10; Fig. 24B). Measuring the change in maximum intensity of ch-TOG at spindle poles within individual cells revealed differences in the signal at one pole relative to the other. While there was some variability in control cells, ch-TOG continued to reciprocally increase or decrease at either pole for a longer time in C75-treated cells (Fig. 24C). We then measured the proportional difference in ch-TOG intensity between the two poles in multiple C75-treated cells where each bar corresponds to a single time point (Fig. 24D). For most cells, ch-TOG alternated from one pole to the other (bars extending to right or left of the net 0 line). This data suggests that C75 treatment causes changes in ch-TOG localization where it first accumulates at the spindle poles, but then unevenly oscillates between the poles as it dissipates. These changes in ch-TOG localization likely prevent it from properly controlling microtubule polymerization.

A

	Bipolar	Bipolar Misaligned	Multipolar
DMSO	83%	7%	9%
ch-TOG siRNA		54%	45%

DAPI / Tubulin

B

HeLa ch-TOG:GFP

DMSO: -01:00, 00:00, 05:00, 10:00, 30:00

300 nM C75: -01:00, 00:00, 05:00, 10:00, 30:00, 50:00, 80:00
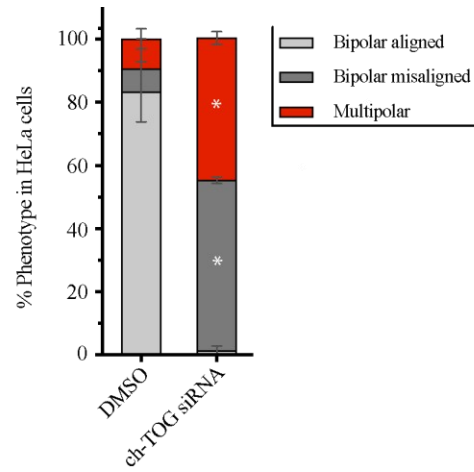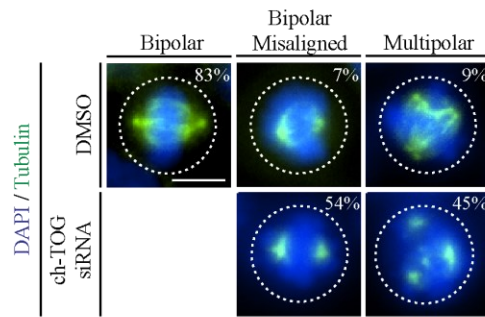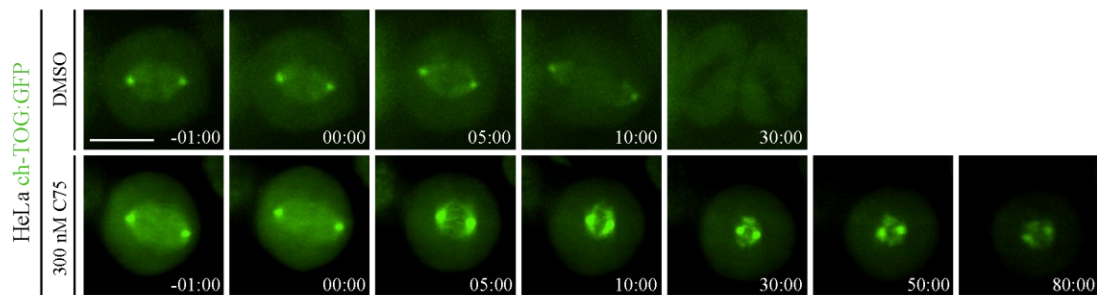
C
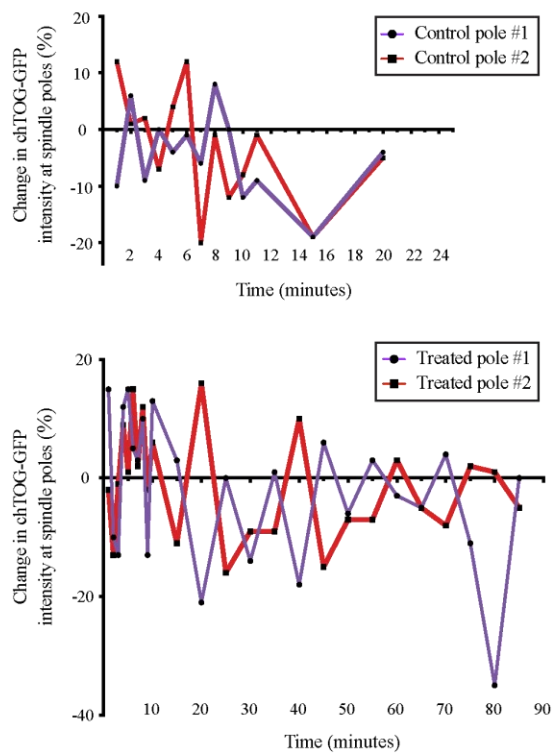
D
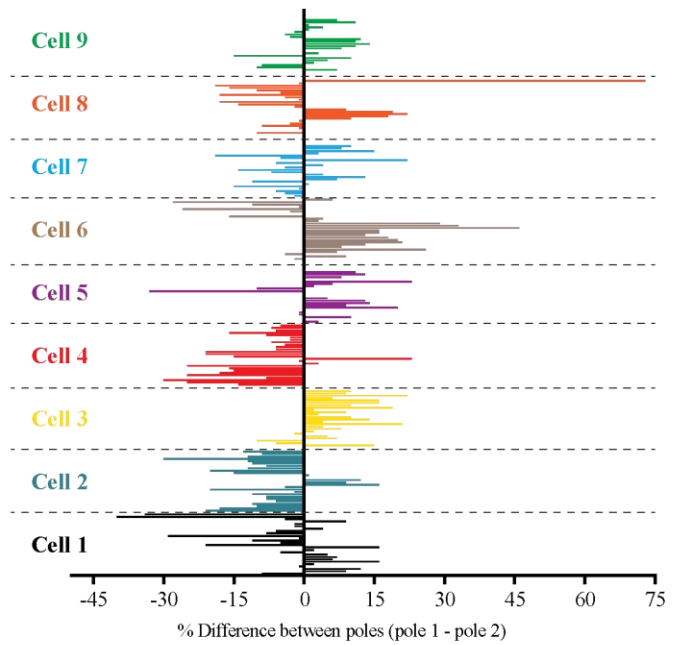
Figure 24: C75 causes a change in ch-TOG localization. (A) Images show fixed HeLa cells stained for DNA (DAPI, blue) and microtubules (tubulin, green) after treatment with ch-TOG siRNAs. The proportion of cells with bipolar spindles and aligned chromosomes, bipolar spindles with misaligned chromosomes, or multipolar spindles is indicated on the images. The scale bar is 10 µm. A bar graph shows the proportion of cells (%) with bipolar spindles (light grey), bipolar spindles with misaligned chromosomes (dark grey) or multipolar spindles (red). Bars show standard deviation. Asterisks show p < 0.0001 with respect to control (DMSO) using two-way ANOVA with a 99% confidence interval. (B) Timelapse images show live HeLa cells expressing ch-TOG:GFP (green) upon addition of DMSO (control, n = 13) or 300 nM C75 (n = 10). Times are indicated in minutes. The scale bar for all cells is 10 µm. (C) Line graphs show the percent change in ch-TOG:GFP signal intensity (Y-axis) over time (minutes, X-axis) for each pole in an individual control or C75-treated cell. (D) A bar graph shows the relative change in proportion of ch-TOG from pole 1 to pole 2 (arbitrarily chosen) over time (each bar is 1 min for the first 10 min, then 5 min) for individual C75-treated cells. Each cell is a different colour.

C75 and paclitaxel enhance spindle phenotypes at a cellular level

Next, we assessed the effect of combining C75 with paclitaxel, a microtubule-stabilizing drug, in HCT116 cells. HCT116 cells were treated with paclitaxel, C75 or both for 7 h, then fixed and co-stained for chromatin (DAPI; blue) and microtubules (green). Paclitaxel caused a significant increase in the proportion of HCT116 cells with monopolar, bipolar misaligned and/or multipolar spindles (Fig. 25A). The majority of phenotypes did not change between 2.5 and 50 nM of paclitaxel, although 10 nM paclitaxel caused a significant increase in bipolar misaligned spindles (Fig. 25A). As before, increasing concentrations of C75 caused a significant increase in the proportion of cells with spindle phenotypes (Fig. 25A). Combining 2.5 nM paclitaxel with 100 or 200 nM C75 caused an increase in the proportion of cells with multipolar spindles, especially at lower concentrations. To quantify this effect, we calculated the ratio (R) for the observed proportion of cells with multipolar spindles compared to those predicted additively. While $R > 1$ for 2.5 nM paclitaxel with 100 nM C75 (2.17 ± 0.73), it was close to 1 for 200 (1.45 ± 0.47) and 300 nM (1.19 ± 0.2; Fig. 25A). Thus, the multipolar phenotype caused by C75 was enhanced by paclitaxel.

We noticed that spindle poles were closer together in paclitaxel-treated cells compared to C75. We quantified this by measuring the distance between spindle poles in the different treatments (Fig. 25B). While increasing paclitaxel from 2.5 nM to 10 nM caused the poles to move closer together, 400 nM C75 caused them to move significantly further apart on its own or in combination with paclitaxel (Fig. 25B). This data suggests that C75 and paclitaxel independently affect microtubules, and C75 causes multipolar phenotypes regardless of microtubule stability. In support of this, the number of spindle poles was similar in cells treated with 400 nM C75 alone or in combination with 2.5 nM paclitaxel (Fig. 25C).

Next, we tested the effects of combining C75 and paclitaxel on spheroid growth. Multicellular tumour spheroids are formed by cancer cells grown in 3D. Due to their increased complexity, spheroids better predict the efficacy of drugs *in vivo* compared to cells grown as monolayers[150,151]. For example, spheroids contain distinct populations of cells that are either quiescent or proliferating. We found that adding 250 nM of C75 or 10 nM of paclitaxel prevented HCT116 spheroids from growing 6 days after treatment, unlike control spheroids treated with DMSO (Fig. 25D). Combining 250 nM of C75 with 10 nM of paclitaxel caused a significant

A

C

B

D
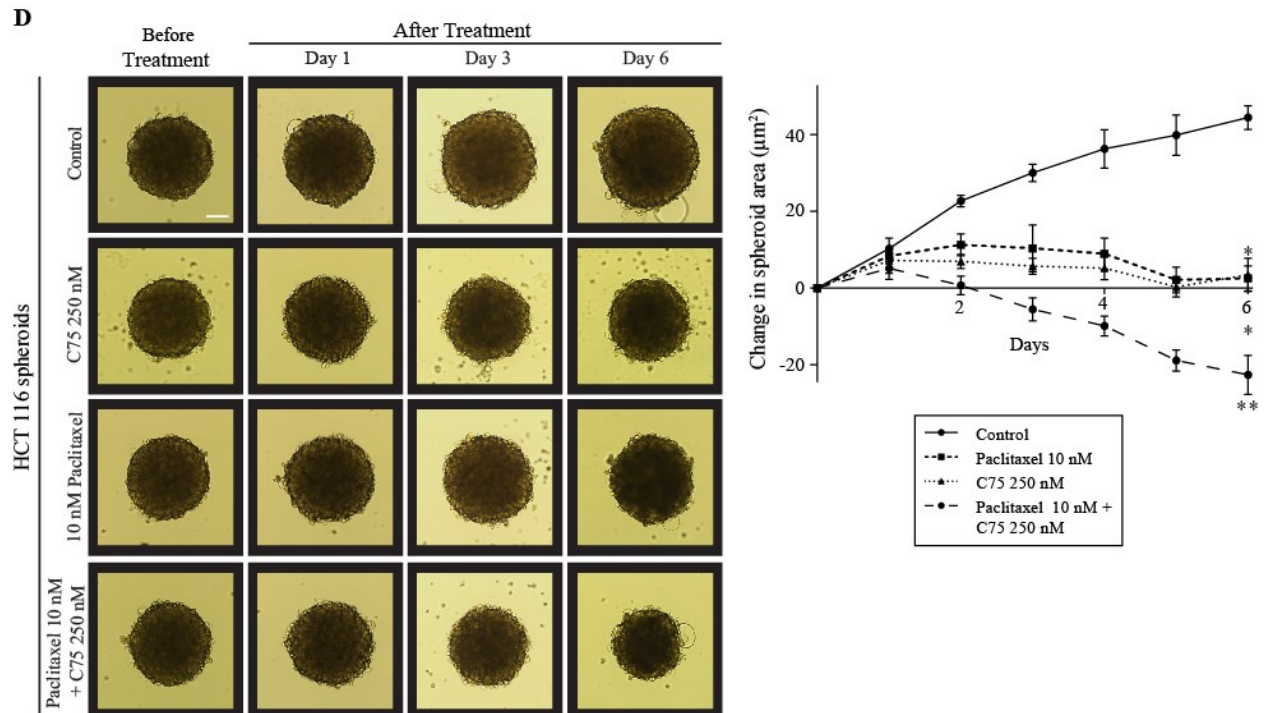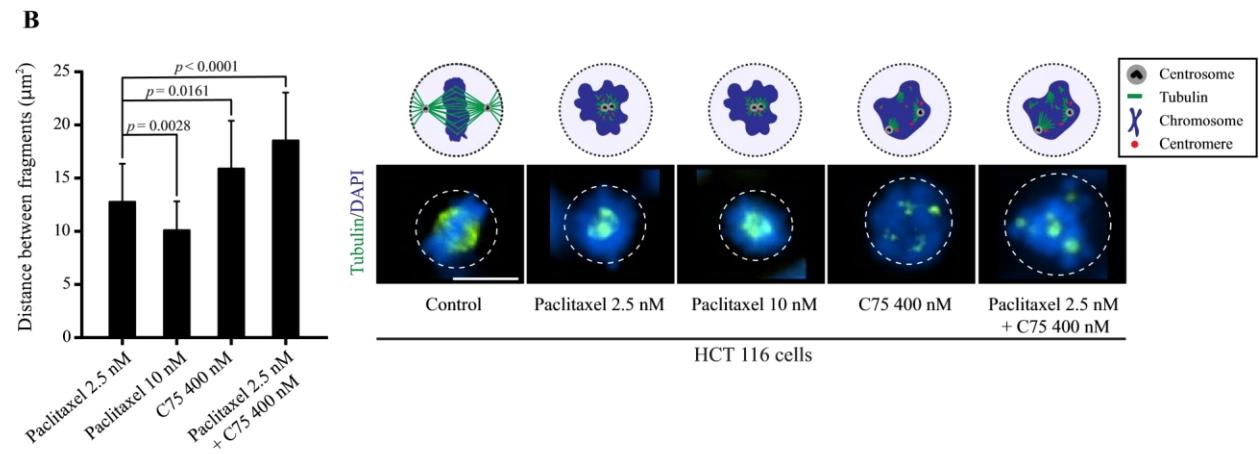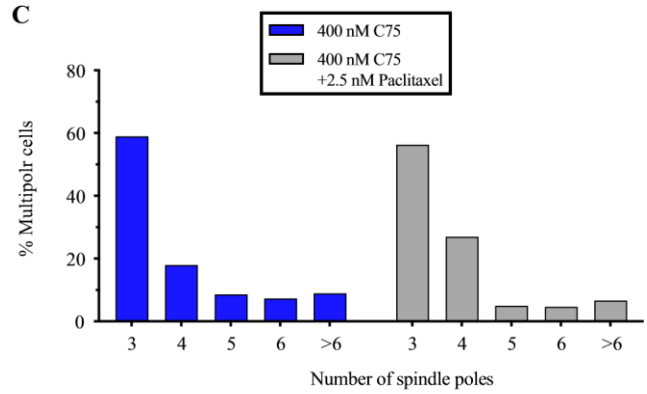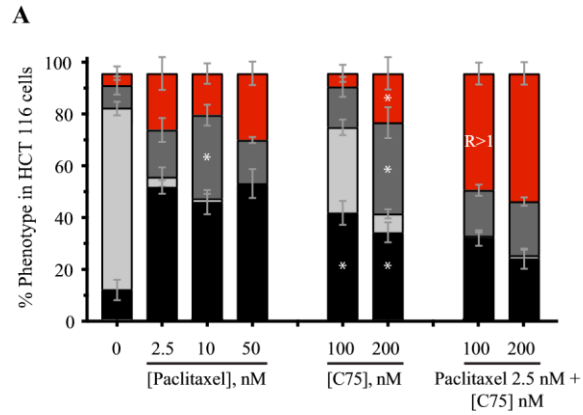
Figure 25: Combining C75 and paclitaxel cause enhanced phenotypes in HCT116 cells. (A) Bar graphs show the proportion of HCT116 cells with bipolar aligned (light grey), bipolar misaligned (dark grey), multipolar (red) or monopolar (black) spindles 7 h after treatment with control (DMSO), varying concentrations of paclitaxel or C75, or both as indicated. The bars show standard deviation. The asterisks indicate $p < 0.05$ determined by multiple t tests for C75-treated vs. control cells. The combination treatments were compared to predicted ratios as indicated. (B) A bar graph shows the distance between spindle poles/fragments measured in HCT116 cells after treatment with paclitaxel or C75 or both as indicated. Also shown are immunofluorescence images of HCT116 cells co-stained for DAPI (chromatin; blue) and tubulin (microtubules; green) for the different treatments. The scale bar is 10 μm, and the p values are indicated as determined by the student's t test. (C) A bar graph shows the percentage of multipolar HCT116 cells from B) with different numbers of spindle poles after treatment with 400 nM C75 or 400 nM C75 (blue) and 2.5 nM paclitaxel (light grey). (D) Brightfield images show HCT116 spheroids over 6 days before and after treatment with control (DMSO; n = 5), 250 nM C75 (n = 5), 10 nM paclitaxel (n = 5) or both (n = 5). The scale bar is 0.1 mm. A line graph to the right shows the change in spheroid area ($μm^2$) over time. Bars on all graphs show standard deviation. The asterisks are $p < 0.05$ as determined by the student's t test.

decrease in spheroid size compared to each compound on their own (Fig. 25D). Thus, a potential application for C75 could be in combination therapies with Taxol to lower doses required to treat cancers.

4.6 Discussion

Here we describe how C75, a microtubule-destabilizing compound, works in cells. C75 is a derivative of a family of thieonoisoquinoline compounds with several groups amenable to modification[156,180]. We previously found that C75 prevents microtubule polymerization and competes with colchicine for tubulin-binding *in vitro*[180]. Here, we show that C75 caused a range in toxicity depending on the cell type, with stronger effects on HeLa (cervical cancer), A549 (lung cancer) and HCT116 (colorectal cancer) vs. HFF-1 (foreskin fibroblast) cells. Increasing concentrations of C75 caused cells to accumulate in mitosis, where cells arrested due to aberrant spindles (Figs. 19, 20). While the spindle phenotypes caused by longer treatments of C75 were similar to those caused by colchicine, C75 and colchicine synergized at sub-lethal concentrations, suggesting that they have different effects on microtubules in cells (Fig. 21). Indeed, we found that they caused different spindle phenotypes depending on the cell cycle stage (Figs. S5, 22, 23), likely reflecting differences in binding affinity and/or accessibility to microtubules. In addition, microtubules regrew in the presence of C75. To our knowledge, this is not typical for microtubule-destabilizing drugs and we did not observe microtubule recovery with different concentrations of colchicine (e.g. 50 or 300 nM; Figs. 22, 23).

The similarity in spindle phenotypes caused by C75 and ch-TOG depletion is striking[163](Fig. 24). Many MAPs work together to form functional, bipolar spindles[18]. The loss of ch-TOG causes an imbalance in enzymatic activities, including the microtubule depolymerase MCAK. MCAK destabilizes microtubule ends to correct kinetochore attachments, which is controlled by Aurora B kinase, and focuses the asters into spindle poles via Aurora A kinase[163,164,182,183]. ch-TOG-depleted cells have phenotypes consistent with these roles including disorganized spindle poles and misaligned sister chromatids[162]. We observed the same phenotypes in C75-treated cells. Based on this we speculate that: (1) C75 could destabilize the minus ends of microtubules, but after microtubule collapse, its high off-rate permits new polymers to form due to local increases in the critical concentration of free tubulin, (2) C75 disrupts microtubules

required for the localization of microtubule regulators, such as ch-TOG, when they are needed to form bipolar spindles, and/or (3) changes in accessibility to C75 could arise due to competition with factors that nucleate or polymerize microtubules[161,165]. The accumulation and oscillation of ch-TOG between spindle poles in C75-treated cells could contribute to changes in microtubule dynamics. For example, ch-TOG requires binding to both microtubule polymers and tubulin dimers to polymerize microtubules, and the loss of microtubules could prevent this function, favoring other activities from other enzymes.

Vinblastine similarly has complex effects on microtubules, which could contribute to its success as an anticancer drug. *In vitro*, vinblastine causes depolymerization at minus ends, and prevents growth at the plus ends[171]. In cells, vinblastine can alter centrioles and/or reduce microtubule dynamics to cause multipolar spindles[172,173]. We propose that C75 shares some similarities with vinblastine with accessibility and/or binding kinetics that favors microtubule depolymerization at the minus ends during mitosis. Vinblastine is one of the few microtubule-destabilizing drugs that is used as an anti-cancer therapy, and its ability to cause spindle phenotypes at low concentrations without disrupting the microtubule polymer mass could minimize side-effects[148]. Although C75 has a high IC_{50} value by comparison (e.g. 30–100-fold higher), the unique effect on microtubules and high selectivity for metaphase cells could make it an interesting compound to consider for *in vivo* use. Importantly, we are making new derivatives with improved IC_{50} values and solubility that could replace C75 as a lead.

The multipolar spindle phenotype caused by C75 suggests that it affects centrosomes. Centrosome integrity relies on the TACC3-clathrin-ch-TOG complex, and it is interesting that C75 causes loss of integrity prior to the imbalanced recovery of tubulin and ch-TOG at spindle poles[155]. Many microtubule-targeting drugs cause multipolar spindles, but this typically occurs after a long time, or as we showed for colchicine, upon mitotic entry[172,184–186]. Cancer cells with high aneuploidy and amplified centrosomes rely on clustering mechanisms to form bipolar spindles[178,185,187,188]. Thus, C75 may be effective for the treatment of cancers with high centrosome numbers[189]. Indeed, the proportion of cells with multipolar spindles caused by C75 varied among the different cancer cell types, likely reflecting genetic differences impacting centrosome integrity, clustering and/or microtubule dynamics. Interestingly, low concentrations of C75 caused an increase in the proportion of monopolar spindles in HCT116 cells. Aurora A kinase and ch-TOG

are over-expressed in HCT116 cells causing increased microtubule assembly[27,35,155,162]. Given its potentially high off-rate, low concentrations of C75 could increase critical concentrations of free tubulin to further stabilize microtubules and block centrosome separation. However, higher concentrations of C75 caused the formation of multipolar spindles, including cells that had also been treated with paclitaxel, which stabilizes microtubules (Figs. 21, 25). We also found that combining C75 and paclitaxel more effectively regressed multicellular tumour spheroids compared to each on their own (Fig. 25). One of the compounds could have improved accessibility due to changes in the microtubule polymer caused by the other compound, and spindles are less likely to recover if subthreshold doses can cause additive effects. Our data supports the exploration of C75's anti-cancer potential, including predicting cell types that could respond to C75 with high efficacy.

Chapter 5. Conclusions and future directions

5.1 Overview

My thesis explores different ways of developing novel anti-cancer therapies. In chapter 2, I reveal how the requirement for anillin in cytokinesis and mechanism controlling ring assembly changes with ploidy. Since cancer cells acquire chromosomal instability and gain ploidy as they progress to more advanced states, my findings could reveal that anillin is an exciting novel target to develop novel anti-cancer therapies. By revealing a physiological adaptation that is unique to cancer cells, drugs or therapies that lower anillin levels could block cancer cell division without impacting healthy cells. In chapters 3 and 4, I reveal how 16g/C75 is a lead compound from a family of thienoisoquinoline derivatives with anti-cancer potential. We identified key functional groups that are important for biological activity, and we identified tubulin as the molecular target. SAR studies can be performed to find even better derivatives with improved efficacy and selectivity. Importantly, C75 causes a unique phenotype that is selective to metaphase and results in the formation of multipolar spindles, which is more similar to paclitaxel-treatment vs. microtubule-depolymerizing agents such as colchicine. This exciting finding could support that this family of compounds has the potential to be developed as a novel anti-cancer drug.

5.2 Cells with higher ploidy have stronger requirements for anillin in cytokinesis

In Chapter 2, I reveal that anillin requirement varies with cell type, which may be due to a switch in the mechanisms controlling ring assembly in response to ploidy. We found that HeLa cells that are hyper triploid require significantly more anillin to support cytokinesis compared to HCT116 cells that are near diploid, and inducing ploidy in HCT116 cells changed anillin's requirement, localization and function to be similar to HeLa cells. We speculated that this was because importins became a dominant mechanism for controlling ring position in cells with higher ploidy compared to other pathways – our model shows how importins are predicted to be more uniformly distributed in cells with lower ploidy, but they only reach a critical threshold in the equatorial plane after the chromosomes segregate in cells with higher ploidy. Indeed, we found that mutating the NLS caused drastic changes in anillin's localization in all cells, but specifically caused cytokinesis phenotypes in cells with higher ploidy. Other pathways that could support ring assembly in cells with lower ploidy include spindle-dependent and/or kinetochore pathways. To

further test our model, we could perturb these pathways in combination with the chromatin-sensing pathway in cells with lower ploidy. Our lab has done this before to demonstrate the relative contributions of the astral microtubule vs. central spindle pathway[82].

To support our model, it is necessary to show that importins are indeed differently distributed, and that importins are required for anillin function. In order to measure this, another graduate student just generated a HeLa cell line where importin-β is endogenously tagged with mNeonGreen, and will do the same in HCT116 cells. Imaging cells during mitosis would reveal differences in importin-β cortical enrichments in cells with lower vs. higher ploidy. I also performed FRET experiments using a probe developed by the Kalab lab which measured the amount of free importin[32]. While promising, more work needs to be done to obtain more precise measurements (e.g. using FLIM) in metaphase and anaphase cells with lower vs. higher ploidy.

We also found that anillin is required for later stages of cytokinesis in HCT116 cells, while it is required for ring positioning in HeLa cells. It is the first time to our knowledge that anillin was directly shown to be required for midbody formation in human cells. The role of anillin in late cytokinesis has been challenging to study because most of our knowledge and studies of cytokinesis have been done in HeLa cells, where anillin is required early. Co-localization studies showed that anillin localizes to the midbody with citron kinase, and recruits septins through its PH domain[125]. Also, the overexpression of anillin causes abscissions delays[109]. Our findings illustrate the importance of studying different cell types and organisms, as our current models likely do not reflect the true diversity of how many biological processes are governed. For example, in the two-cell *C. elegans* embryo, we found that there are different levels of cortical ANI-1 (*C. elegans* anillin) in the AB and P1 cells fated to be somatic tissue and germline, respectively. In addition, ANI-1 is regulated by the chromatin pathway in AB cells, but not in P1 cells suggesting that there are different mechanisms controlling anillin function in these cell types[79].

Our findings reveal that anillin or the chromatin pathway could be ideal to target as a novel anti-cancer therapy, especially since cancer cells typically have higher than normal ploidy. In addition, cytokinesis failure can trigger p53-independent apoptosis, or can be a normal part of tissue development[190]. One cancer that could be particularly attractive to target by anillin inhibition or knockdown is liver cancer caused by hepatocellular carcinoma (HCC). During differentiation, a large portion of hepatocytes gain ploidy in part due to cytokinesis failure[191]. This gain in ploidy

is thought to be required to secrete enzymes needed for metabolism and lipid biosynthesis[192]. Another possible function is for tissue regeneration, since it was demonstrated that polyploidization is necessary for heart and kidney regeneration and repair processes[193,194]. HCC have multiple cytokinesis regulators are highly upregulated, including anillin[191,195]. A recent study found that knocking down anillin in the liver of mice reduced the incidence of liver tumours with restored healthy tissue function[195,196]. Other studies showed the polyploid state of hepatocytes is more resistant to forming tumours, and analysis of the HCC-derived tissue showed that the proportion of binucleate cells was heavily reduced at the expense of mononucleated cells[197]. Thus, one explanation for this is that HCCs rely more heavily on the chromatin sensing pathway and anillin to support cytokinesis, and could be sensitive to the loss or disruption of these components. Very few biological studies have been performed using healthy hepatocytes or HCCs, and more studies are needed to fully understand how their mechanisms regulating cytokinesis differ to obtain support this hypothesis. To our knowledge, there are no anillin inhibitors, although several RNA-based therapies are in development. Our group is collaborating with Dr. Forgione's group to develop compounds that specifically inhibit anillin. It is exciting to speculate the anti-cancer potential of targeting anillin.

5.3 Identifying C75 as a potential anti-cancer compound

In chapter 3, our collaborators synthesized a family of thienoisoquinoline compounds that we screened for efficacy in A549 cancer cells, and found an active derivative, 16g/C75. We found that C75 causes cells to arrest in mitosis, leading to cell death. We also found that it works with similar efficacy in other cancer cell types, with ~3-fold selectivity compared to fibroblasts. We also found that it binds to the colchicine site on tubulin and prevents microtubule polymerization *in vitro*. We were surprised to see that 16g/C75 worked more efficiently *in vitro* compared to colchicine. Given that colchicine has lower IC_{50} values than C75, this suggests that they have different accessibility and/or molecular targets within the cell. We also show that C75 effectively shrinks multi-cellular tumour spheroids *in vitro*, and although preliminary, we collaborated with Dr. Harkness (University of Saskatchewan) to show that C75 can reduce triple negative breast cancer (TNBC)-derived xenograft tumours in mice. C75 was identified by modifying the A and D ring from the thienoisoquinoline scaffold. Recently, new derivatives were generated with a modified C ring, which revealed C173 with IC_{50} values of ~50 nM on TNBC cells with 5-fold

selectivity compared to non-cancerous MCF10A cells. C173 also has improved solubility, and retention, suggesting that it may replace C75 as our new lead compound.

In chapter 4, we characterized the mechanism of action of C75 at the cellular level, and compared it to other microtubule-targeting drugs. We found that C75 arrests cancer cells in mitosis and causes multipolar phenotypes by a mechanism that appears to be unique compared to other microtubule-targeting drugs. Live imaging on HeLa cells after treatment revealed that colchicine progressively depolymerizes spindle microtubules and can lead to fragmented poles over time, or if cells are treated in prometaphase. In comparison, C75 causes rapid microtubule depolymerization and pole fragmentation, followed by microtubule regrowth to form multipolar spindles. Furthermore, they show phenotypic synergy with each other suggesting different mechanisms of action in cells. The formation of multipolar spindles is reminiscent of paclitaxel treatment, and we also compared C75 with paclitaxel, alone and in combination. We found that since paclitaxel stabilizes microtubules to reduce dynamics, it also takes time to form multipolar spindles, which appear more clustered compared to C75. C75 caused these clusters to move apart, again suggesting a unique mechanism of action.

It is not clear why C75 shows such a unique phenotype in cells. We compared HeLa, A549 and HCT116 cells and did see some variability in the extent of multipolar spindles. This suggests that their genetic backgrounds could differentially sensitize cells. For example, ch-TOG is highly overexpressed in HCT116 cells which have a higher incidence of monopolar spindles, and C75-treatment caused fewer multipolar spindles in HCT116 cells compared to HeLa or A549 cells. The mechanism by which C75 causes spindle fragmentation is not clear. We show that the centrosomes fragment vs. displacement of pericentriolar material, based on localization of centrin-2. We also found that ch-TOG localization is changed. Instead of localizing to the spindle and centrosomes, it localizes only to the centrosomes, and does not dissipate when it typically would in control cells. Based on its ability to prevent microtubule polymerization *in vitro*, C75 could bind to free tubulin to prevent their incorporation into new polymers, and/or directly destabilize microtubules at the plus and/or minus ends. The displacement of a polymerase like ch-TOG could also favor depolymerization by MCAK. Also, since cancer cells have pseudo-bipolar spindles that rely on microtubules for clustering centrosomes, the disruption of microtubule minus ends also could cause centrosomes to dissociate. The regrowth that occurs shortly after could be because the

critical concentration of free tubulin now favors growth in the absence of enzymes, and/or outcompetes drug-bound tubulin. These predictions are based on our knowledge of another microtubule-targeting drug called vinblastine. Vinblastine is currently used to treat a plethora of cancers and has IC$_{50}$ between 2-12 nM depending on the cell type[184]. Vinblastine can have different effects on the plus or minus ends of microtubules[198]. For example, vinblastine can bind to the minus end of microtubules and destabilize the lattice, which further disrupts the bipolar spindle, including dissociation between the mother and daughter centrioles[199]. Through this effect, vinblastine induces multipolar spindles and cell death[184,200].

As mentioned earlier, patients often gain resistance to paclitaxel or experience severe side-effects and there is a need to find alternative treatments. Microtubule-targeting is a highly successful approach in the clinic, and finding derivatives that could overcome these limitations caused by paclitaxel could be ideal. We show that C75 enhances the multipolar phenotype when used with paclitaxel, and could be considered in combination therapies. In addition, we have done some preliminary studies to show that C75 retains efficacy in Taxol-resistant TNBC cells. However, more studies are needed to determine if any of the different mechanisms that lead to resistance can also affect C75 (or derivatives) so we can predict cancers that would be ideal (or not) to treat. As mentioned above, we also have a new derivative with high efficacy in TNBC cells. Repeating some of our studies with this new derivative may reveal even stronger combination data. We are also performing bioinformatics studies to identify genes that are mutated or alternately expressed in TNBCs so that we can identify TNBCs that would be predicted to respond well to treatment with our derivatives.

5.4 Conclusions

Although there has been some progress in extending the lifespan of patients affected by some cancers, others remain relatively unchanged. All cancers are heterogenous, and often lack sufficient genetic changes that can be selectively targeted. Thus, the most successful therapies remain those that target more general physiological processes. Another limitation is that drugs like paclitaxel and vinblastine are plant-derived compounds, for which modifications are very challenging. My thesis describes a physiological process that could be targeted in highly progressive cancers, which involves the protein anillin. Interestingly, anillin is one of the most highly upregulated proteins in all (most) cancers outside the brain and is used as a prognostic

marker. Understanding why this protein may be so highly upregulated is crucial to reveal if it could be ideal to target as a novel therapy. My thesis also describes a new family of compounds that target microtubules with high efficacy and selectivity in cancer cells, and which are amenable to modifications. We already found a derivative with improved efficacy, demonstrating the power of the system. My findings could lead to the development of new cancer therapies and an increase in therapeutic options.

References

1.   Hanahan, D. & Weinberg, R. A. Hallmarks of Cancer: The Next Generation - PIIS0092867411001279.pdf. *Cell* **144**, 646–674 (2011).

2.   Chan, K. S., Koh, C. G. & Li, H. Y. Mitosis-targeted anti-cancer therapies: Where they stand. *Cell Death and Disease* vol. 3 e411 Preprint at https://doi.org/10.1038/cddis.2012.148 (2012).

3.   Hanahan, D. Hallmarks of Cancer: New Dimensions. *Cancer Discovery* vol. 12 31–46 Preprint at https://doi.org/10.1158/2159-8290.CD-21-1059 (2022).

4.   Brenner, D. R. *et al.* Projected estimates of cancer in Canada in 2020. *CMAJ* **192**, E199–E205 (2020).

5.   Scheidig, A. J., Burmester, C. & Goody, R. S. The pre-hydrolysis state of p21(ras) in complex with GTP: New insights into the role of water molecules in the GTP hydrolysis reaction of ras-like proteins. *Structure* **7**, 1311–1324 (1999).

6.   Serebriiskii, I. G. *et al.* Comprehensive characterization of RAS mutations in colon and rectal cancers in old and young patients. *Nat Commun* **10**, 3722 (2019).

7.   Allan, L. A. & Clarke, P. R. Phosphorylation of Caspase-9 by CDK1/Cyclin B1 Protects Mitotic Cells against Apoptosis. *Mol Cell* **26**, 301–310 (2007).

8.   Sansregret, L. & Swanton, C. The role of aneuploidy in cancer evolution. *Cold Spring Harbor Perspectives in Medicine* vol. 7 a028373 Preprint at https://doi.org/10.1101/cshperspect.a028373 (2017).

9.   Motazedian, A. & Dawson, M. A. MSL pushes genomic instability over the edge. *Nature Cell Biology* vol. 23 295–296 Preprint at https://doi.org/10.1038/s41556-021-00666-1 (2021).

10. de Gooijer, M. C. *et al.* The G2 checkpoint—a node-based molecular switch. *FEBS Open Bio* **7**, 439–455 (2017).

11.   Meadows, J. C. & Millar, J. B. A. Sharpening the anaphase switch. *Biochem Soc Trans* **43**, 19–22 (2015).

12.   Lara-Gonzalez, P., Westhorpe, F. G. & Taylor, S. S. The spindle assembly checkpoint. *Current Biology* **22**, 966–980 (2012).

13.   Vogt, E., Kirsch-Volders, M., Parry, J. & Eichenlaub-Ritter, U. Spindle formation, chromosome segregation and the spindle checkpoint in mammalian oocytes and susceptibility to meiotic error. *Mutat Res Genet Toxicol Environ Mutagen* **651**, 14–29 (2008).

14.   Shirayama, M., Tóth, A., Gálová, M. & Nasmyth, K. APC(Cdc20) promotes exit from mitosis by destroying the anaphase inhibitor Pds1 and cyclin Clb5. *Nature* **402**, 203–207 (1999).

15.   Maldonado, M. & Kapoor, T. M. Constitutive Mad1 targeting to kinetochores uncouples checkpoint signalling from chromosome biorientation. *Nat Cell Biol* **13**, 475–482 (2011).

16.   Li, R. & Murray, A. W. Feedback control of mitosis in budding yeast. *Cell* **66**, 519–531 (1991).

17.   Pines, J. Cubism and the cell cycle: The many faces of the APC/C. *Nature Reviews Molecular Cell Biology* vol. 12 427–438 Preprint at https://doi.org/10.1038/nrm3132 (2011).

18.   Petry, S. Mechanisms of Mitotic Spindle Assembly. *Annu Rev Biochem* **85**, 659–683 (2016).

19.   Goodson, H. v. & Jonasson, E. M. Microtubules and microtubule-associated proteins. *Cold Spring Harb Perspect Biol* **10**, a022608 (2018).

20.   Wordeman, L. GTP-tubulin loves microtubule plus ends but marries the minus ends. *Journal of Cell Biology* vol. 218 2822–2823 Preprint at https://doi.org/10.1083/jcb.201908039 (2019).

21. Brouhard, G. J. & Rice, L. M. Microtubule dynamics: An interplay of biochemistry and mechanics. *Nature Reviews Molecular Cell Biology* vol. 19 451–463 Preprint at https://doi.org/10.1038/s41580-018-0009-y (2018).

22. Smith, E. *et al.* Differential control of Eg5-dependent centrosome separation by Plk1 and Cdk1. *EMBO Journal* **30**, 2233–2245 (2011).

23. Tillery, M. M. L., Blake-Hedges, C., Zheng, Y., Buchwalter, R. A. & Megraw, T. L. Centrosomal and non-centrosomal microtubule-organizing centers (MTOCs) in Drosophila melanogaster. *Cells* vol. 7 121 Preprint at https://doi.org/10.3390/cells7090121 (2018).

24. Consolati, T. *et al.* Microtubule Nucleation Properties of Single Human γTuRCs Explained by Their Cryo-EM Structure. *Dev Cell* **53**, 603–617 (2020).

25. Moritz, M., Braunfeld, M. B., Sedat, J. W., Alberts, B. & Agard, D. A. Microtubule nucleation by γ-tubulin-containing rings in the centrosome. *Nature* **378**, 638–640 (1995).

26. Wieczorek, M., Bechstedt, S., Chaaban, S. & Brouhard, G. J. Microtubule-associated proteins control the kinetics of microtubule nucleation. *Nat Cell Biol* **17**, 907–916 (2015).

27. Barr, A. R. & Bakal, C. A sensitised RNAi screen reveals a ch-TOG genetic interaction network required for spindle assembly. *Sci Rep* **5**, 10564 (2015).

28. Byrnes, A. E. & Slep, K. C. TOG-tubulin binding specificity promotes microtubule dynamics and mitotic spindle formation. *Journal of Cell Biology* **216**, 1641–1657 (2017).

29. Roostalu, J., Cade, N. I. & Surrey, T. Complementary activities of TPX2 and chTOG constitute an efficient importin-regulated microtubule nucleation module. *Nat Cell Biol* **17**, 1422–1434 (2015).

30. Kalab, P., Weis, K. & Heald, R. Visualization of a Ran-GTP gradient in interphase and mitotic Xenopus egg extracts. *Science (1979)* **295**, 2452–2456 (2002).

31. Xu, L. & Massagué, J. Nucleocytoplasmic shuttling of signal transducers. *Nature Reviews Molecular Cell Biology* vol. 5 209–219 Preprint at https://doi.org/10.1038/nrm1331 (2004).

32.   Kaláb, P., Pralle, A., Isacoff, E. Y., Heald, R. & Weis, K. Analysis of a RanGTP-regulated gradient in mitotic somatic cells. *Nature* **440**, 697–701 (2006).

33.   Gruss, O. J. *et al.* Ran induces spindle assembly by reversing the inhibitory effect of importin α on TPX2 activity. *Cell* **104**, 83–93 (2001).

34.   Wordeman, L. & Mitchison, T. J. Identification and partial characterization of mitotic centromere- associated kinesin, a kinesin-related protein that associates with centromeres during mitosis. *Journal of Cell Biology* **128**, 95–104 (1995).

35.   Barr, A. R. & Gergely, F. MCAK-Independent Functions of ch-Tog/XMAP215 in Microtubule Plus-End Dynamics. *Mol Cell Biol* **28**, 7199–7211 (2008).

36.   Dumontet, C. & Jordan, M. A. Microtubule-binding agents: A dynamic field of cancer therapeutics. *Nature Reviews Drug Discovery* vol. 9 790–803 Preprint at https://doi.org/10.1038/nrd3253 (2010).

37.   Yu, J. X., Chen, Q., Yu, Y. Q., Li, S. Q. & Song, J. F. Upregulation of colonic and hepatic tumor overexpressed gene is significantly associated with the unfavorable prognosis marker of human hepatocellular carcinoma. *Am J Cancer Res* **6**, 690–700 (2016).

38.   Weaver, B. A. How Taxol/paclitaxel kills cancer cells. *Molecular Biology of the Cell* vol. 25 2677–2681 Preprint at https://doi.org/10.1091/mbc.E14-04-0916 (2014).

39.   Snyder, J. P., Nettles, J. H., Cornett, B., Downing, K. H. & Nogales, E. The binding conformation of Taxol in-tubulin: A model based on electron crystallographic density. *Proc Natl Acad Sci U S A* **98**, 5312–5316 (2001).

40.   Parness, J. & Horwitz, S. B. Taxol binds to polymerized tubulin in vitro. *Journal of Cell Biology* **91**, 479–487 (1981).

41.   Liebmann, J. E. *et al.* Cytotoxic studies of pacfitaxel (Taxol®) in human tumour cell lines. *Br J Cancer* **68**, 1104–1109 (1993).

42.   Adams, J. D. *et al.* Taxol: a history of pharmaceutical development and current pharmaceutical concerns. *Journal of the National Cancer Institute. Monographs* 141–147 Preprint at (1993).

43.   Zasadil, L. M. *et al.* Cytotoxicity of paclitaxel in breast cancer is due to chromosome missegregation on multipolar spindles. *Sci Transl Med* **6**, 229ra43 (2014).

44.   Kavallaris, M. Microtubules and resistance to tubulin-binding agents. *Nature Reviews Cancer* vol. 10 194–204 Preprint at https://doi.org/10.1038/nrc2803 (2010).

45.   Xie, S. & Zhou, J. Harnessing plant biodiversity for the discovery of novel anticancer drugs targeting microtubules. *Frontiers in Plant Science* vol. 8 720 Preprint at https://doi.org/10.3389/fpls.2017.00720 (2017).

46.   Xiao, H., Zheng, Y., Ma, L., Tian, L. & Sun, Q. Clinically-Relevant ABC Transporter for Anti-Cancer Drug Resistance. *Frontiers in Pharmacology* vol. 12 648407 Preprint at https://doi.org/10.3389/fphar.2021.648407 (2021).

47.   Gonçalves, A. *et al.* Resistance to taxol in lung cancer cells associated with increased microtubule dynamics. *Proc Natl Acad Sci U S A* **98**, 11732–11742 (2001).

48.   Kamath, K., Wilson, L., Cabral, F. & Jordan, M. A. βIII-tubulin induces paclitaxel resistance in association with reduced effects on microtubule dynamic instability. *Journal of Biological Chemistry* **280**, 12902–12907 (2005).

49.   Sato, T. *et al.* Binding affinities of paclitaxel and docetaxel for generic and nanoparticle albumin-bound paclitaxel-derived albumin from human serum. *Biomed Rep* **14**, 1733 (2021).

50.   Jordan, M. & Kamath, K. How Do Microtubule-Targeted Drugs Work? An Overview. *Curr Cancer Drug Targets* **7**, 730–742 (2007).

51.   Gigant, B. *et al.* Structural basis for the regulation of tubulin by vinblastine. *Nature* **435**, 519–522 (2005).

52.   Prota, A. E. *et al.* A new tubulin-binding site and pharmacophore for microtubule-destabilizing anticancer drugs. *Proc Natl Acad Sci U S A* **111**, 13817–13821 (2014).

53.   Leung, Y. Y., Yao Hui, L. L. & Kraus, V. B. Colchicine-Update on mechanisms of action and therapeutic uses. *Seminars in Arthritis and Rheumatism* vol. 45 341–350 Preprint at https://doi.org/10.1016/j.semarthrit.2015.06.013 (2015).

54. Garland, D. L. Kinetics and Mechanism of Colchicine Binding to Tubulin: Evidence for Ligand-Induced Conformational Change. *Biochemistry* **17**, 4266–4272 (1978).

55. Massarotti, A., Coluccia, A., Silvestri, R., Sorba, G. & Brancale, A. The tubulin colchicine domain: A molecular modeling perspective. *ChemMedChem* vol. 7 33–42 Preprint at https://doi.org/10.1002/cmdc.201100361 (2012).

56. Bhattacharyya, B., Panda, D., Gupta, S. & Banerjee, M. Anti-mitotic activity of colchicine and the structural basis for its interaction with tubulin. *Medicinal Research Reviews* vol. 28 155–183 Preprint at https://doi.org/10.1002/med.20097 (2008).

57. Fltzgerald, T. J. Molecular features of colchicine associated with antimitotic activity and inhibition of tubulin polymerization. *Biochem Pharmacol* **25**, 1383–1387 (1976).

58. Signoretto, E. *et al.* Nocodazole Induced Suicidal Death of Human Erythrocytes. *Cellular Physiology and Biochemistry* **38**, 379–392 (2016).

59. Wang, Y. *et al.* Structures of a diverse set of colchicine binding site inhibitors in complex with tubulin provide a rationale for drug discovery. *FEBS Journal* **283**, 102–111 (2016).

60. Godinho, S. A. & Pellman, D. Causes and consequences of centrosome abnormalities in cancer. *Philosophical Transactions of the Royal Society B: Biological Sciences* vol. 369 20130467 Preprint at https://doi.org/10.1098/rstb.2013.0467 (2014).

61. Ogden, A., Rida, P. C. G. & Aneja, R. Let's huddle to prevent a muddle: Centrosome declustering as an attractive anticancer strategy. *Cell Death and Differentiation* vol. 19 1255–1267 Preprint at https://doi.org/10.1038/cdd.2012.61 (2012).

62. Pannu, V. *et al.* HSET overexpression fuels tumor progression via centrosome clustering-independent mechanisms in breast cancer patients. *Oncotarget* **6**, 6076–6091 (2015).

63. Zeligs, J. D. & Wollman, S. H. Mitosis in rat thyroid epithelial cells in vivo. II. Centrioles and pericentriolar material. *Journal of Ultrasructure Research* **66**, 97–108 (1979).

64. Buendia, B., Bré, M. H., Griffiths, G. & Karsenti, E. Cytoskeletal control of centrioles movement during the establishment of polarity in Madin-Darby Canine kidney cells. *Journal of Cell Biology* **110**, 1123–1135 (1990).

65. Milunović-Jevtić, A., Mooney, P., Sulerud, T., Bisht, J. & Gatlin, J. C. Centrosomal clustering contributes to chromosomal instability and cancer. *Current Opinion in Biotechnology* vol. 40 113–118 Preprint at https://doi.org/10.1016/j.copbio.2016.03.011 (2016).

66. Sekino, Y. *et al.* KIFC1 Inhibitor CW069 induces apoptosis and reverses resistance to docetaxel in prostate cancer. *J Clin Med* **8**, 225 (2019).

67. Tuan, N. M. & Lee, C. H. Role of anillin in tumour: From a prognostic biomarker to a novel target. *Cancers* vol. 12 1–27 Preprint at https://doi.org/10.3390/cancers12061600 (2020).

68. Wang, D., Naydenov, N. G., Dozmorov, M. G., Koblinski, J. E. & Ivanov, A. I. Anillin regulates breast cancer cell migration, growth, and metastasis by non-canonical mechanisms involving control of cell stemness and differentiation. *Breast Cancer Research* **22**, (2020).

69. Green, R. A., Paluch, E. & Oegema, K. Cytokinesis in animal cells. *Annual Review of Cell and Developmental Biology* vol. 28 101011–155718 Preprint at https://doi.org/10.1146/annurev-cellbio-101011-155718 (2012).

70. Zanin, E. *et al.* A conserved RhoGAP limits M phase contractility and coordinates with microtubule asters to confine RhoA during Cytokinesis. *Dev Cell* **26**, 496–510 (2013).

71. Piekny, A., Werner, M. & Glotzer, M. Cytokinesis: Welcome to the Rho zone. *Trends in Cell Biology* vol. 15 651–658 Preprint at https://doi.org/10.1016/j.tcb.2005.10.006 (2005).

72. Piekny, A. J. & Maddox, A. S. The myriad roles of Anillin during cytokinesis. *Seminars in Cell and Developmental Biology* vol. 21 881–891 Preprint at https://doi.org/10.1016/j.semcdb.2010.08.002 (2010).

73. Ozugergin, I. & Piekny, A. Diversity is the spice of life: An overview of how cytokinesis regulation varies with cell type. *Front Cell Dev Biol* **10**, (2022).

74. Husser, M. C., Skaik, N., Martin, V. J. J. & Piekny, A. CRISPR-Cas tools to study gene function in cytokinesis. *J Cell Sci* **134**, jcs254409 (2021).

75. Piekny, A. J. & Glotzer, M. Anillin Is a Scaffold Protein That Links RhoA, Actin, and Myosin during Cytokinesis. *Current Biology* **18**, 30–36 (2008).

76. Hickson, G. R. X. & O'Farrell, P. H. Rho-dependent control of anillin behavior during cytokinesis. *Journal of Cell Biology* **180**, 285–294 (2008).

77. Maddox, A. S., Lewellyn, L., Desai, A. & Oegema, K. Anillin and the Septins Promote Asymmetric Ingression of the Cytokinetic Furrow. *Dev Cell* **12**, 827–835 (2007).

78. Fotopoulos, N. *et al.* Caenorhabditis elegans anillin (ani-1) regulates neuroblast cytokinesis and epidermal morphogenesis during embryonic development. *Dev Biol* **383**, 61–74 (2013).

79. Ozugergin, I., Mastronardi, K., Law, C. & Piekny, A. Diverse mechanisms regulate contractile ring assembly for cytokinesis in the two-cell Caenorhabditis elegans embryo. *J Cell Sci* **135**, jcs258921 (2022).

80. Husser, M. C., Ozugergin, I., Resta, T., Martin, V. J. J. & Piekny, A. J. Cytokinetic diversity in mammalian cells is revealed by the characterization of endogenous anillin, Ect2 and RhoA. *Open Biol* **12**, (2022).

81. Tse, Y. C., Piekny, A. & Glotzera, M. Anillin promotes astral microtubule-directed cortical myosin polarization. *Mol Biol Cell* **22**, 3165–3175 (2011).

82. Triplet, C. van O., Garcia, M. J., Bik, H. H., Beaudet, D. & Piekny, A. Anillin interacts with microtubules and is part of the astral pathway that defines cortical domains. *J Cell Sci* **127**, 3699–3710 (2014).

83. Chen, A. *et al.* Inhibition of polar actin assembly by astral microtubules is required for cytokinesis. *Nat Commun* **12**, 2409 (2021).

84. Mangal, S. *et al.* TPXL-1 activates Aurora A to clear contractile ring components from the polar cortex during cytokinesis. *Journal of Cell Biology* **217**, 837–848 (2018).

85. Yamamoto, K. *et al.* Optogenetic relaxation of actomyosin contractility uncovers mechanistic roles of cortical tension during cytokinesis. *Nat Commun* **12**, 7145 (2021).

86. Mishima, M., Kaitna, S. & Glotzer, M. Central spindle assembly and cytokinesis require a kinesin-like protein/RhoGAP complex with microtubule bundling activity. *Dev Cell* **2**, 41–54 (2002).

87. Yüce, Ö., Piekny, A. & Glotzer, M. An ECT2-centralspindlin complex regulates the localization and function of RhoA. *Journal of Cell Biology* **170**, 571–582 (2005).

88. Saito, S. *et al.* Deregulation and Mislocalization of the Cytokinesis Regulator ECT2 Activate the Rho Signaling Pathways Leading to Malignant Transformation. *Journal of Biological Chemistry* **279**, 7169–7179 (2004).

89. Beaudet, D. A Chromatin-Sensing Pathway Regulates Cytokinesis. (Concordia University, 2019).

90. Petronczki, M., Glotzer, M., Kraut, N. & Peters, J. M. Polo-like Kinase 1 Triggers the Initiation of Cytokinesis in Human Cells by Promoting Recruitment of the RhoGEF Ect2 to the Central Spindle. *Dev Cell* **12**, 713–725 (2007).

91. Su, K. C., Takaki, T. & Petronczki, M. Targeting of the RhoGEF Ect2 to the Equatorial Membrane Controls Cleavage Furrow Formation during Cytokinesis. *Dev Cell* **21**, 1104–1115 (2011).

92. Frenette, P. *et al.* An anillin-ect2 complex stabilizes central spindle microtubules at the cortex during cytokinesis. *PLoS One* **7**, e34888 (2012).

93. Kotýnková, K., Su, K. C., West, S. C. & Petronczki, M. Plasma Membrane Association but Not Midzone Recruitment of RhoGEF ECT2 Is Essential for Cytokinesis. *Cell Rep* **17**, 2672–2686 (2016).

94. Li, J., Dallmayer, M., Kirchner, T., Musa, J. & Grünewald, T. G. P. PRC1: Linking Cytokinesis, Chromosomal Instability, and Cancer Evolution. *Trends in Cancer* vol. 4 59–73 Preprint at https://doi.org/10.1016/j.trecan.2017.11.002 (2018).

95. Adriaans, I. E., Basant, A., Ponsioen, B., Glotzer, M. & Lens, S. M. A. PLK1 plays dual roles in centralspindlin regulation during cytokinesis. *Journal of Cell Biology* **218**, 1250–1264 (2019).

96. Douglas, M. E., Davies, T., Joseph, N. & Mishima, M. Aurora B and 14-3-3 Coordinately Regulate Clustering of Centralspindlin during Cytokinesis. *Current Biology* **20**, 927–933 (2010).

97. Kunda, P. *et al.* PP1-mediated moesin dephosphorylation couples polar relaxation to mitotic exit. *Current Biology* **22**, 231–236 (2012).

98. Rodrigues, N. T. L. *et al.* Kinetochore-localized PP1-Sds22 couples chromosome segregation to polar relaxation. *Nature* **524**, 489–492 (2015).

99. Peterman, E., Valius, M. & Prekeris, R. CLIC4 is a cytokinetic cleavage furrow protein that regulates cortical cytoskeleton stability during cell division. *J Cell Sci* **133**, jcs241117 (2020).

100. Deng, M., Suraneni, P., Schultz, R. M. & Li, R. The Ran GTPase Mediates Chromatin Signaling to Control Cortical Polarity during Polar Body Extrusion in Mouse Oocytes. *Dev Cell* **12**, 301–308 (2007).

101. Beaudet, D., Akhshi, T., Phillipp, J., Law, C. & Piekny, A. Active Ran regulates anillin function during cytokinesis. *Mol Biol Cell* **28**, 3517–3531 (2017).

102. Beaudet, D., Pham, N., Skaik, N. & Piekny, A. Importin binding mediates the intramolecular regulation of anillin during cytokinesis. *Mol Biol Cell* **31**, 1103–1199 (2020).

103. Ozugergin, I. & Piekny, A. Complementary functions for the Ran gradient during division. *Small GTPases* vol. 12 177–187 Preprint at https://doi.org/10.1080/21541248.2020.1725371 (2021).

104. Chen, C. T., Hehnly, H. & Doxsey, S. J. Orchestrating vesicle transport, ESCRTs and kinase surveillance during abscission. *Nature Reviews Molecular Cell Biology* vol. 13 483–488 Preprint at https://doi.org/10.1038/nrm3395 (2012).

105. El-Amine, N., Carim, S. C., Wernike, D. & Hickson, G. R. X. Rho-dependent control of the Citron kinase, Sticky, drives midbody ring maturation. *Mol Biol Cell* **30**, 2185–2204 (2019).

106. Amine, N. el, Kechad, A., Jananji, S. & Hickson, G. R. X. Opposing actions of septins and Sticky on Anillin promote the transition from contractile to midbody ring. *Journal of Cell Biology* **203**, 487–504 (2013).

107. D'Avino, P. P. Citron kinase - renaissance of a neglected mitotic kinase. *Journal of Cell Science* vol. 130 1701–1708 Preprint at https://doi.org/10.1242/jcs.200253 (2017).

108. Echard, A., Hickson, G. R. X., Foley, E. & O'Farrell, P. H. Terminal cytokinesis events uncovered after an RNAi screen. *Current Biology* **14**, 1685–1693 (2004).

109. Gai, M. *et al.* Citron kinase controls abscission through RhoA and anillin. *Mol Biol Cell* **22**, 3768–3778 (2011).

110. Glotzer, M. The 3Ms of central spindle assembly: Microtubules, motors and MAPs. *Nature Reviews Molecular Cell Biology* vol. 10 9–20 Preprint at https://doi.org/10.1038/nrm2609 (2009).

111. Guizetti, J. *et al.* Cortical constriction during abscission involves helices of ESCRT-III-dependent filaments. *Science (1979)* **331**, 1616–1620 (2011).

112. Hu, C. K., Coughlin, M. & Mitchison, T. J. Midbody assembly and its regulation during cytokinesis. *Mol Biol Cell* **23**, 1024–1034 (2012).

113. Frémont, S. & Echard, A. Membrane Traffic in the Late Steps of Cytokinesis. *Current Biology* vol. 28 R458–R470 Preprint at https://doi.org/10.1016/j.cub.2018.01.019 (2018).

114. Simon, G. C. & Prekeris, R. The role of FIP3-dependent endosome transport during cytokinesis. *Commun Integr Biol* **1**, 132–133 (2008).

115. Stoten, C. L. & Carlton, J. G. ESCRT-dependent control of membrane remodelling during cell division. *Seminars in Cell and Developmental Biology* vol. 74 50–65 Preprint at https://doi.org/10.1016/j.semcdb.2017.08.035 (2018).

116. Schiel, J. A. *et al.* Endocytic membrane fusion and buckling-induced microtubule severing mediate cell abscission. *J Cell Sci* **124**, 1411–1424 (2011).

117. Basant, A. & Glotzer, M. Spatiotemporal Regulation of RhoA during Cytokinesis. *Current Biology* vol. 28 570–580 Preprint at https://doi.org/10.1016/j.cub.2018.03.045 (2018).

118. Zhao, W. M. & Fang, G. MgcRacGAP controls the assembly of the contractile ring and the initiation of cytokinesis. *Proc Natl Acad Sci U S A* **102**, 13158–13163 (2005).

119. Osório, D. S. *et al.* Crosslinking activity of non-muscle myosin II is not sufficient for embryonic cytokinesis in C. elegans. *Development* **146**, dev179150 (2019).

120. Bell, K. R. *et al.* Novel cytokinetic ring components drive negative feedback in cortical contractility. *Mol Biol Cell* **31**, 1623–1636 (2020).

121. Kechad, A., Jananji, S., Ruella, Y. & Hickson, G. R. X. Anillin acts as a bifunctional linker coordinating midbody ring biogenesis during cytokinesis. *Current Biology* **22**, 197–203 (2012).

122. Carim, S. C., Kechad, A. & Hickson, G. R. X. Animal Cell Cytokinesis: The Rho-Dependent Actomyosin-Anilloseptin Contractile Ring as a Membrane Microdomain Gathering, Compressing, and Sorting Machine. *Front Cell Dev Biol* **8**, (2020).

123. Bassi, Z. I. *et al.* Sticky/Citron kinase maintains proper RhoA localization at the cleavage site during cytokinesis. *Journal of Cell Biology* **195**, 595–603 (2011).

124. Panagiotou, T. C., Chen, A. & Wilde, A. An anillin-CIN85-SEPT9 complex promotes intercellular bridge maturation required for successful cytokinesis. *Cell Rep* **40**, (2022).

125. Renshaw, M. J., Liu, J., Lavoie, B. D. & Wilde, A. Anillin-dependent organization of septin filaments promotes intercellular bridge elongation and Chmp4B targeting to the abscission site. *Open Biol* **4**, 130190 (2014).

126. Lekomtsev, S. *et al.* Centralspindlin links the mitotic spindle to the plasma membrane during cytokinesis. *Nature* **492**, 276–279 (2012).

127. Wolfe, B. A., Takaki, T., Petronczki, M. & Glotzer, M. Polo-like kinase 1 directs assembly of the HsCyk-4 RhoGAP/Ect2 RhoGEF complex to initiate cleavage furrow formation. *PLoS Biol* **7**, e1000110 (2009).

128. Pearson, M. A., Reczek, D., Bretscher, A. & Karplus, P. A. Structure of the ERM protein moesin reveals the FERM domain fold masked by an extended actin binding tail domain. *Cell* **101**, 259–270 (2000).

129. Yang, G. *et al.* Molecular basis of functional exchangeability between ezrin and other actin-membrane associated proteins during cytokinesis. *Exp Cell Res* **403**, 112600 (2021).

130. Kalab, P. & Heald, R. The RanGTP gradient - A GPS for the mitotic spindle. *J Cell Sci* **121**, 1577–1586 (2008).

131. Forbes, D. J., Travesa, A., Nord, M. S. & Bernis, C. Nuclear transport factors: Global regulation of mitosis. *Current Opinion in Cell Biology* vol. 35 78–90 Preprint at https://doi.org/10.1016/j.ceb.2015.04.012 (2015).

132. Hasegawa, K., Ryu, S. J. & Kaláb, P. Chromosomal gain promotes formation of a steep RanGTP gradient that drives mitosis in aneuploid cells. *Journal of Cell Biology* **200**, 151–161 (2013).

133. Tripathi, V. K., Subramaniyan, S. A. & Hwang, I. Molecular and Cellular Response of Co-cultured Cells toward Cobalt Chloride (CoCl2)-Induced Hypoxia. *ACS Omega* **4**, 20882–20893 (2019).

134. de Boeck, M., Kirsch-Volders, M. & Lison, D. Cobalt and antimony: Genotoxicity and carcinogenicity. *Mutation Research - Fundamental and Molecular Mechanisms of Mutagenesis* vol. 533 135–152 Preprint at https://doi.org/10.1016/j.mrfmmm.2003.07.012 (2003).

135. Lopez-Sánchez, L. M. *et al.* CoCl2, a mimic of hypoxia, induces formation of polyploid giant cells with stem characteristics in colon cancer. *PLoS One* **9**, e99143 (2014).

136. Drost, J. *et al.* Sequential cancer mutations in cultured human intestinal stem cells. *Nature* **521**, 43–47 (2015).

137. Ran, F. A. *et al.* Genome engineering using the CRISPR-Cas9 system. *Nat Protoc* **8**, 2281–2308 (2013).

138. Kato-Inui, T., Takahashi, G., Hsu, S. & Miyaoka, Y. Clustered regularly interspaced short palindromic repeats (CRISPR)/CRISPR-associated protein 9 with improved proof-reading enhances homology-directed repair. *Nucleic Acids Res* **46**, 4677–4688 (2018).

139. Budnar, S. *et al.* Anillin Promotes Cell Contractility by Cyclic Resetting of RhoA Residence Kinetics. *Dev Cell* **49**, 894–906 (2019).

140. Mastop, M. *et al.* Characterization of a spectrally diverse set of fluorescent proteins as FRET acceptors for mTurquoise2. *Sci Rep* **7**, 11999 (2017).

141. Lee, M. E., DeLoache, W. C., Cervantes, B. & Dueber, J. E. A Highly Characterized Yeast Toolkit for Modular, Multipart Assembly. *ACS Synth Biol* **4**, 975–986 (2015).

142. Narkar, A. *et al.* On the role of p53 in the cellular response to aneuploidy. *Cell Rep* **34**, 108892 (2021).

143. Canman, J. C. *et al.* Determining the position of the cell division plane. *Nature* **424**, 1074–1078 (2003).

144. Carvalho, A., Desai, A. & Oegema, K. Structural Memory in the Contractile Ring Makes the Duration of Cytokinesis Independent of Cell Size. *Cell* **137**, 926–937 (2009).

145. Carreno, S. *et al.* Moesin and its activating kinase Slik are required for cortical stability and microtubule organization in mitotic cells. *Journal of Cell Biology* **180**, 739–746 (2008).

146. Musacchio, A. The Molecular Biology of Spindle Assembly Checkpoint Signaling Dynamics. *Current Biology* vol. 25 R1002–R1008 Preprint at https://doi.org/10.1016/j.cub.2015.08.051 (2015).

147. Hari, M. *et al.* Paclitaxel-resistant cells have a mutation in the paclitaxel-binding region of β-tubulin (Asp26Glu) and less stable microtubules. *Mol Cancer Ther* **5**, 270–278 (2006).

148. Hughes, J. P., Rees, S. S., Kalindjian, S. B. & Philpott, K. L. Principles of early drug discovery. *Br J Pharmacol* **162**, 1239–1249 (2011).

149. Bhattacharyya, B. & Wolff, J. Promotion of fluorescence upon binding of colchicine to tubulin. *Proc Natl Acad Sci U S A* **71**, (1974).

150. Friedrich, J., Seidel, C., Ebner, R. & Kunz-Schughart, L. A. Spheroid-based drug screen: Considerations and practical approach. *Nat Protoc* **4**, 309–324 (2009).

151. Sutherland, R. M. Cell and environment interactions in tumor microregions: The multicell spheroid model. *Science* vol. 240 177–184 Preprint at https://doi.org/10.1126/science.2451290 (1988).

152. Kirschner, M. W. & Williams, R. C. The mechanism of microtubule assembly in vitro. *J Supramol Struct* **2**, 412–428 (1974).

153. Margolis, R. L. & Wilson, L. Addition of colchicine tubulin complex to microtubule ends: The mechanism of substoichiometric colchicine poisoning. *Proc Natl Acad Sci U S A* **74**, 3466–3470 (1977).

154. Holmfeldt, P., Stenmark, S. & Gullberg, M. Differential functional interplay of TOGp/XMAP215 and the KinI kinesin MCAK during interphase and mitosis. *EMBO Journal* **23**, 627–637 (2004).

155. Hood, F. E. *et al.* Coordination of adjacent domains mediates TACC3-ch-TOG-clathrin assembly and mitotic spindle binding. *Journal of Cell Biology* **202**, 463–478 (2013).

156. Chen, F., Wong, N. W. Y. & Forgione, P. One-pot tandem palladium-catalyzed decarboxylative cross-coupling and C-H activation route to thienoisoquinolines. *Adv Synth Catal* **356**, 1725–1730 (2014).

157. Shi, J. & Mitchison, T. J. Cell death response to anti-mitotic drug treatment in cell culture, mouse tumor model and the clinic. *Endocrine-related cancer* vol. 24 T83 Preprint at https://doi.org/10.1530/ERC-17-0003 (2017).

158. Martin, M. & Akhmanova, A. Coming into Focus: Mechanisms of Microtubule Minus-End Organization. *Trends in Cell Biology* vol. 28 574–588 Preprint at https://doi.org/10.1016/j.tcb.2018.02.011 (2018).

159. Oakley, B. R., Paolillo, V. & Zheng, Y. γ-tubulin complexes in microtubule nucleation and beyond. *Mol Biol Cell* **26**, 2957–2962 (2015).

160. Akhmanova, A. & Steinmetz, M. O. Control of microtubule organization and dynamics: Two ends in the limelight. *Nature Reviews Molecular Cell Biology* vol. 16 711–726 Preprint at https://doi.org/10.1038/nrm4084 (2015).

161. Brouhard, G. J. *et al.* XMAP215 Is a Processive Microtubule Polymerase. *Cell* **132**, 79–88 (2008).

162. Gergely, F., Draviam, V. M. & Raff, J. W. The ch-TOG/XMAP215 protein is essential for spindle pole organization in human somatic cells. *Genes Dev* **17**, 336–341 (2003).

163. Zhang, X., Ems-McClung, S. C. & Walczak, C. E. Aurora A phosphorylates MCAK to control ran-dependent spindle bipolarity. *Mol Biol Cell* **19**, 2752–2765 (2008).

164. Walczak, C. E., Gayek, S. & Ohi, R. Microtubule-depolymerizing kinesins. *Annual Review of Cell and Developmental Biology* vol. 29 417–441 Preprint at https://doi.org/10.1146/annurev-cellbio-101512-122345 (2013).

165. Widlund, P. O. *et al.* XMAP215 polymerase activity is built by combining multiple tubulin-binding TOG domains and a basic lattice-binding region. *Proc Natl Acad Sci U S A* **108**, 2741–2746 (2011).

166. Dominguez-Brauer, C. *et al.* Targeting Mitosis in Cancer: Emerging Strategies. *Molecular Cell* vol. 60 524–536 Preprint at https://doi.org/10.1016/j.molcel.2015.11.006 (2015).

167. Kumar, N. Taxol-induced polymerization of purified tubulin. Mechanism of action. *Journal of Biological Chemistry* **256**, 10435–10441 (1981).

168. Kumar, A., Sharma, P. R. & Mondhe, D. M. Potential anticancer role of colchicine-based derivatives: An overview. *Anti-Cancer Drugs* vol. 28 250–262 Preprint at https://doi.org/10.1097/CAD.0000000000000464 (2016).

169. Field, J. J., Kanakkanthara, A. & Miller, J. H. Microtubule-targeting agents are clinically successful due to both mitotic and interphase impairment of microtubule function. *Bioorganic and Medicinal Chemistry* vol. 22 5050–5059 Preprint at https://doi.org/10.1016/j.bmc.2014.02.035 (2015).

170. Martino, E. *et al.* Vinca alkaloids and analogues as anti-cancer agents: Looking back, peering ahead. *Bioorganic and Medicinal Chemistry Letters* vol. 28 2816–2826 Preprint at https://doi.org/10.1016/j.bmcl.2018.06.044 (2018).

171. Panda, D., Miller, H. P., Islam, K. & Wilson, L. Stabilization of microtubule dynamics by estramustine by binding to a novel site in tubulin: A possible mechanistic basis for its antitumor action. *Proc Natl Acad Sci U S A* **94**, 10560–10564 (1997).

172. Jordan, M. A., Thrower, D. & Wilson, L. Effects of vinblastine, podophyllotoxin and nocodazole on mitotic spindles. Implications for the role of microtubule dynamics in mitosis. *J Cell Sci* **102**, 401–416 (1992).

173. Wendell, K. L., Wilson, L. & Jordan, M. A. Mitotic block in HeLa cells by vinblastine: Ultrastructural changes in kinetochore-mcirotubule attachment and in centrosomes. *J Cell Sci* **104**, 261–274 (1993).

174. Brito, D. A. & Rieder, C. L. The ability to survive mitosis in the presence of microtubule poisons differs significantly between human nontransformed (RPE-1) and cancer (U2OS, HeLa) cells. *Cell Motil Cytoskeleton* **66**, 437–447 (2009).

175. Hedrick, D. G., Stout, J. R. & Walczak, C. E. Effects of anti-microtubule agents on microtubule organization in cells lacking the kinesin-13 MCAK. *Cell Cycle* **7**, 2146–2156 (2008).

176. Ertych, N. *et al.* Increased microtubule assembly rates influence chromosomal instability in colorectal cancer cells. *Nat Cell Biol* **16**, 779–791 (2014).

177. Yu, N. *et al.* Isolation of Functional Tubulin Dimers and of Tubulin-Associated Proteins from Mammalian Cells. *Current Biology* **26**, 1728–1736 (2016).

178. Fielding, A. B., Lim, S., Montgomery, K., Dobreva, I. & Dedhar, S. A critical role of integrin-linked kinase, ch-TOG and TACC3 in centrosome clustering in cancer cells. *Oncogene* **30**, 521–534 (2011).

179. Al-Bassam, J. & Chang, F. Regulation of microtubule dynamics by TOG-domain proteins XMAP215/Dis1 and CLASP. *Trends in Cell Biology* vol. 21 604–614 Preprint at https://doi.org/10.1016/j.tcb.2011.06.007 (2011).

180. Liu, J. T. *et al.* Design, structure-activity relationship study and biological evaluation of the thieno[3,2-c]isoquinoline scaffold as a potential anti-cancer agent. *Bioorg Med Chem Lett* **52**, 128327 (2021).

181. Chou, T. C. Drug combination studies and their synergy quantification using the chou-talalay method. *Cancer Research* vol. 70 440–446 Preprint at https://doi.org/10.1158/0008-5472.CAN-09-1947 (2010).

182. Andrews, P. D. *et al.* Aurora B regulates MCAK at the mitotic centromere. *Dev Cell* **6**, 253–268 (2004).

183. Ems-Mcclung, S. C. *et al.* Aurora B inhibits MCAK activity through a phosphoconformational switch that reduces microtubule association. *Current Biology* **23**, 2491–2499 (2013).

184. Levrier, C. *et al.* 6α-Acetoxyanopterine: A novel structure class of mitotic inhibitor disrupting microtubule dynamics in prostate cancer cells. *Mol Cancer Ther* **16**, 3–15 (2017).

185. Karki, M., Keyhaninejad, N. & Shuster, C. B. Precocious centriole disengagement and centrosome fragmentation induced by mitotic delay. *Nat Commun* **8**, 1–2 (2017).

186. Foraker, A. B. *et al.* Clathrin promotes centrosome integrity in early mitosis through stabilization of centrosomal ch-TOG. *Journal of Cell Biology* **198**, 591–605 (2012).

187. Rai, A., Surolia, A. & Panda, D. An Antitubulin Agent BCFMT Inhibits Proliferation of Cancer Cells and Induces Cell Death by Inhibiting Microtubule Dynamics. *PLoS One* **7**, e44311 (2012).

188. Sabat-Pospiech, D., Fabian-Kolpanowicz, K., Prior, I. A., Coulson, J. M. & Fielding, A. B. Targeting centrosome amplification, an Achilles' heel of cancer. *Biochemical Society Transactions* vol. 47 1209–1222 Preprint at https://doi.org/10.1042/BST20190034 (2019).

189. Leber, B. *et al.* Proteins required for centrosome clustering in cancer cells. *Sci Transl Med* **2**, 33ra38 (2010).

190. McKenzie, C. & D'Avino, P. P. Investigating cytokinesis failure as a strategy in cancer therapy. *Oncotarget* **7**, 87323–87341 (2016).

191.	Margall-Ducos, G., Celton-Morizur, S., Couton, D., Brégerie, O. & Desdouets, C. Liver tetraploidization is controlled by a new process of incomplete cytokinesis. *J Cell Sci* **120**, 3633–3639 (2007).

192.	Miettinen, T. P. *et al.* Identification of transcriptional and metabolic programs related to mammalian cell size. *Current Biology* **24**, 598–608 (2014).

193.	Øvrebø, J. I. & Edgar, B. A. Polyploidy in tissue homeostasis and regeneration. *Development (Cambridge)* vol. 145 dev156034 Preprint at https://doi.org/10.1242/dev.156034 (2018).

194.	Cao, J. *et al.* Tension Creates an Endoreplication Wavefront that Leads Regeneration of Epicardial Tissue. *Dev Cell* **42**, 600–615 (2017).

195.	Zhang, S. *et al.* Knockdown of Anillin Actin Binding Protein Blocks Cytokinesis in Hepatocytes and Reduces Liver Tumor Development in Mice Without Affecting Regeneration. *Gastroenterology* **154**, 1421–1434 (2018).

196.	Donne, R., Saroul-Aïnama, M., Cordier, P., Celton-Morizur, S. & Desdouets, C. Polyploidy in liver development, homeostasis and disease. *Nature Reviews Gastroenterology and Hepatology* vol. 17 391–405 Preprint at https://doi.org/10.1038/s41575-020-0284-x (2020).

197.	Bou-Nader, M. *et al.* Polyploidy spectrum: A new marker in HCC classification. *Gut* **69**, 355–364 (2020).

198.	Dhamodharan, R., Jordan, M. A., Thrower, D., Wilson, L. & Wadsworth, P. Vinblastine suppresses dynamics of individual microtubules in living interphase cells. *Mol Biol Cell* **6**, 1215–1229 (1995).

199.	Panda, D., Jordan, M. A., Chu, K. C. & Wilson, L. Differential effects of vinblastine on polymerization and dynamics at opposite microtubule ends. *Journal of Biological Chemistry* **271**, 29807–29812 (1996).

200.	Martin, G. M. & Sprague, C. A. Vinblastine induces multipolar mitoses in tetraploid human cells. *Exp Cell Res* **63**, 466–467 (1970).
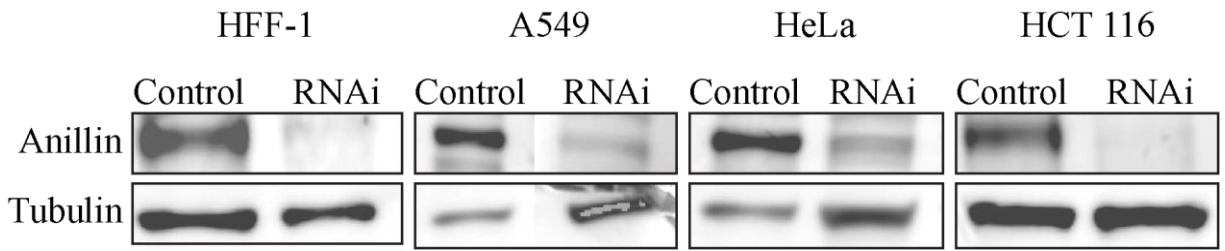
Supplemental Figures

Figure S1: The efficacy of anillin depletion in different cell lines. Western blots show the levels of anillin in lysates from control HFF-1, A549, HeLa and HCT116 cells and after anillin RNAi treatment. Tubulin detected using DM1a was used as a loading control.
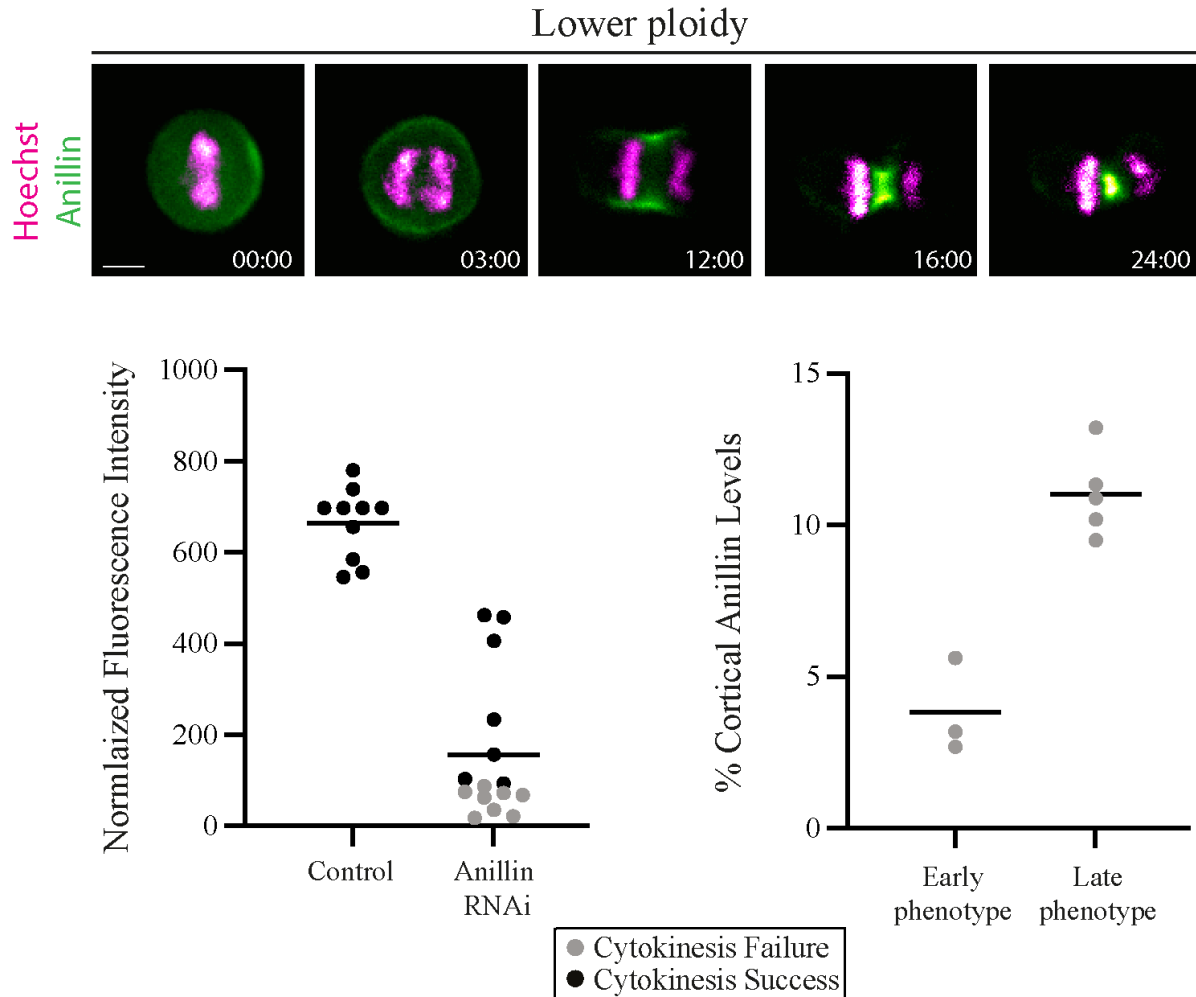
Figure S2: Anillin requirement in CoCl₂-treated lower ploidy HCT116 cells. Timelapse fluorescence images show mNeonGreen-anillin in a CoCl₂-treated HCT116 cell with lower ploidy (Hoescht to stain chromatin, magenta). Times are shown in minutes and the scale bar is 10 μm. Underneath, dot plots show the normalized fluorescence intensity (a.u.) of anillin in control (n=10) or after anillin RNAi (n=15) these cells. The cells that failed cytokinesis are in grey, and those that succeeded are in black. Also shown are dot plots for the % of cortical anillin remaining in lower ploidy cells with early vs. late cytokinesis phenotypes.
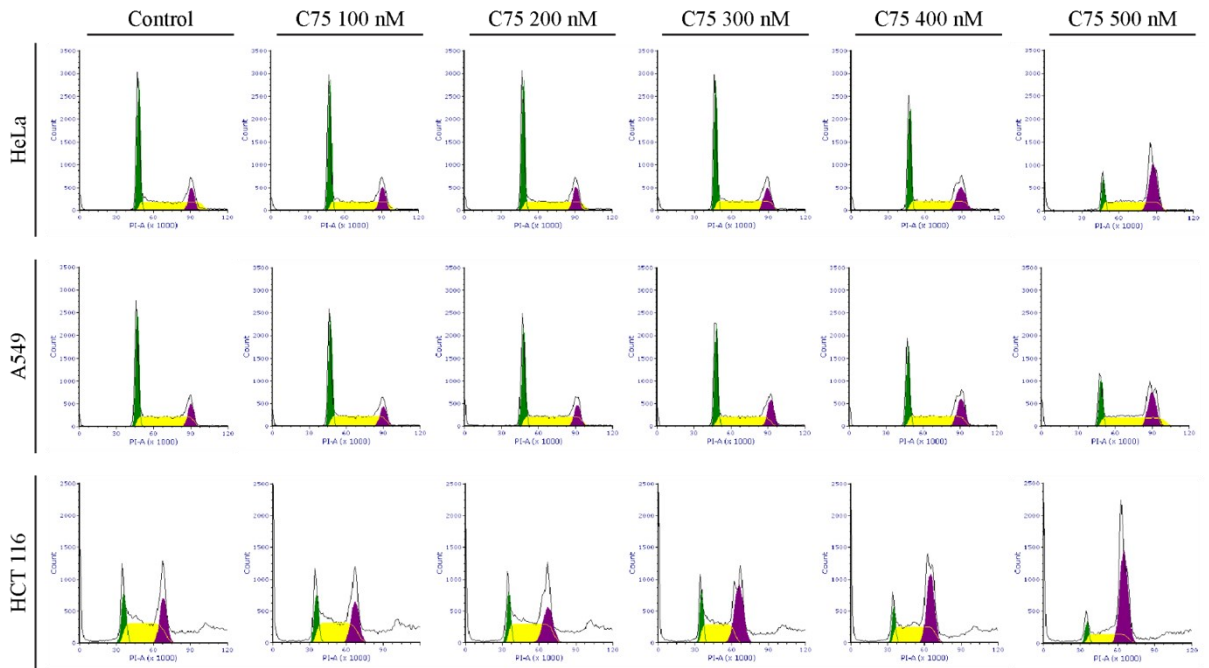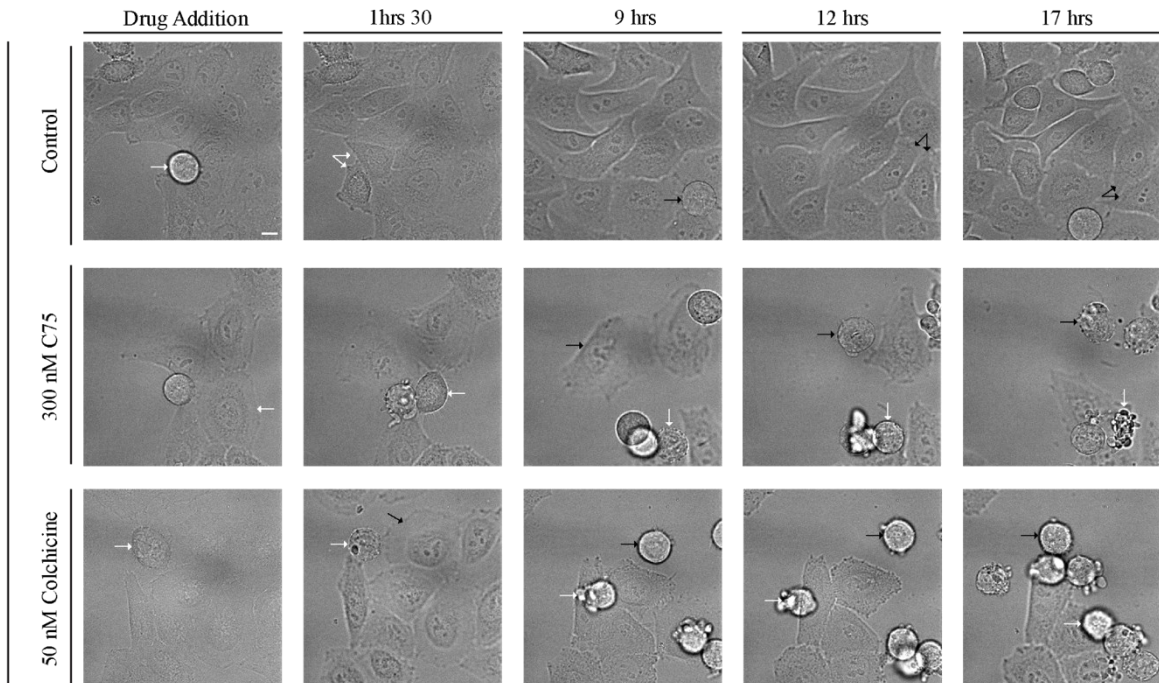
A

B

Figure S3: C75 causes cells to arrest in G2/M. A) Graphs show the proportion of HeLa, A549 and HCT116 cells in the different phases of the cell cycle (G1 in green; S in yellow; G2/M in purple) 8 hours after treatment with varying concentrations of C75, as determined by flow cytometry. Cell counts are on the Y-axis and propidium iodide (PI) intensity (levels) is on the Xaxis. B) DIC images show fields of view of HeLa cells after addition of DMSO (control), 300 nM C75 or 50 nM colchicine over time for 17 hours. White and black arrows point to cells. The scale bar is 10 μm.

A

[Colchicine], nM	% Lethality
0	0%
1	2%
5	2%
10	58%
20	99%
30	99%
40	99%
50	100%
100	100%
1000	100%

[C75], nM	% Lethality
0	0%
1	6%
10	10%
100	0%
200	9%
300	22%
400	23%
500	97%
700	99%
1000	100%

[Colchicine], nM	[C75], nM	% Lethality	Combination Index (CI)	
0	0	0%	>1000	Antagonistic
3	0	19%	7.4	Antagonistic
3	100	14%	237	Antagonistic
3	300	95%	0.2	Synergistic
3	500	100%	0	-
3	1000	100%	0	-
3	10000	99%	0	-

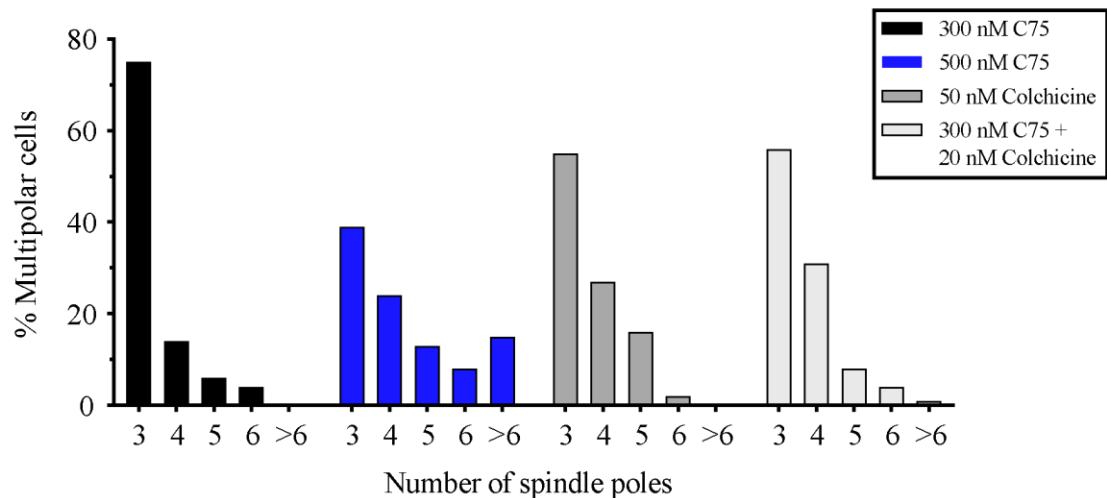| [C75], nM	[Colchicine], nM	% Lethality	Combination Index (CI)	
0	0	0%	>1000	Antagonistic
250	0	2%	>1000	Antagonistic
250	1	12%	897	Antagonistic
250	5	96%	0.25	Synergistic
250	10	100%	0	-
250	20	100%	0	-
250	30	99%	0	-
250	40	99%	0	-
250	50	100%	0	-
250	100	100%	0	-
250	1000	100%	0	-

B

Figure S4: Combining C75 and colchicine cause enhanced lethality and spindle phenotypes. A) Tables illustrate the percent lethality of HeLa cells treated with colchicine (top left), C75 (top right), or both in combination (bottom two) for different concentrations as indicated. Also included are values for the Combination Index (CI) calculated using CompuSyn software, and whether the values indicate synergistic, antagonistic or additive interactions. Red boxes highlight the lowest concentrations that show synergism between C75 and colchicine. B) A bar graph shows the percentage of multipolar HeLa cells from Figure 3C with different numbers of 2 spindle poles after treatment with 300 nM C75 (black), 500 nM C75 (blue), 50 nM colchicine (dark grey) or 300 nM colchicine plus 20 nM colchicine (light grey).
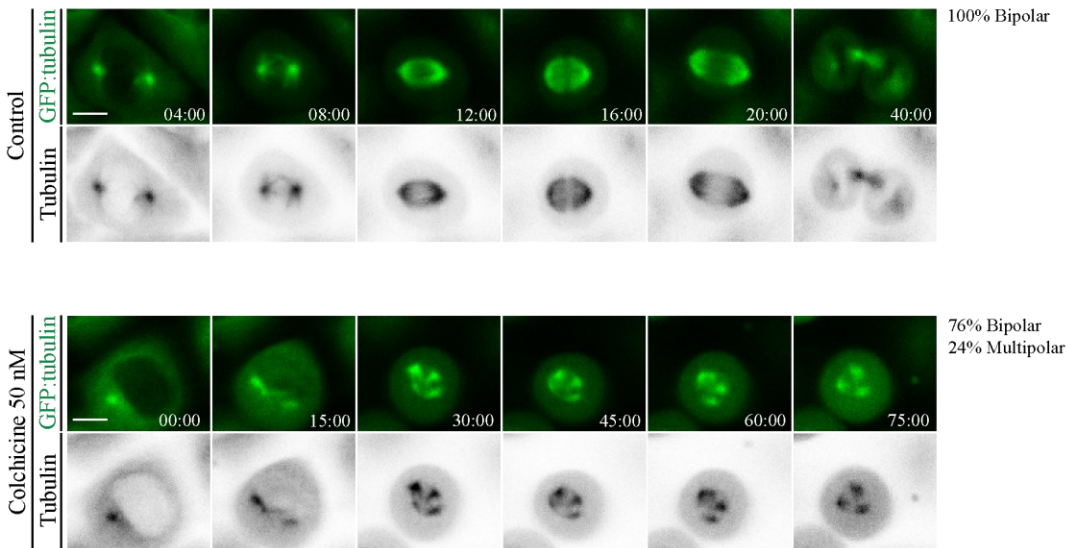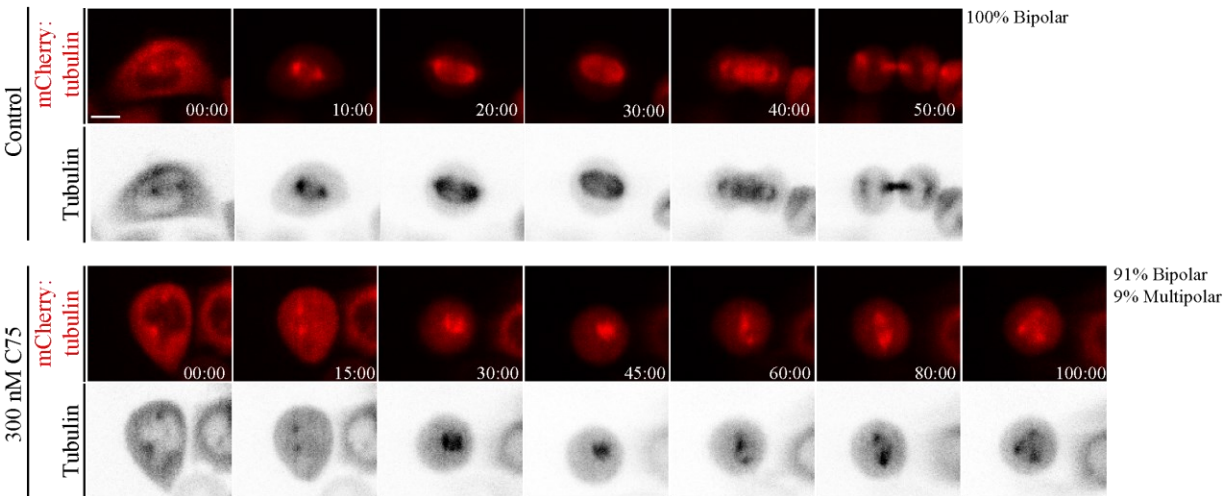
Figure S5: Colchicine causes centrosome fragmentation prior to metaphase. A) Timelapse images show live HeLa cells expressing GFP:tubulin (green) without (control, n=12) or after treatment with 50 nM colchicine (n=74). Times are indicated in minutes. The proportion of cells with bipolar or multipolar spindles are indicated. B) Timelapse images show HeLa cells expressing mCherry:tubulin (red) without (control, n=22) or after treatment with 300 nM C75 (n=44). Times are indicated in minutes. The proportion of cells with bipolar, multipolar or monopolar spindles are indicated. The scale bar for cells in A) and B) is 10 µm.
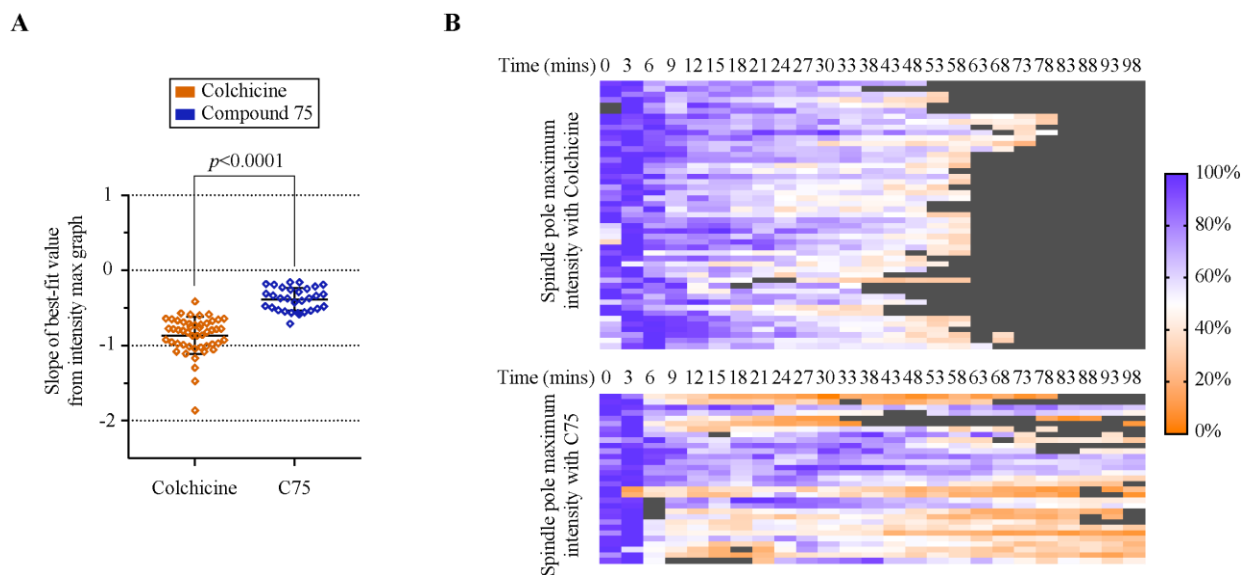
Figure S6: Spindle poles recover in the presence of C75. A) A scatter plot shows the distribution of best-fit slope values obtained from plotting changes in the maximum intensity of tubulin at spindle poles over time after treatment with 300 nM colchicine or C75. Statistics were done using two-tailed Welch's t test with a $p < 0.0001$. B) Heat maps show the change in maximum intensity of tubulin at each spindle pole (%) over time (in minutes) after treatment with 300 nM colchicine (top) or C75 (bottom). Purple indicates high values, while orange indicates low values.